The mechanical consequences of internal erosion on gap-graded soil

Author:
Li, Shijin

Publication Date:
2019

DOI:
https://doi.org/10.26190/unsworks/21740

THE MECHANICAL CONSEQUENCES OF INTERNAL EROSION ON GAP-GRADED SOIL

Shijin Li

A thesis in fulfilment of

the requirements for the degree of

Doctor of Philosophy

School of Civil and Environmental Engineering

The University of New South Wales

Sydney, Australia

December 2019

Thesis/Dissertation Sheet

Surname/Family Name	:	**Li**
Given Name/s	:	**Shijin**
Abbreviation for degree as give in the University calendar	:	**PhD**
Faculty	:	**Engineering**
School	:	**School of Civil and Environmental Engineering**
Thesis Title	:	**The Mechanical Consequences of Internal Erosion on a Gap-Graded Soil**

Abstract 350 words maximum

The mechanical consequences of internal erosion (suffusion) on a gap-graded soil are investigated.

A new soil sample formation procedure is proposed which results in homogeneous particle size distributions along the length of an eroded sample. Triaxial tests are conducted on homogeneous samples formed using the new procedure as well as heterogeneous samples created by the more commonly used approach. The results show the samples with homogeneous post-erosion particle size distributions exhibit slightly higher peak deviator stresses than those which were heterogeneous. The results highlight the importance of ensuring homogeneity of post-erosion.

Additional triaxial erosion tests on the gap-graded soil having undergone different amounts of internal erosion at varying confining stresses are conducted. The hydraulic gradient, confining stress and initial density have significant influences on the erosion characteristics. The peak deviator stress tends to decrease as the amount of erosion increases. The volumetric strain at large shear strains decreases as the volume of seepage water and the amount of erosion increase. Internal erosion also causes the critical state line to move upwards. The upward movement of the critical state line is lesser than the increase of the void ratio due to internal erosion.

A direct mathematical link between the fractal dimension and void ratio for soils with single or double fractal particle size distributions is developed, incorporating some practical and realistic assumptions. In gap graded soils, different amounts of internal erosion result in the fractal dimension of the finer component to vary. The changing particle size distribution due to internal erosion may be expressed solely in terms of the change in fractal dimension. The change in the void ratio can also be expressed in terms of this changing fractal dimension.

A modified grading state index is proposed using fractals enabling the effects of the shape of the particle size distribution to be considered. The dominant effects of the increase in void ratio and changing grading are incorporated into an extension of the Severn-Trent sand constitutive model. The extended model describes the stress-strain behaviors of soils subjected to internal erosion. Model simulations fit well with the experiment data.

ORIGINALITY STATEMENT

'I hereby declare that this submission is my own work and to the best of my knowledge it contains no materials previously published or written by another person, or substantial proportions of material which have been accepted for the award of any other degree or diploma at UNSW or any other educational institution, except where due acknowledgement is made in the thesis. Any contribution made to the research by others, with whom I have worked at UNSW or elsewhere, is explicitly acknowledged in the thesis. I also declare that the intellectual content of this thesis is the product of my own work, except to the extent that assistance from others in the project's design and conception or in style, presentation and linguistic expression is acknowledged.'

Signed ……..

Date ……..

INCLUSION OF PUBLICATIONS STATEMENT

UNSW is supportive of candidates publishing their research results during their candidature as detailed in the UNSW Thesis Examination Procedure.

Publications can be used in their thesis in lieu of a Chapter if:

- The candidate contributed greater than 50% of the content in the publication and is the "primary author", ie. the candidate was responsible primarily for the planning, execution and preparation of the work for publication
- The candidate has approval to include the publication in their thesis in lieu of a Chapter from their supervisor and Postgraduate Coordinator.
- The publication is not subject to any obligations or contractual agreements with a third party that would constrain its inclusion in the thesis

Please indicate whether this thesis contains published material or not:

☐ This thesis contains no publications, either published or submitted for publication
(if this box is checked, you may delete all the material on page 2)

☐ Some of the work described in this thesis has been published and it has been documented in the relevant Chapters with acknowledgement
(if this box is checked, you may delete all the material on page 2)

☒ This thesis has publications (either published or submitted for publication) incorporated into it in lieu of a chapter and the details are presented below

CANDIDATE'S DECLARATION

I declare that:

- I have complied with the UNSW Thesis Examination Procedure
- where I have used a publication in lieu of a Chapter, the listed publication(s) below meet(s) the requirements to be included in the thesis.

Candidate's Name	**Signature**	**Date (dd/mm/yy)**

POSTGRADUATE COORDINATOR'S DECLARATION *To only be filled in where publications are used in lieu of Chapters*

I declare that:

- the information below is accurate
- where listed publication(s) have been used in lieu of Chapter(s), their use complies with the UNSW Thesis Examination Procedure
- the minimum requirements for the format of the thesis have been met.

PGC's Name	**PGC's Signature**	**Date (dd/mm/yy)**

For each publication incorporated into the thesis in lieu of a Chapter, provide all of the requested details and signatures required

Details of publication #1:
Full title: The influence of particle size distribution homogeneity on the shearing of soils having been subjected to internal erosion
Authors: Shijin Li, Adrian Russell, David Muir Wood
Journal or book name: Canadian Geotechnical Journal
Volume/page numbers: --
Date accepted/ published: Accepted on 16/11/2019

Status	*Published*		*Accepted and In press*	✓	*In progress (submitted)*	

The Candidate's Contribution to the Work
First author

Location of the work in the thesis and/or how the work is incorporated in the thesis:
Chapter 3

PRIMARY SUPERVISOR'S DECLARATION

I declare that:

- the information above is accurate
- this has been discussed with the PGC and it is agreed that this publication can be included in this thesis in lieu of a Chapter
- All of the co-authors of the publication have reviewed the above information and have agreed to its veracity by signing a 'Co-Author Authorisation' form.

Primary Supervisor's name	**Primary Supervisor's signature**	**Date (dd/mm/yy)**

Details of publication #2:
Full title: A sample formation procedure to obtain homogeneous post-erosion particle size distribution
Authors: Shijin Li, Adrian Russell
Journal or book name: 7th International Symposium on Deformation Characteristics of Geomaterials (IS-Glasgow 2019)
Volume/page numbers: E3S Web Conf. Volume 92, 2019
Date accepted/ published: 02/07/2019

Status	*Published*	✓	*Accepted and In press*		*In progress (submitted)*	

The Candidate's Contribution to the Work
First author

Location of the work in the thesis and/or how the work is incorporated in the thesis: Chapter 3		
PRIMARY SUPERVISOR'S DECLARATION I declare that: • the information above is accurate • this has been discussed with the PGC and it is agreed that this publication can be included in this thesis in lieu of a Chapter • All of the co-authors of the publication have reviewed the above information and have agreed to its veracity by signing a 'Co-Author Authorisation' form.		
Primary Supervisor's name	**Primary Supervisor's signature**	**Date (dd/mm/yy)**

Details of publication #3: *Full title: Stress-strain behaviour of soils having undergone different amounts of internal erosion* *Authors: Shijin Li, Adrian Russell, David Muir Wood* *Journal or book name: Proceedings of 25th meeting of European Working Group on Internal Erosion in Embankment Dams & their Foundations* *Volume/page numbers: pp114-122* *Date accepted/ published: 04/07/2017*						
Status	*Published*	✓	*Accepted and In press*		*In progress (submitted)*	
The Candidate's Contribution to the Work First author						
Location of the work in the thesis and/or how the work is incorporated in the thesis: Chapter 3						
PRIMARY SUPERVISOR'S DECLARATION I declare that: • the information above is accurate • this has been discussed with the PGC and it is agreed that this publication can be included in this thesis in lieu of a Chapter • All of the co-authors of the publication have reviewed the above information and have agreed to its veracity by signing a 'Co-Author Authorisation' form.						
Primary Supervisor's name		**Primary Supervisor's signature**			**Date (dd/mm/yy)**	

ABSTRACT

The mechanical consequences of internal erosion (suffusion) on a gap-graded soil are investigated.

A new soil sample formation procedure is proposed which results in homogeneous particle size distributions along the length of an eroded sample. Triaxial tests are conducted on homogeneous samples formed using the new procedure as well as heterogeneous samples created by the more commonly used approach. The results show the samples with homogeneous post-erosion particle size distributions exhibit slightly higher peak deviator stresses than those which were heterogeneous. The results highlight the importance of ensuring homogeneity of post-erosion.

Additional triaxial erosion tests on the gap-graded soil having undergone different amounts of internal erosion at varying confining stresses are conducted. The hydraulic gradient, confining stress and initial density have significant influences on the erosion characteristics. The peak deviator stress tends to decrease as the amount of erosion increases. The volumetric strain at large shear strains decreases as the volume of seepage water and the amount of erosion increase. Internal erosion also causes the critical state line to move upwards. The upward movement of the critical state line is lesser than the increase of the void ratio due to internal erosion.

A direct mathematical link between the fractal dimension and void ratio for soils with single or double fractal particle size distributions is developed, incorporating some practical and realistic assumptions. In gap graded soils, different amounts of internal erosion result in the fractal dimension of the finer component to vary. The changing particle size distribution due to internal erosion may be expressed solely in terms of the change in fractal dimension. The change in the void ratio can also be expressed in terms of this changing fractal dimension.

A modified grading state index is proposed using fractals enabling the effects of the shape of the particle size distribution to be considered. The dominant effects of the increase in void ratio and changing grading are incorporated into an extension of the Severn-Trent sand constitutive model. The extended model describes the stress-strain behaviors of soils subjected to internal erosion. Model simulations fit well with the experiment data.

ACKNOWLEDGMENTS

The work described in this thesis was carried out as part of a project of the Australian Research Council Discovery Project DP150104123 initiated by my supervisor Professor Adrian Russell. Financial assistance of the Australia Research Council and of the China Scholarship Council are gratefully acknowledged.

I would like to express my deepest gratitude to my supervisor Professor Adrian Russell for the continuous support of my Ph.D study and research, for his patience, motivation, and immense knowledge. He has made himself available at all times for giving me invaluable advice and direction. Working under his supervision has greatly broadened my knowledge in geotechnical engineering, especially in fractal theories and constitutive modelling, and has increased my self-confidence in doing research.

Also, I thank Mr Paul Gwynne, Mr Timothy Weston, Mr Luiz Pettersen, Mr William Terry and Mr Anthony Macken for preparing laboratory equipment and quick response to my calls for assistance.

Also, I thank Professor David Muir Wood for valuable advice and guidance with my experiments, paper writing and modelling. I also thank Professor Nasser Khalili, Dr Kurt Douglas, Dr Arman Khoshghalb, Dr Thanh Vo, and Dr Babak Shahbodaghkhan for attending my research progress reviews and their valuable advice.

I also thank my colleagues and friends who accompanied me on this journey and helped me over the last four years. They are Dr Adnan Sufian, Dr Yi Tang, Yunjie Mai, Xidong Zhang, Diyang Qi, Yanzhi Wang, Gaochao Lin, Vienti Hadsari, Dr Junnan Yang, Dr Rong Hu, Dr Yifan Zuo.

Thanks are extended to the staff of the School of Civil and Environmental Engineering of the University of New South Wales for their efficient services throughout the course of my candidature.

Last but not least, I appreciate my parents and my sister's support and encouragement.

Shijin Li

Sydney, Australia

13/12/2019

Table of Contents

List of Figures

List of Tables

CHAPTER 1 INTRODUCTION

1.1 BACKGROUND

Water retaining structures such as embankment dams, levees and dykes are critical elements of modern civil infrastructure. They retain reservoirs for water supply and production of electricity, and provide protection from flooding, and are expected to perform safely for many decades. However, internal erosion of the soils forming the containment structures may occur and lead to expensive maintenance costs or, in extreme cases, total collapse.

Slow seepage of water through soils may wash fine particles from one layer to the next layer. It is a particular concern for non-plastic soils in dam cores, filters and transition layers and broadly graded or gap-graded silt/sand soils in dam and levee foundations. Removal of fine particles results in a narrower, coarser gradation, and higher permeability. It reduces the stability of the remaining stress-carrying particles and may eventually lead to overall dam collapse. Around 50% of dam failures and dysfunctions are caused by internal erosion (Foster et al. 2000).

One type of internal erosion, referred to as suffusion, is caused by water seeping through the matrix of coarse soil, progressively transporting out of fine particles, while the soil matrix does not deform in any significant way.

Internal erosion may affect soils in many ways. It causes a change to the particle size distribution, an increase in void ratio and, most importantly, alterations to mechanical properties including strength and stress-strain behavior. In recent years, laboratory-controlled tests on soils have been used to study the causes and mechanical consequences of internal erosion. For example, (Bendahmane et al. 2008; Moffat et al. 2011; Richards and Reddy 2009) subjected soil samples

to internal erosion using a range of hydraulic conditions and confining stress states in order to understand their effects on the erosion process. Other laboratory tests have addressed how the strength and stress-strain behavior of soils may be affected by internal erosion (Chang and Zhang 2011; Chang et al. 2014; Ke and Takahashi 2014b; Ouyang and Takahashi 2015).

While the results of these experiments are a major interest to dam owners and their engineering advisors, providing some guidance on what strength changes and alterations to the stress-strain behavior of the soil can be expected, they have a limitation that restricts their usefulness. In most cases, it was observed that the internal erosion of the samples prior to triaxial testing caused a heterogeneous particle size distribution to develop throughout the sample. Kenney and Lau (1985) conducted seepage tests on granular soils and found that downward flow resulted in the formation of a top transition zone (where the particles are the coarsest and the concentration of fine particles is the lowest), a central homogeneous zone and a bottom transition zone (where the concentration of fine particles is the largest). Chang and Zhang (2011) and Ke and Takahashi (2014b) also reported heterogeneous post-erosion particle size distributions for samples subjected to downward flow that were consistent with Kenney and Lau (1985). This heterogeneity of the particle size distribution may introduce other heterogeneities related to void ratio, state parameter, soil deformation and load distribution throughout a sample, meaning the stress-strain behaviors and strengths measured at the sample boundaries are not representative of what is happening at critical sections inside the samples.

Several significant contributions (Kikumoto et al. 2010; Muir Wood 2007; Muir Wood and Maeda 2007; Muir Wood et al. 2010) studied the influences, especially mechanical influences, of changing particle size distributions on soils. Muir Wood (2007) proposed the idea of a grading state index to characterize the geometry of the particle size distribution. He studied how a changing grading state index influences the mechanical behavior of the soil. Muir Wood and Maeda (2007) concluded that the changing grading has a first-order influence on the critical state parameters and this has been applied to develop constitutive models to predict the mechanical consequences of internal erosion at a certain fixed stress state (Muir Wood et al. 2010), and also

particle crushing (Kikumoto et al. 2010), based on the Severn-Trend sand constitutive modelling framework (Gajo and Wood 1999). However, the stress-strain behavior of soils having undergone different amounts of internal erosion, and the nature of the changes to the particle size distributions, are not fully understood. Simplifying assumptions are often made, such as the gradual and complete removal of the finest particles as erosion progresses, with laboratory data suggesting the particle removals differ from this.

Novel theories have been developed which link the particle size distribution and its fractal characteristics to void ratio and other microstructural properties (Russell (2010) Russell and Buzzi (2012) yet have not been applied in studies on the mechanical consequences of internal erosion.

1.2 OBJECTIVE, METHOD AND SCOPE

The main objective of this research is to understand the mechanical consequences of internal erosion and produce a constitutive model able to simulate the stress-strain behavior of soils having experienced varying amounts of internal erosion. Attention is given to a gap-graded cohesionless soil, which is particularly susceptible to internal erosion, although many of the research findings and methods developed have applicability to soils with other gradings.

To achieve this a major part of the research is devoted to the formation of homogeneous samples for triaxial testing. The triaxial tests enable determinations of strength and stress-strain behaviors and are most relevant when conducted on homogenous samples. The results of the triaxial tests enable theoretical links between microstructural characteristics and large-scale mechanical properties to be made for use by researchers, dam engineers and owners, making them better able to predict the mechanical consequences of internal erosion.

A new procedure for the formation of soil samples for internal erosion testing that have homogeneous post-erosion particle size distributions is proposed. The differences in stress-strain behaviors of soil samples formed by the new procedure and a commonly used procedure that results in heterogeneous post-erosion particle size distributions are compared, confirming the sample's homogeneity influences the results.

A series of drained triaxial compression tests are then conducted to investigate the stress-strain behavior of the gap-graded soil having undergone different amounts of internal erosion. The triaxial erosion tests are conducted using a modified triaxial apparatus, able to subject samples to different amounts of internal erosion by upward or downward flow prior to testing. Also, the erosion characteristics under varying hydraulic and stress conditions are studied.

Theoretical links between the changing fractal dimension of the finer fraction of the gap-graded soil and the increase in void ratio are developed and validated using the experimental data.

A new grading state index is defined to incorporate the fractal characteristics and shape of the particle size distribution to make it more realistic and better able to capture unique features of the particle size distribution before and after internal erosion. The grading state index is then incorporated into an extended existing Severn-Trent sand model. The grading state index and model account for changes to the void ratio and critical state line which accompany erosion.

1.3 THESIS STRUCTURE

The structure of the thesis is as follows.

Chapter 2 reviews previous laboratory investigations on eroded samples and what is currently known about the mechanical consequences of internal erosion. The fractal characterization of particle size distributions, and constitutive models for soils subjected to a changing grading, are also reviewed.

Chapter 3 presents a new procedure for the formation of eroded soil samples for triaxial testing that have homogeneous particle size distributions. The differences in stress-strain behaviors of soil samples formed by the new procedure, and a commonly used procedure that results in heterogeneous post-erosion particle size distributions, are compared.

Chapter 4 presents additional laboratory triaxial erosion tests on the gap-graded soil having undergone different amounts of internal erosion at varying effective confining stresses. The effects of different amounts of internal erosion on mechanical behavior and the evolution of critical state lines for samples subjected to different amounts of internal erosion are discussed.

Chapter 5 develops a theoretical link between the changing fractal dimension of the finer fraction of a gap-graded soil and the increase in void ratio. This theoretical link is validated by experimental data.

Chapter 6 presents a model for the stress-strain behavior of soils subjected to different amounts of internal erosion. It is an extension of the Severn Trent sand model, and incorporates the effects of a changing grading, void ratio and critical state line.

Chapter 7 summarizes the major findings of the research and outlines recommendations for further research.

CHAPTER 2 LITERATURE REVIEW

2.1 INTRODUCTION

The literature review comprises three main sections. In Section 2.2 experimental investigations on mechanical influences of internal erosion on soils are reviewed. In Section 2.3 the fractal characteristics of particle and pore size distributions are discussed. In Section 2.4 constitutive modelling of internal erosion is discussed.

2.2 EXPERIMENTAL INVESTIGATIONS ON MECHANICAL INFLUENCES OF INTERNAL EROSION ON SOILS

Soils may be subjected to suffusion, a type of internal erosion, whereby water seeps through the matrix formed by the coarser particles of the soil and progressively removes the finer particles while the matrix does not deform in any significant way. Around 50% of dam failures and dysfunctions are caused by internal erosion (Foster et al. 2000). A number of investigations have been conducted by researchers to study the mechanical consequences on internal erosion, the hydraulic characteristics and the erosion process.

Laboratory studies on mechanical influences of internal erosion and particle removal have been discussed by Bendahmane et al. (2008), Chang and Zhang (2011, 2012), Xiao and Shwiyhat (2012), Ke and Takahashi (2012, 2014a, 2014b, 2015), McDougall et al. (2013), Sato and Kuwano (2015, 2018), Chang et al. (2014), and Ouyang and Takahashi (2015).

Bendahmane et al. (2008) developed an experimental device that can apply hydraulic stresses to soil samples to characterize the erosion process. The apparatus contains a modified triaxial system with a hollow base pedestal, end platens and a drainage system to cause particle removal under a confining stress. However, Bendahmane et al. (2008) only conducted internal erosion tests on soils under complex confining pressures and varying hydraulic conditions. Mechanical alterations were not reported.

Chang and Zhang (2011) developed a stress-controlled triaxial erosion apparatus, comprised a pressurized water supply system, a triaxial system and effluent and fine particle collection system, to investigate the initiation and development of internal erosion under isotropic and anisotropic stress conditions and to study the mechanical influences of suffusion on the soil. The triaxial apparatus was modified to include a hollow base pedestal. A perforated plate was attached at both ends of the sample to support the soil, as shown in Figure 2-1. This modification made it possible for seepage to pass through the soil sample and cause erosion. They conducted a series of internal erosion tests and shearing tests on eroded samples under complex stress states (isotropic, drained triaxial compression and triaxial extension stress paths) and found that the total deformation, the maximum erosion rate and total weight of the eroded fine particles increased with the increase of deviator stress. They observed that the original dilative stress-strain response changed to a contractive response and the peak drained strength decreased. They also found that the post-erosion particle size distributions in different layers of the sample were heterogeneous. In a similar laboratory investigation, Chang and Zhang (2012) studied the critical hydraulic gradient that was needed for initiation of internal erosion in gap-graded soils under complex stress states. The experiment setup and testing procedures they developed to conduct the internal erosion tests and subsequent triaxial compression tests provided a feasible methodology for others to investigate the hydraulic and mechanical influences of internal erosion on gap-graded soils.

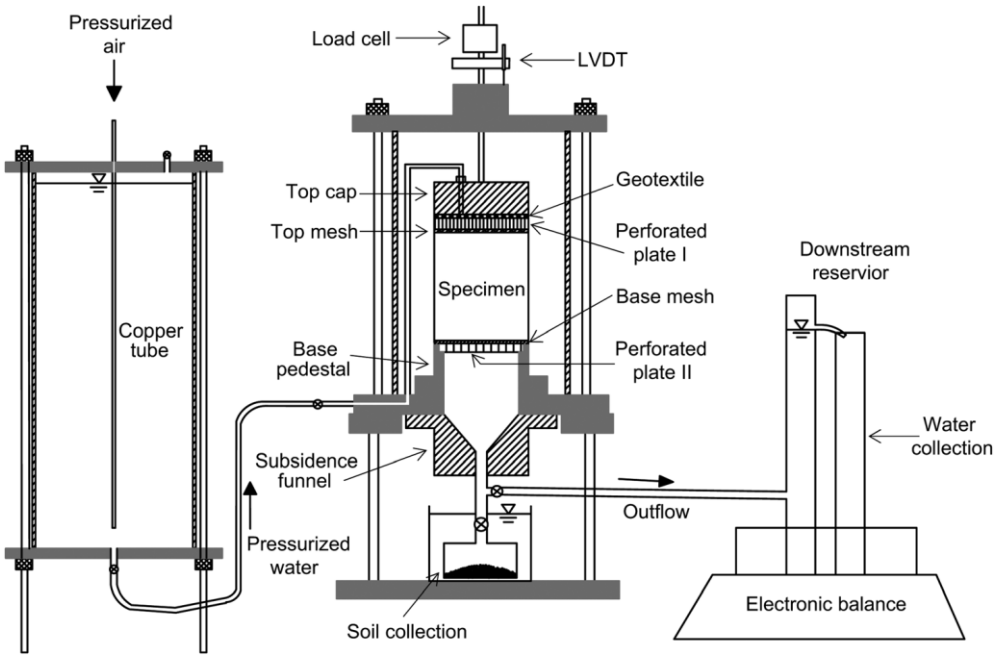

Figure 2-1 Schematic of the triaxial erosion testing apparatus, from Chang and Zhang (2011)

Xiao and Shwiyhat (2012) conducted triaxial erosion tests on three types of gap-graded soils and a poorly graded soil using a modified triaxial apparatus that allowed seepage to pass through a compacted sample to cause erosion. The apparatus permitted collection of effluent and eroded fine particles. The initial pore size distributions of the four soils were determined by mercury intrusion porosimetry. However, the post-erosion pore size distributions were not determined. They observed a reduction in permeability and total soil volume in the gap-graded soils. They attributed the permeability reduction to fine particle migration and clogging. Fine particle clogging was observed occasionally. They found that gap-graded soils exhibited an undrained strength increase after internal erosion, while poorly graded soils exhibited an undrained strength reduction after internal erosion. They attributed the undrained strength increase for gap-graded soils to an erosion-induced loss of sample saturation. The bottom of the eroded samples were subjected to atmospheric pressure, which resulted in a decrease in pore pressure. Even though a re-saturation procedure was applied, it was observed to be ineffective. The strength differences for poorly graded soils contain clay before and after erosion was caused by the different effective confining pressures because the erosion also caused pore pressure variation in samples. Higher effective confining stress leads to higher compressive strength.

Ke and Takahashi (2012) performed a series of 1-D upward internal erosion tests imposing a constant water head to cause suffusion. Soils with varying fines contents, relative densities and maximum applied hydraulic gradients were considered. They examined the mechanical influences of the internal erosion using cone penetration tests and direct shear tests. They concluded that the cone resistance decreases after the soil was subjected to internal erosion. It was unclear which of the following factors caused the strength reduction; the loss of fine particles or the change in the interlocking of the soil particles due to internal erosion. Another limitation was that the maximum hydraulic gradient imposed on their samples could not be larger than 0.5.

Instead of applying seepage to cause a loss of particles, McDougall et al. (2013) came up with the idea of forming soil samples with dissolvable particles. They mixed salts and sands to form soil sample and loaded the sand-salt mixture sample in a modified permeation oedometer. The salt subsequently dissolved. They concluded that the overall sand-salt sample volume changes were dependent on the amounts of dissolved particles. The loss of particles resulted in an increase in void ratio. By compressing the dissolved samples, they found that the dissolution of larger particles led to more volumetric contraction during monotonic confined compression. Although both particle dissolution and particle removal by internal erosion cause particle losses, the mechanisms are different.

The process of erosion occurs very slowly in the field, perhaps over a period of decades (i.e. WAC Bennet Dam) (Muir Wood et al, 2010). So, the removal of fine particles could be treated as gradually and progressively. Therefore, it is necessary to study the stress-strain behavior of soils having undergone varying amounts of internal erosion. Ke and Takahashi (2014a, 2014b) developed a triaxial erosion apparatus to investigate the mechanical influences of internal erosion on gap-graded soils. Their apparatus consists of a constant-flow-rate control system, a triaxial compression system and an eroded soil-collection system. Unlike Chang and Zhang (2011)'s apparatus, which provides a constant hydraulic gradient to cause internal erosion, the

constant-flow-rate system pumps water through soil sample at constant flow rate to cause internal erosion. The shortcoming of the former is that it is difficult to estimate the head loss when seepage passes through valves, tubes and right-angled type fittings. The flow-rate-control method, on the other hand, is a good way to avoid these head losses. The other parts of the modified apparatus are similar to Chang and Zhang (2011)'s triaxial erosion testing apparatus. The authors conducted undrained and drained compression tests and undrained cyclic tests on eroded soil samples and concluded that eroded soils exhibited lower drained shear strengths (especially soils with high initial fines contents), higher undrained peak deviator stresses and lower post-peak undrained deviator stresses compared with soil samples without internal erosion. The small-strain stiffness of the eroded soil at the beginning of drained compression was larger than that of the soil without erosion. They attributed the alteration in mechanical behavior of the soils subjected to internal erosion to the increase in post-erosion void ratios. In terms of undrained cyclic tests on soil samples, they found that the behavior of soils with internal erosion exhibited a "limited flow deformation" pattern, while the behavior of soils without internal erosion exhibited a "flow deformation" pattern. Ke and Takahashi (2014b) have also studied the mechanical behavior of soils under cyclic conditions. They also found that the post-erosion particle size distributions of the top and the bottom layer moved downwards from its original position due to internal erosion. However, there was greater fine particles losses at the top layers of the samples.

Chang et al. (2014) studied the mechanical effects of internal erosion on gap-graded soils using the same apparatus of Chang and Zhang (2011). A particular interest of the study was the evolution of the critical state line due to internal erosion. They assumed that the slope of critical state line in the compression plane of a soil before and after internal erosion does not change. They found that the critical state line tends to moves upwards due to the loss of fines, in accordance with Wood and Maeda (2008) and Muir Wood et al. (2010).

Ouyang and Takahashi (2015) conducted triaxial erosion tests on soils with different initial fines contents. The test apparatus was the same as the one used by Ke and Takahashi (2014b). Soils

were prepared to have initial fines contents of 0%, 15%, 25% and 35% by weight. Ouyang and Takahashi (2015) compared the undrained stress-strain behaviors of the soils with and without internal erosion. They found that the soils show less contractive tendency after the removal of fine particles by internal erosion. The undrained stiffnesses of soils having been subjected to internal erosion were greater than those of soils without internal erosion at small strains. The undrained peak deviator stresses and strengths of the soils having been subjected to internal erosion were greater than those of soils without internal erosion at large strains. The excess pore-water pressure build up in soils having been subjected to internal erosion were not as great in of soils without internal erosion. In terms of the influence of initial fines contents, they concluded that a lower fines content resulted in higher undrained peak and residual strengths.

Sato and Kuwano (2018) conducted triaxial erosion tests to investigate the influence of a small amount of particle removal induced by internal erosion on deformation and stiffness of well-graded soil samples containing plastic clay. Their experimental results show that a well-graded cohesive soil is vulnerable to internal erosion and that the bonded clay-sand matrix is immigrated by seepage flow. The deviator stress and stiffness decreased with the increase of the amount of internal erosion at intermediate strains, but the strength reduction tended to cease at large strains. Electron microscopy scanning results indicated that the rearrangement of the soil mixture due to particle removal lead to an anisotropic behavior.

2.3 THE FRACTAL CHARACTERIZATION OF SOIL AND ITS APPLICATION IN SOIL MECHANICS

2.3.1 Introduction and definitions

One classic example of a fractal refers to measuring the total length of a coastline. The total length L is linked to the length of the rule l by which it is measured through:

$$L \propto l^{1-D} \qquad (2\text{-}1)$$

in which D is the fractal dimension.

More generally the a fractal dimension is an index that characterizes fractal sets or patterns or sets by quantifying their complexity as a ratio of the change in detail to the change in scale (Mandelbrot 1983). It is defined as:

$$D = \frac{\log(N)}{\log(L)} \qquad (2\text{-}2)$$

where N is the number of self-similar pieces and L is the magnification factor.

Power-law relations similar to Equation (2-1) have been formed to describe particle size distributions in soils. Instead of a measurement of the length of coastline, the measured quantity is the total number of particles greater than a specific particle size d. For a well-graded soil the concept of a fractal indicates that, across a wide range of particle sizes, the soil particle size distribution is self-similar.

2.3.2 Literature review on fractal characterization of soil and its application in soil mechanics

Fractals and particle size distribution

A fractal particle size distribution exists when

$$N(d_s > d) \propto d^{-D_s} \qquad (2\text{-}3)$$

where $N(d_s > d)$ is the number of soil particles of size d or greater and D_s is the fractal dimension of the soil's particle size distribution. Gee and Bauder (1986) measured the mass of

particles whose sizes were between a lower and upper boundary according to the sieve diameters or particle settling times. They estimated the number of particles of size d or greater, $N(d_s > d)$, by assuming some representative particle size, $\bar{d}$, whose density and volume were linked to the number of soil particles between two adjacent sieves, d_i and d_{i+1}. The approximate cumulative numbers of particles greater than $\bar{d}$ can be expressed as:

$$N(d_s > \bar{d}) \approx \sum_{i=1}^{n} N(d_i < d < d_{i+1}) = \sum_{i=1}^{n} \frac{M(d_i < d < d_{i+1})}{4/3\,\pi \bar{d}^3 \rho} \qquad (2\text{-}4)$$

where $M(d_i < d < d_{i+1})$ is the mass of soil particles between two adjacent sieves of opening size of d_i and d_{i+1}, ρ is the density of soil particle. In this approximation approach, the number is estimated based on representative average sizes, not actual sizes. As a result, the calculation is highly dependent on the choice of the value of $\bar{d}$, especially when $\bar{d}$ is small.

Tyler and Wheatcraft (1992) suggested calculating the mass of soil particles whose sizes are greater than d because the mass of the soil is more easily to be measured. According to Mandelbrot (1983), the volume $V(d_s > d)$ of cubes of size d or greater is expressed as:

$$V(d_s > d) = \Lambda[1 - (\frac{d}{\lambda_v})^{3-D_s}] \qquad (2\text{-}5)$$

where Λ and λ_v are constants describing shape and scale. Tyler and Wheatcraft (1992) derived the particle size distribution based on Equation (2-5). The expression is:

$$\frac{M(d_s < d)}{M_T} = 1 - (\frac{d}{\lambda_m})^{3-D_s} \qquad (2\text{-}6)$$

where M_T is the total mass of soil particles, λ_m is a soil constant which can be easily evaluated if the maximum particle size is known, denoted as $d_{s\max}$. It follows that $M(d_{s\max} < d)/M_T = 0$ and λ_m is equal to $d_{s\max}$. Treating $d_{s\max}$ as an upper boundary and $d_{s\min}$ (minimum particle size) as a lower boundary, Equation (2-6) can be expanded as (Russell 2011):

$$\%M(d_s < d) = 100\left(\frac{d_s^{3-D_s} - d_{s\min}^{3-D_s}}{d_{s\max}^{3-D_s} - d_{s\min}^{3-D_s}}\right) \quad (2\text{-}7)$$

When $d_{s\max} \gg d_{s\min}$ a plot of the logarithm of $\%M(d_s < d)$ versus the logarithm of d produces a linear relationship with a slope $3 - D_s$, as shown in Figure 2-3 (the original particle size distribution is shown in Figure 2-2).

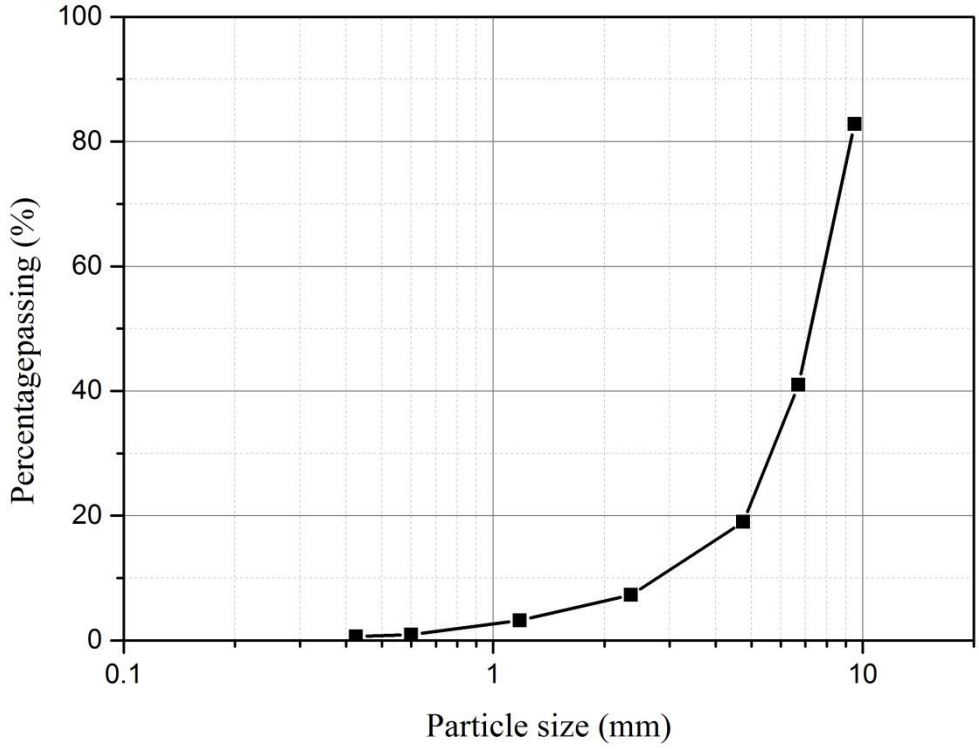

Figure 2-2 Particle size distribution curve of gravel-sand mixtures with fractal size distribution.

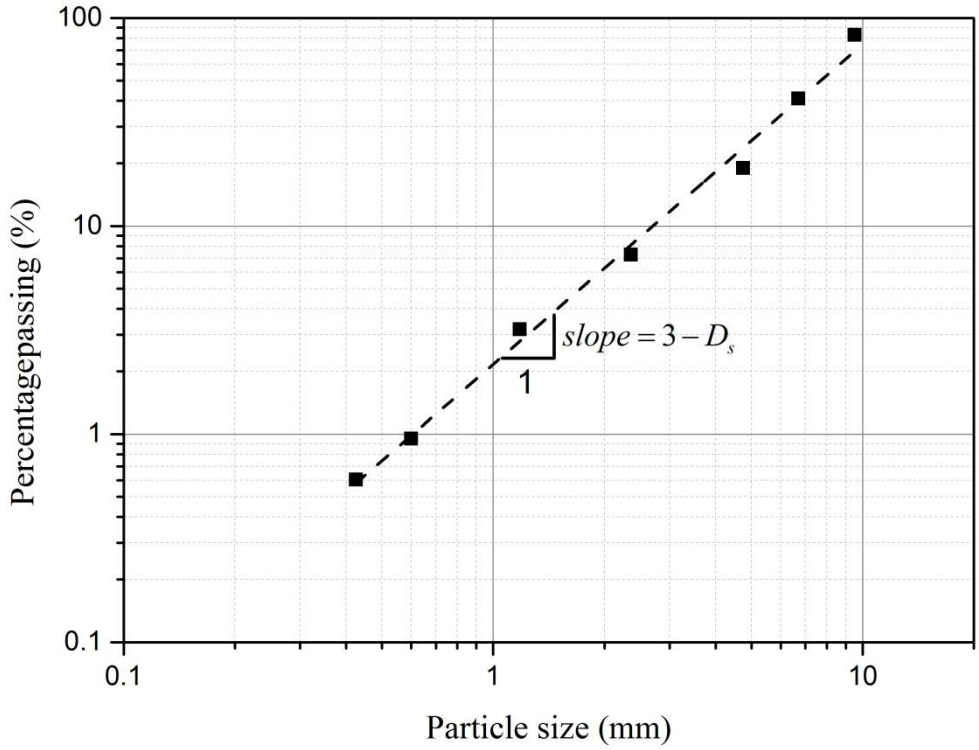

Figure 2-3 Particle size distribution for gravel-sand mixture with fractal size distribution on double logarithm plots.

For gap-graded soils (Figure 2-4) in which two fractal sets can describe the size distributions, the complete particle size distribution curve may be expressed as (Russell 2011):

$$\begin{aligned} &1-R_c\frac{d_{sc\max}^{3-D_{sc}}-d_s^{3-D_{sc}}}{d_{sc\max}^{3-D_{sc}}-d_{sc\min}^{3-D_{sc}}} && \textit{Coarse fraction, for } d_{sc\min}<d_s<d_{sc\max}\\ &1-R_c-(1-R_c)\frac{d_{sf\max}^{3-D_{sf}}-d_s^{3-D_{sf}}}{d_{sf\max}^{3-D_{sf}}-d_{sf\min}^{3-D_{sf}}} && \textit{Fine Fraction, for } d_{sf\min}<d_s<d_{sf\max} \end{aligned} \quad (2\text{-}8)$$

in which D_{sc} and D_{sf} are the fractal dimensions of the coarse fraction and fine fraction of the soil mixture, respectively, obtained from the rescaled double-log plot of each soil's particle size distribution; d_{sc} and d_{sf} are the sizes of coarse particles and fine particles, respectively; the subscripts min and max represent the minimum and maximum particle sizes; and R_c is the mass

ratio of the coarse fraction to the total mass of soil mixture. In Figure 2-4, if $d_{sf\ \max} > d_{sc\ \min}$, the tail of the coarse fraction will overlap the beginning part of the fine fraction; if $d_{sf\ \max} = d_{sc\ \min}$, two fractions will be connected perfectly; if $d_{sf\ \max} < d_{sc\ \min}$, there will be a deficiency between $d_{sf\ \max}$ and $d_{sc\ \min}$.

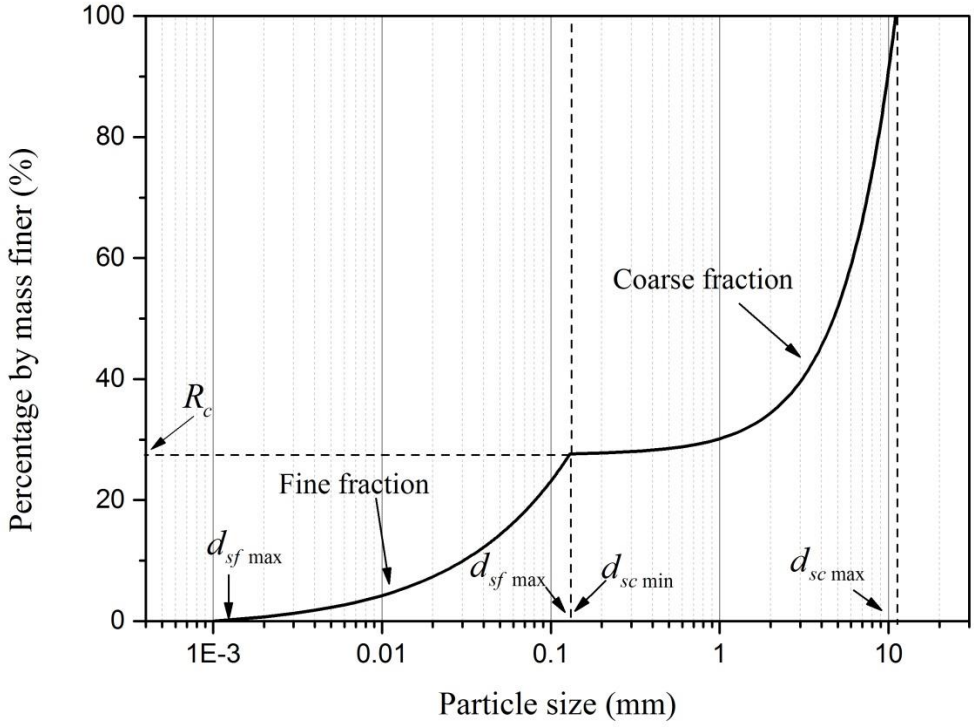

Figure 2-4 Schematic diagram of the internal erosion triaxial testing system.

All above expressions have assumed that particle density is constant over all scales for a soil with fractal particle size distribution. The shape of the particle does not necessarily have to be spherical if a shape factor is introduced.

Fractals and pore size distributions

Perfect and Kay (1995) and Perfect (1997) reviewed studies on the fractal characteristics of soil and rock and suggested that particle and pore size distributions in naturally forming and artificial soils may be characterized mathematically using fractals.

Tyler and Wheatcraft (1989) presented a theoretical investigation correlating the fitting parameter in the Arya and Paris (1981) soil-water retention model to the pore geometry and other physical properties of the soil. They suggested that the exponent in Arya and Paris's model is equal to the fractal dimension of the pore size distribution and may be linked to the fractal dimension of the particle size distribution which is more easily measured.

Hunt and Gee (2002) used a critical path analysis to calculate the unsaturated hydraulic conductivity of soils with pore spaces which can be described using fractals. With the hypothesis that the ratios of maximum and minimum particle and pore sizes are equal, they concluded that soils which exhibit a bimodal fractal particle-size distribution may require two fractal dimensions to characterize the pore size distributions over different size ranges.

To test whether or not the same fractal dimension can be used to describe the pore and particle size distributions, Wang et al. (2005) compared the fractal dimensions obtained from soil-water retention curves and fractal dimensions of particle sizes and concluded that the fractal dimensions obtained from soil water-retention curves were smaller than those from particle sizes. The fractal dimensions of pore sizes and particle sizes were clearly different.

Yu et al. (2009) summarized some fundamental characteristics of fractal porous media, linking the fractal particle and pore size distribution, particle or pore density functions and the fractal dimensions for solid and pore phases. In particular, they reviewed and discussed the geometric porosities versus the fractal dimensions and microstructures of porous media. They indicated that it is likely that the ratios between maximum and minimum particle and pore sizes are different, and thus the fractal dimensions for particle and pore sizes are also to be different as well.

Russell (2010, 2011) linked the particle and pore sizes by assuming that the particle and pore surface areas are equal. It follows that:

$$\left(\frac{d_{p\min}}{d_{p\max}}\right)^{2-D_p} = \left(\frac{d_{s\min}}{d_{s\max}}\right)^{2-D_s} \qquad (2\text{-}9)$$

where d_p and d_s are pore and particle sizes, the subscripts min and max indicate the minimum and maximum pore or particle size, D_p and D_s are fractal dimensions of pore and particle size, respectively. This equation indicates that:

$$D_p = 2 + (D_s - 2)\frac{\ln(d_{s\min}/d_{s\max})}{\ln(d_{p\min}/d_{p\max})} \qquad (2\text{-}10)$$

or

$$d_{p\min} = d_{p\max}\left(\frac{d_{s\min}}{d_{s\max}}\right)^{\frac{2-D_s}{2-D_p}} \qquad (2\text{-}11)$$

Russell (2011) found that, as a material with a fractal particle size distributions is formed by adding successively smaller particles, as done by Dodds and Weitz (2002), the maximum pore size at any stage the formation is proportional to the total number of particles when raised to the power $-(3-D_s)$. Since the number of pores or particles being of any size larger than a certain size can be characterized using Equation (2-3), it follows that:

$$d_{p\max} = Cd_{s\max}\left(\frac{d_{s\min}}{d_{s\max}}\right)^{-(3-D_s)} \quad (2\text{-}12)$$

where C is a dimensionless material constant. This is the most theoretically rigorous link between pore and particle sizes. This link has been applied in a derivation of a compression line for soils with changing grading (Russell 2011) and in definitions of soil-water characteristics curves (Russell 2014; Russell and Buzzi 2012; Vo et al. 2016).

2.4 CONSTITUTIVE MODELLING CONSIDERING INTERNAL EROSION AND CHANGING PARTICLE SIZE DISTRIBUTION

A particle size distribution change, also referred to as a grading change, may result from particle breakage or internal erosion during engineering applications. Particle breakage increases the content of fine particles while internal erosion removes fine particles. In engineering practice, the changes in grading are irreversible and thus the soil that exists in engineering constructions is quite different from the soil that was there at the beginning. The soil properties will also be altered.

Daouadji et al. (2001) proposed an elastoplastic constitutive model for the stress-strain behavior of granular soils when particle crushing occurs. The position of critical state line in the compression plane was related to the level of energy consumed during particle crushing. That the critical state line move downwards as a result of the increase in the fines contents due to particle crushing.

Muir Wood (2007) introduced the concept of a grading state index, I_G, to describe the change in the particle size distribution due to particle crushing or internal erosion. The grading state index was used to characterize the position of current grading relative to a single-sized particles and a fractal particle size distribution. The value is the ratio between the area under the current particle

size distribution curve and the area between the two extremes, as shown in Figure 2-5. It varies from 0 to 1 as the soil grading changes from single sized particles to the fractal limiting condition.

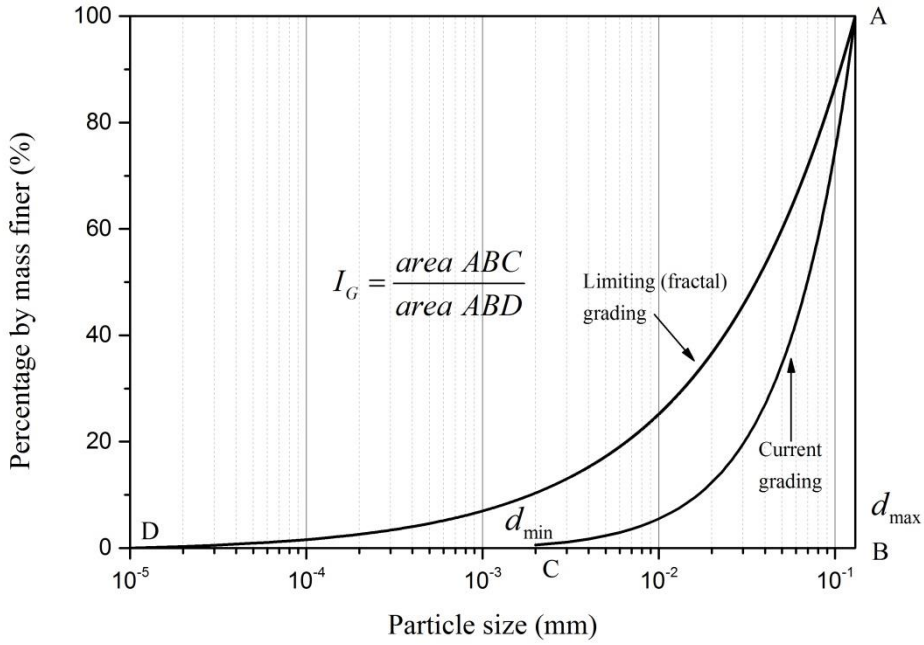

Figure 2-5 Grading state index, after Muir Wood (2007).

Muir Wood and Maeda (2008) conducted DEM analyze and confirmed that the grading of a granular material has a first-order influence on the critical state parameters as it is directly related to the particle packing. They concluded that crushing itself does not cause any change in specific volume of soil but, its subsequent mechanical responses are influenced by the change in constitutive parameters and may lead to changes in volume. They also concluded that changing the grading, either by particle crushing or internal erosion, causes the granular material to seek the critical state line appropriate to the current grading, as shown in Figure 2-6. Specifically, breakage or crushing of soil particles may result in a critical state line location lower than the

original position while erosion may result in critical state line location higher than the original position.

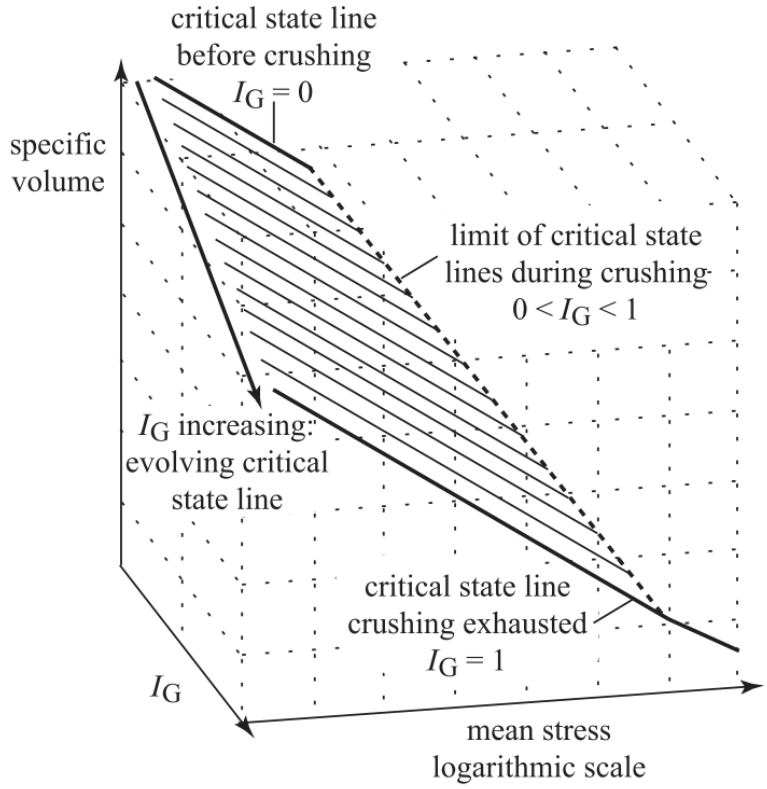

Figure 2-6 Critical state surface in space of mean stress, grading state index, and specific volume (Muir Wood and Maeda 2008).

Muir Wood et al. (2010) proposed a constitutive model capturing the mechanical influences of internal erosion at a certain stress state. They proposed a linear relationship between specific volume decrease and the change in grading for soils while maintaining linear particle size distributions in double logarithmic plots. The change in critical state line due to internal erosion was also related to the change in grading state index, indicating the critical state line was a function of the grading state index and the current stress. The influences of internal erosion on strain and the available strength during internal erosion were evaluated, extending the Severn-Trent model (Gajo and Muir Wood 1999) by incorporating a second plastic mechanism. It

captures incorporates the effects of the changing grading and describes how the internal erosion activates distortional deformation and volumetric compression during erosion. They focused on the mechanical influences of internal erosion on soils at constant stress states. However, most experimental investigations have been more concerned about the stress-strain behaviors of soil having subjected to internal erosion during shearing with a changing stress state. In Muir Wood et al. (2010) model, the shape of the particle size distribution was less important than the maximum and minimum particle sizes because once the maximum and minimum particle sizes are given a linear relation on double logarithmic plots was assumed. Besides, they assumed that the smallest particles were removed first during erosion. However, the shape of particle size distribution is known to be crucial to the erodibility of soils.

Another model which used the grading index as an important constitutive property to model the mechanical influences of particle crushing was proposed by Kikumoto et al. (2010). They linked the grading state index to the minimum and maximum specific volumes so that the change of the critical state line due to particle crushing could be described mathematically. Consequently, the state parameter could also be expressed as a function of the grading state index. The Severn-Trent model, in which the critical state line and state parameter act to describe the evolution of strength, was extended to include the effects of changing grading due to particle crushing. A three-dimensional critical state surface in the three-dimensional mean effective stress-grading state index-specific volume was thus proposed. They concluded that the effect of crushing or breakage was to shift the critical state line and compression line downwards in the compression plane because a soil material with a broader particle size distribution is able to pack more efficiently. According to their simulation of undrained triaxial compression tests, the effects of particle crushing on loose samples are negligible because the test has to end up on critical state line at a low stress level. The key effects of particle crushing on dense sands include: contractive initial behavior with mean effective stress decreasing, followed by volumetric dilation, changes into mean effective stress increasing after particle crushing.

Hicher (2013) proposed a micro-mechanical model to study the mechanical behavior of granular soils subjected to internal erosion based on a homogenization procedure for deriving the stress-strain relationships of a granular material from stresses and strains at the particle level. The numerical results showed that the removal of the fine particles leads to a decrease in sliding resistance of each interparticle contact and consequently, local deformation occurs. The numerical results showed similar trends with the results from DEM. However, more experimental studies on mechanical consequences of internal erosion are needed.

Shire et al. (2014) used discrete element modeling to analyze the fabric and effective stress distribution within gap-graded soils with different erodibility. It is found that the fines content, soil grading and relative density have an influence on the stress distribution.

Yang et al. (2019) studied the effect of the changing porosity and fines content due to internal erosion and developed a elastoplastic constitutive model. This model has been applied to study a dike foundation that had subjected to internal erosion.

Wang et al. (2019) used a subloading Cam-clay model to simulate the mechanical behavior of soils having been subjected to internal erosion. The initial stress states and the slope of normal compression line are two important parameters in this model and the value of these parameters were obtained from back analysis.

2.5 SUMMARY

Significant gaps still remain in the conducting triaxial test on soils with homogeneous post-erosion particle size distribution; the understanding of the mechanical consequences of internal erosion on gap-graded soils with homogeneous post-erosion particle size distribution; the

relationship between particle removal and particle size distribution; the fractal characteristics of a gap-graded soil before and after erosion; the link between particle removal and void ratio of soils; the application of existing fractal theory to mechanical consequences of internal erosion; and modelling the soil behavior subjected to internal erosion.

CHAPTER 3 DETAILS OF THE TEST SOIL AND A PROCEDURE TO OBTAIN HOMOGENEOUS POST-EROSION PARTICLE SIZE DISTRIBUTIONS IN TRIAXIAL EROSION TESTS

3.1 INTRODUCTION

3.1.1 Overview

This Chapter comprises seven main sections in addition to this introduction. In Section 3.2 a summary of limitations of current studies involving triaxial erosion tests is given. In Section 3.3 the triaxial erosion testing apparatus used here to study the erosion characteristics of soils and the stress-strain behavior of soils having been subjected to internal erosion is presented. In Section 3.4 the engineering properties of the soil used here are detailed. In Section 3.5 a conventional sample formation procedure is outlined. In Section 3.6 a new technique is proposed for the formation of soil samples for erosion testing that have homogeneous post-erosion particle size distributions. The differences in stress-strain behaviors of soil samples formed by the new technique and the more commonly used conventional technique will be highlighted, confirming the sample's homogeneity influences the results are detailed in Section 3.7. Section 3.8 presents a discussion and conclusion.

Most of the contents of this chapter are contained in a recently published journal article: The influence of particle size distribution homogeneity on the shearing of soils having been subjected to internal erosion. Accepted by Canadian Geotechnical Journal on 16/11/2019.

3.1.2 Definition of the triaxial erosion test

A modified triaxial apparatus, incorporating a drainage system that enables internal erosion and particle removal in saturated and consolidated soil samples under certain confining pressures, is used in triaxial erosion tests. Triaxial erosion tests are commonly conducted to study the initiation, rate of progression, characteristics (including erosion rate, flow rate, turbidity of effluent, cumulative eroded mass loss, pore pressure), change in sample volume, post-erosion particle size distribution and, most importantly, the mechanical consequences of internal erosion. The testing procedure broadly contains three steps: *i*) internal erosion of the sample (the seepage test), *ii*) the triaxial test and *iii*) a post-erosion microstructure and particle size distribution analysis.

3.2 LIMITATIONS OF EXISTING STUDIES

While the results of triaxial erosion tests are a major interest to dam owners and their engineering advisors, providing some guidance on what strength changes and alterations to the stress-strain behavior of the soil can be expected, they have a limitation that restricts their usefulness. The limitation comes through the use of eroded samples which have heterogeneous post-erosion particle size distributions.

Most researchers have reported that the internal erosion processes used in their studies usually lead to a heterogeneity in the post-erosion particle size distributions through the sample. Kenney and Lau (1985) conducted seepage tests on granular soils and found that downward flow resulted in the formation of a top transition zone (where the particles are the coarsest and the concentration of fine particles is the lowest), a central homogeneous zone and a bottom transition zone (where the concentration of fine particles is the largest). Chang and Zhang (2011) and Ke and Takahashi (2014b) also reported heterogeneous post-erosion particle size distributions for samples subjected to downward flow that were consistent with Kenney and Lau

(1985). This heterogeneity of the particle size distribution may introduce other heterogeneities related to void ratio, state parameter, soil deformation and load distribution throughout a sample, meaning the stress-strain behaviors and strengths measured at the sample boundaries are not representative of what is happening at critical sections inside the samples.

In routine triaxial testing, where erosion is not a concern, great attention is devoted to producing homogenous samples prior to determinations of strength and stress-strain behaviors to maximize the relevance and usefulness of the results. This has led to the widespread use of the "undercompaction method" (Ladd 1978) to form soil samples with homogenous void ratios and densities. Starting with a homogenous sample means that the observed mechanical responses can be linked, reliably and directly, to measures of state including void ratio and state parameter. The particle size distribution is also an important measure of state that must feature in an understanding of the mechanical responses. For example it has a first-order influence on critical state parameters (Been and Jefferies 1985; Gajo and Muir Wood 1999; Kikumoto et al. 2010; Muir Wood 2004; Muir Wood and Belkheir 1994). Despite the importance of sample homogeneity when triaxial testing too many erosion studies have been conducted using samples that are heterogeneous during shearing.

3.3 TRIAXIAL EROSION TESTING APPARATUS

A modified triaxial apparatus is used, able to subject samples to different amounts of internal erosion by upward or downward flow prior to testing. The apparatus consists of a triaxial compression testing system, a drainage system enabling water to seep through samples in an upward or downward direction, a constant head water tank to drive the seepage and a system to collect the water and eroded particles once they have exited the soil. The system is broadly similar to others (Chang and Zhang 2011; Ke and Takahashi 2014b; Ouyang and Takahashi 2015; Xiao and Shwiyhat 2012). A schematic illustration is shown in Figure 3-1.

3.3.1 Triaxial system

The triaxial testing apparatus, used to test cylindrical samples 200 mm in diameter and 400 mm in height, is displacement-controlled. A motorized load frame applies an axial load to samples. The drive unit has a multispeed gearbox and gives constant rates of axial displacement down to speeds of 0.0001 mm/min. The resulting axial load is measured by a submersible load cell at chosen time intervals. The load cell has a capacity of 50 kN and a precision of 0.025 N. The axial displacement of the sample during shearing is measured using a linear variable differential transducer (LVDT) with a precision of 0.0001 mm. The cell pressure and pore pressure, applied to test samples via air-water interface bladders, may be controlled during saturation and monotonic compression. The axial load cell, pressure transducers, and LVDT are linked to a PC through a desktop mounting kit. The automatic logging of test data is controlled by a program with an interactive visual interface running on this PC. Figure 3-2 shows a photo of the triaxial apparatus.

3.3.2 Drainage system

The base pedestal and top-cap contain funnel-shaped depressions to enable seepage water containing soil particles to exit a sample through its ends and pass into a collection system. Perforated stainless steel discs cover each funnel-shaped depression and provide and act as rigid base and top sample boundaries. The perforations are circular, 5mm in diameter, and make a grid pattern with a center-to-center spacing of about 7 mm. The 5 mm perforation size is sufficiently large to prevent clogging by fine particles and is sufficiently small to prevent coarse particles from passing thus preventing the collapse of a sample. The largest eroded particle is less than (and usually much less than) 15% of the maximum particle size (Wan 2009). The equivalent maximum particle diameter is 13 mm in this study. All flow channels and fittings have an internal diameter of 7.5 mm. Seepage water can be introduced and passed through samples in both upward and downward directions to cause particle removal under a range of confining

stresses and hydraulic gradients prior to shearing. Figure 3-3 shows a photo of perforated stainless steel disc.

Passing water in two directions enables a more homogeneous sample to be achieved prior to subsequent triaxial testing than was found to be possible by Bendahmane et al. (2008), Chang and Zhang (2011), Ke and Takahashi (2014b), whose equipment permitted flow only in one direction, resulting in significant variations in particle size distributions along the lengths of the samples. Moffat et al. (2011) observed that a downward flow through soil causes the vertical effective stress to increase while an upward flow causes the vertical effective stress to decrease. Chang and Zhang (2011) attributed the non-uniformity of fine particle concentrations within the eroded soil to the effective stress change accompanying unidirectional seepage.

Plastic tubes in the drainage system had 5 mm diameter and thick walls to ensure high stiffness to minimize errors in the measurements of axial strain and deviator strain.

3.3.3 Constant water head and the effluent collection system

The seepage water is supplied via a constant head tank. The constant head tank comprises a watertight barrel fitted with an inlet ballcock valve such that continuous water supply can be achieved. In the tests reported in this chapter the water tank is located 1.24 m above the base of the sample, with the water exiting the sample being collected in containers level with the base, corresponding to an average hydraulic gradient i of 3.1 across the sample. Higher or lower hydraulic gradients can be achieved by raising or lowering the position of the constant head tank.

When erosion is detected, and particles begin to wash out from the sample, the collected water is allowed to stand for a period of time so that suspended soil particles settle out from the water. The flow rate and the rate of increase of mass of eroded soil are determined.

Axial deformation of a sample during erosion, if it occurs, is measured by reading the vertical separation of the laser mark generated by a fixed laser pointer in front of the triaxial cell.

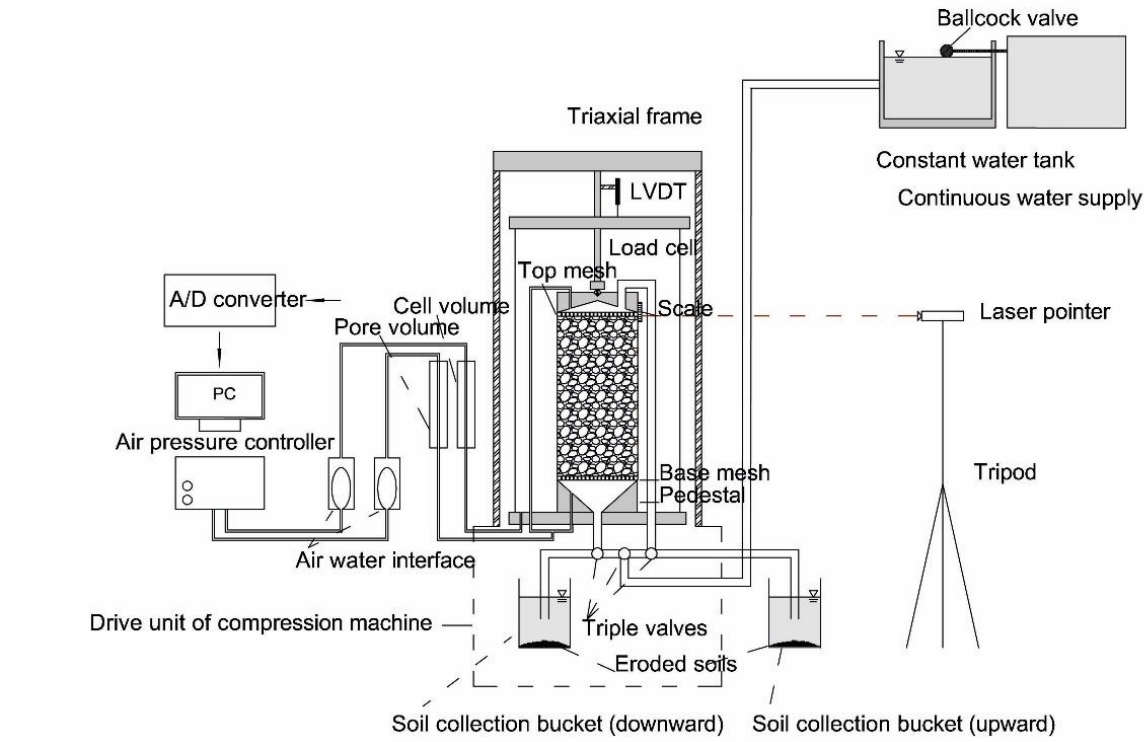

Figure 3-1 Schematic diagram of the internal erosion triaxial testing system.

Figure 3-2 A photo of triaxial erosion apparatus.

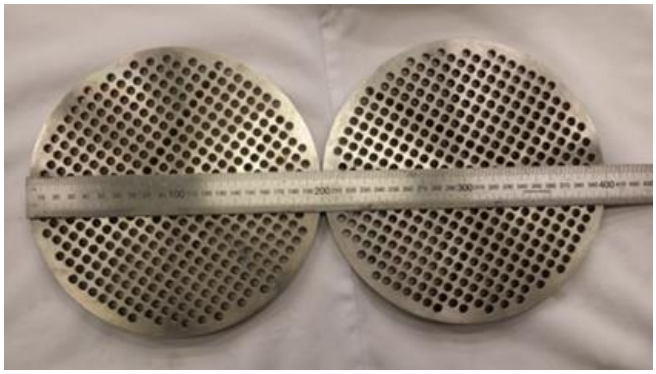

Figure 3-3 A photo of perforated stainless steel discs.

3.4 TEST SOIL AND SAMPLE PREPARATION

3.4.1 Test soil

The soil used in this study is a mixture of three base materials comprising silt, sand and gravel-sized particles in different proportions. The three base materials are referred to as silica 60G, 5 mm basalt and 10 mm basalt. The particle size distribution of each base material is shown in Figure 3-4. They are mixed in the proportions 0.26:0.10:0.64 by dry mass to produce a gap-graded soil for testing, having a gravel content of 58.2%, with a full particle size distribution also shown in Figure 3-4.

The maximum particle size is 13 mm, meaning boundary effects in the 200 mm diameter samples remain negligible as sample diameter to maximum particle size ratio is always lager than 10 (Holtz and Gibbs 1956). The soils have been selected to ensure high practical relevance. Silt, sand and gravel are typical constituents of many soils used in the construction of water retaining structures. Previous studies have shown that cohesionless gap-graded soils are internally unstable to internal erosion under practically relevant combinations of hydraulic gradient, confining stress and compaction density (Foster and Fell 1999; Lafleur et al. 1989; Wan 2006; Wan and Fell 2008). The erodibility of the test soil may be inferred using one of many empirical criteria based on the particle size distribution as discussed in Section 3.5.2. This particular gap-graded soil is selected to ensure that erosion will occur, noting that soils having gravel contents of around 60% (or larger) are internally unstable (Wan 2009). The gravel particles act as the primary load-bearing skeleton in the soil, enabling fine particles to be washed out from the spaces around the gravel. Other physical properties of the test soil are summarized in Table 3-1.

Table 3-1 Physical properties of the gap-graded test soil

Physical property	Value
d_{90}, mm	10.1
d_{60}, mm	6.9
Mean particle size d_{50}, mm	5.7
d_{30}, mm	0.97
d_{15}, mm	0.04
Effective particle size d_{10}, mm	0.02
Uniformity coefficient C_u	284.6
Curvature coefficient C_c	5.6
$h' = d_{90} / d_{60}$	1.5
$h'' = d_{90} / d_{15}$	232
Specific gravity, G_s	2.73
Minimum dry density, g / cm^3	1.79
Maximum dry density, g / cm^3	2.49
USCS (ASTM D2487-11)	GM
Particle description	sub-angular

d_x denotes the particle size for which $x\%$ of the soil by mass comprises particles of that size or smaller

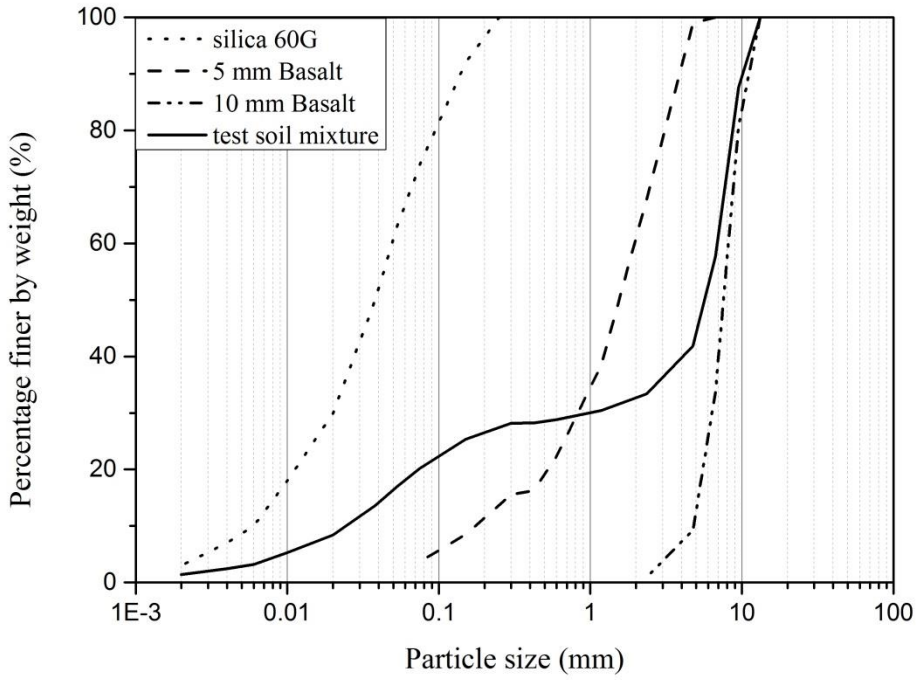

Figure 3-4 Particle size distributions of the test soil and its constituents.

3.4.2 The instability of the test soil

Soils that are vulnerable to internal erosion are internally unstable. Over the years, extensive studies on the instability of soils have been carried out by researchers and engineers. Some of them developed quantitative criteria based on the particle size distribution to identify which soils are susceptible to internal erosion under a range of confining stress states and hydraulic gradients. These criteria will be introduced here so the potential erodibility of the test soil can be evaluated.

U.S. Army Corps of Engineers (1953)

Sherman (1953), from the U.S. Army Corps of Engineers, performed downward flow seepage tests to determine the effectiveness of gravel and concrete sands as filter materials for base materials in embankments and dams. A criterion was proposed that internal erosion would occur

in a cohesive filter materials if: (1) the seepage is turbulent flow; (2) the applied hydraulic gradient is higher than 5; and (3) the coefficient of uniformity (C_u) is greater than 20.

According to Table 3-1, the C_u of the test soil is 284.6, greater than 20, suggesting it will be internally unstable.

Istomina (1957)

According to Kovács (2011), Istomina (1957) proposed a criterion in terms of C_u:

$$\begin{array}{ll} \textit{No suffusion if} & C_u < 10 \\ \textit{Transition condition} & 10 < C_u \le 20 \\ \textit{Suffusion is liable if} & C_u \ge 20 \end{array} \qquad (3\text{-}1)$$

The testing soil is likely to be internally unstable according to Istomina (1957)'s criterion.

Lubochkov (1965)

According to Kovács (2011), Lubochkov (1965) developed an analytical method to identify the range of particle sizes which are susceptible to internal erosion, based on laboratory tests and observations. It was assumed that a soil layer is not susceptible to suffusion if the particle size distribution does not a certain criterion. This criterion is expressed in terms of ratios of particle sizes (denoted as D rather than d) and S values (denoting vertical positions on the particle size distribution curve) as follows:

$$\begin{array}{l} \dfrac{\Delta S_1 / \Delta S_2}{4} \le 1; \textit{if } \dfrac{D_{n-1}}{D_n} = \dfrac{D_n}{D_{n+1}} = 10 \ (\textit{tolerance safety factor } 1.0); \\ \dfrac{\Delta S_1 / \Delta S_2}{2.6} \le 1; \textit{if } \dfrac{D_{n-1}}{D_n} = \dfrac{D_n}{D_{n+1}} = 5 \ (\textit{tolerance safety factor } 1.5); \\ \dfrac{\Delta S_1 / \Delta S_2}{1.7} \le 1; \textit{if } \dfrac{D_{n-1}}{D_n} = \dfrac{D_n}{D_{n+1}} = 2.5 \ (\textit{tolerance safety factor } 2.3); \end{array} \qquad (3\text{-}2)$$

where D_n is an arbitrary particle size, D_{n+1} and D_{n-1} are determined from D_n by dividing or multiplying it by 10, 5 or 2.5 and $\Delta S_1 = S_{n-1} - S_n$ is the (vertical) difference between cumulative mass for particle sizes D_{n-1} and D_n. Similarly, $\Delta S_2 = S_n - S_{n+1}$ is the vertical difference between cumulative mass for particle sizes D_n and D_{n+1}. Figure 3-5 shows an example of the application of Lubochkov (1965)'s method.

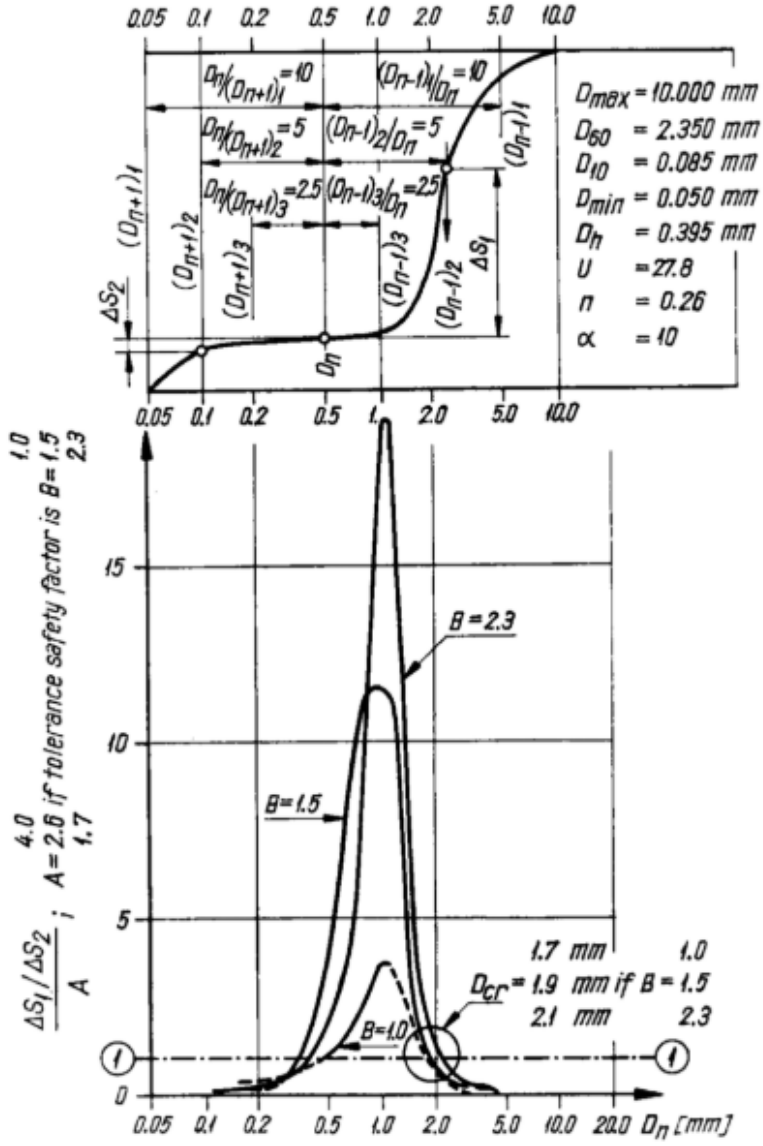

Figure 3-5 Lubochkov's method to determine the instability of soil from Kovács (2011).

For the test soil used here and for $D_n = 0.5$, $D_{n-1} = 5$ and $D_{n+1} = 0.05$, from equation (3-2), the percentage by mass of each size is $S_n = 28.7\%$, $S_{n-1} = 44.1\%$, and $S_{n+1} = 16.3\%$. Then $\Delta S_1 = S_{n-1} - S_n = 15.4\%$ and $\Delta S_2 = S_n - S_{n+1} = 13.3\%$. Since $\frac{D_{n-1}}{D_n} = \frac{D_n}{D_{n+1}} = 10$, and since $\frac{\Delta S_1 / \Delta S_2}{4} = 0.289 < 1$, particles of size 0.5 mm are susceptible to suffusion. By repeating the above calculation steps for a wider range of particle sizes, it can be inferred that the particles that are susceptible to internal erosion have the sizes between 0 mm and 0.75 mm. Therefore, according to Lubochkov (1965), the testing soil is internal unstable and significant numbers of particles smaller than 0.75 mm are erodible, as shown in Figure 3-6.

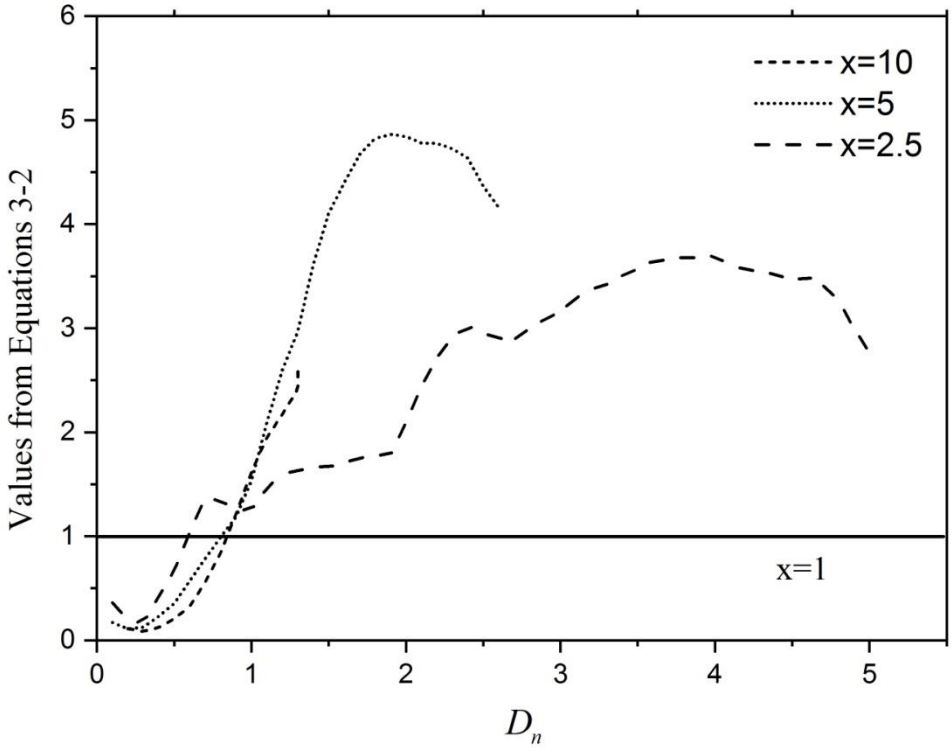

Figure 3-6 Erodibility of the test soil, evaluated by Lubochkov (1965)'s method.

Kezdi (1979)

Kézdi (1979) gave a criterion on a soil's internal stability to suffusion based on Terzaghi et al. (1948)'s filter rule. The soil will remain stable when:

$$(D_{15c} / d_{85f})_{\max} \le 4 \qquad (3\text{-}3)$$

where the subscripts c and f stands for coarse and fine, which is divided by an arbitrary point along the particle size distribution curve, D_{15c} is the particle size for which 15% by mass is finer, d_{85f} is the particle size for which 15% by weight is finer. Kézdi (1979) assumed that a soil that satisfied Equation (3-3) would be self-filtering and, therefore, would be internally stable. As shown in Figure 3-7, the test soil has been split into coarse and fine fractions, separated at $d = 0.3\,mm$, and the particle size distributions have been plotted. D_{15c} and d_{85f} can be read from the plot. The soil is internally unstable as $D_{15c} / d_{85f} = 28 > 4$.

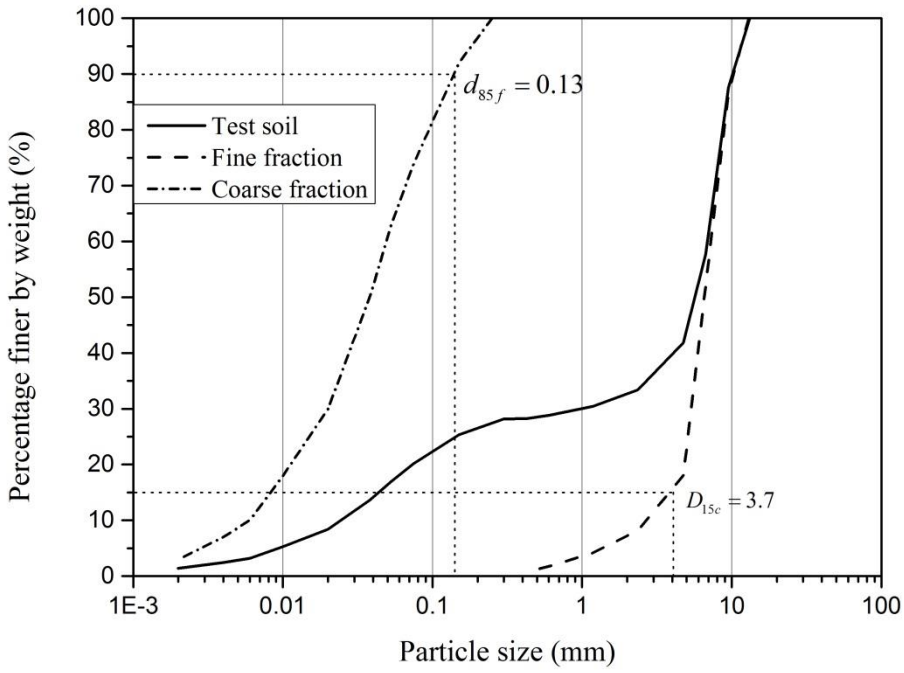

Figure 3-7 Evaluation of erodibility of the test soil using Kézdi (1979)'s method.

Kenney and Lau (1985, 1986)

To study the internal instability of granular materials Kenney and Lau (1985) conducted downward seepage erosion tests on cohesionless soil samples following the basic experimental approached adopted by Sherman (1953). The soil samples were a mixture of sand and gravel with a maximum particle size as large as 100 mm. The diameter of the soil samples was either 580 mm or 245 mm. The soil samples were compacted to 580 mm lengths when they had a diameter of 245 mm, and 860 mm lengths when they had a diameter of 580 mm. 6 out of the 14 tested samples turned out to be internally unstable.

Kenney and Lau (1985, 1986) stated that soil particles finer than size d, which has a mass fraction F, is likely to be transported by seepage out of soil matrix if there is a material deficiency in the size range d to $4d$, which have a weight fraction H. Both F and H can be read from the particle size distribution curve for any arbitrary given particle size d, with $H = F_{4d} - F_d$ and $F = F_d$. Kenney and Lau (1985) plotted the F versus H of the tested samples and suggested that there exists a boundary line $H = 1.3F$. The soil is erodible if part of or all of the $H - F$ combinations are located below the boundary line, as shown in Figure 3-8. For the testing soil, the $H - F$ is plotted in Figure 3-9. The curve goes below the $F = 1.3H$ boundary line and implying that it will be erodible.

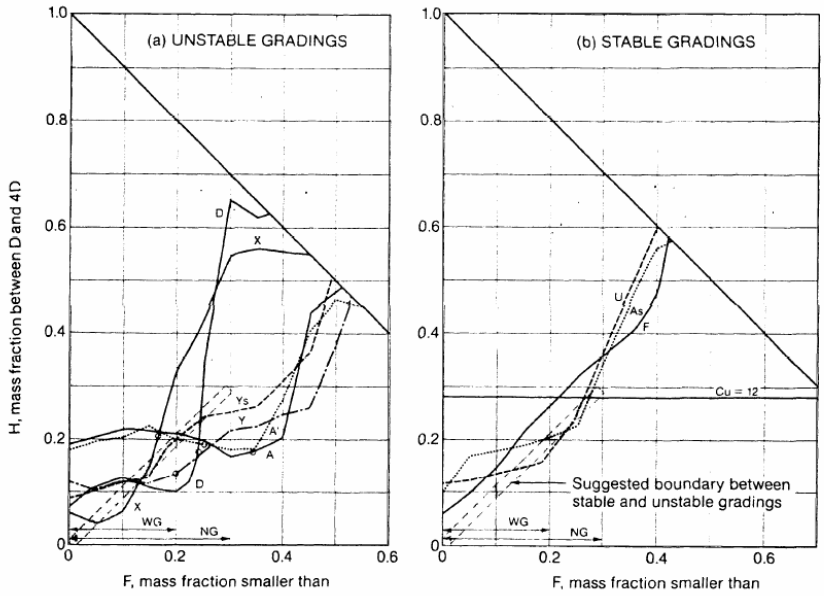

Figure 3-8 Method to evaluate the erodibility of soils (Kenney and Lau (1985))**.**

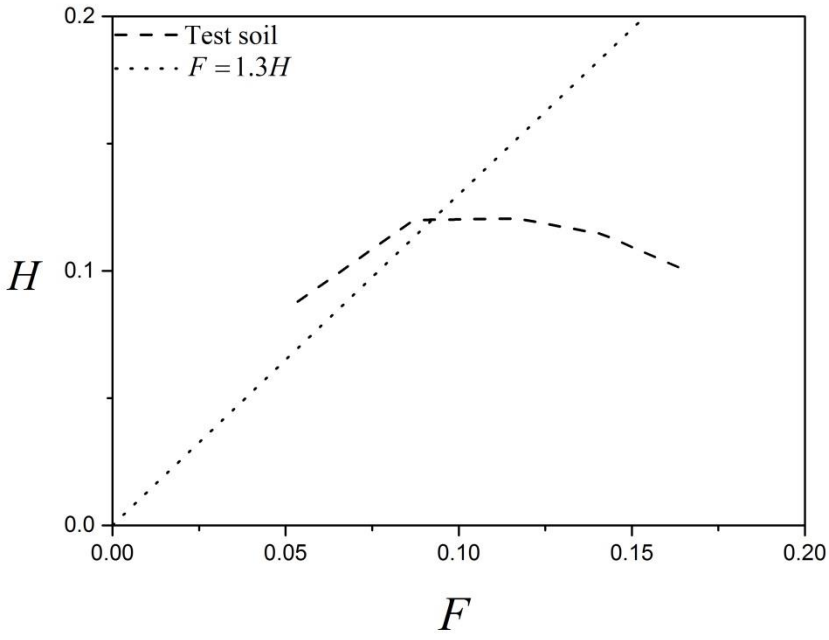

Figure 3-9 Evaluation of erodibility of the test soil using Kenney and Lau (1985)'s method.

Burenkova (1993)

Burenkova (1993) carried out laboratory tests on 22 cohesionless soil samples to examine their internal instability. The soil samples were a mixture of sand and gravel, with the maximum particle size as large as 100 mm, and C_u as large as 200. Burenkova's laboratory tests differ from others' seepage tests. Instead of conducting seepage test Burenkova mixed various sizes of soil particles based on the assumption that the smaller size fraction did not act as part of the soil skeleton if it did not result in a volume increase when mixed with a coarse fraction. The test procedure involved the coarsest particles being poured into a cell and the volume measured. The finer particles were then added into the cell and the volume was measured again. The above procedures were followed until all designed fractions were added. If the volume of the soil sample increased after the mixing of a finer soil fraction, then this finer soil fraction was treated as a part of soil skeleton, otherwise the finer fraction was treated as erodible particles.

According to Burenkova (1993) the erodibility of soil was a direct relation with the conditional factors of uniformity, h' and h'', were defined as $h' = d_{90}/d_{60}$ and $h'' = d_{90}/d_{15}$. The ratio $h' = d_{90}/d_{60}$ represents the slope of the coarse fraction of the grading curve. A higher value indicates a more uniform coarse fraction, which will result in a larger constriction space. The ratio $h'' = d_{90}/d_{15}$ is regarded as a measure of the filter action between the finer part and the coarse part. On the plot of h' versus h'', as shown in Figure 3-10, Burenkova (1993) defined boundary lines separating erodible soils (Zone Ⅰ,Ⅲ), non-erodible soils (Zone Ⅱ), and artificial soils (Zone Ⅳ). The zone for non-erodible soils can be expressed as:

$$0.76\log(h'')+1 < h' < 1.86\log(h'')+1 \qquad (3\text{-}4)$$

However, this method does not have a clear-cut boundary between erodible and non-erodible soils.

According to Burenkova (1993)'s criterion, the test soil is erodible, as shown in Figure 3-11.

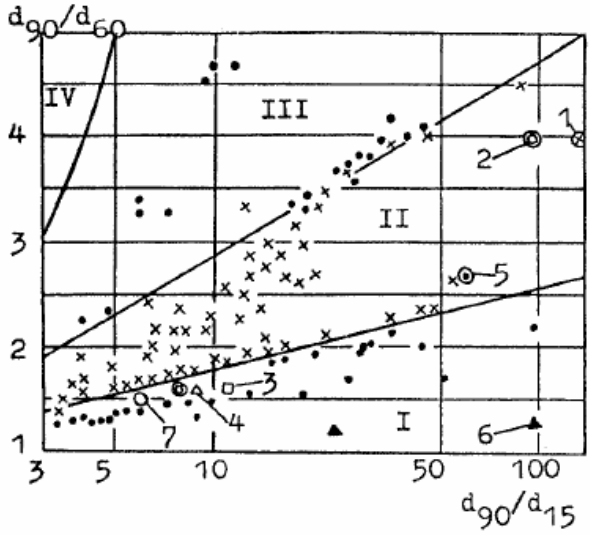

(Zones I and III – Suffusive; Zone II – Non-suffusive; Zone IV – Artificial Soils.)

Figure 3-10 Criterion of erodible and non-erodible soils by Burenkova (1993).

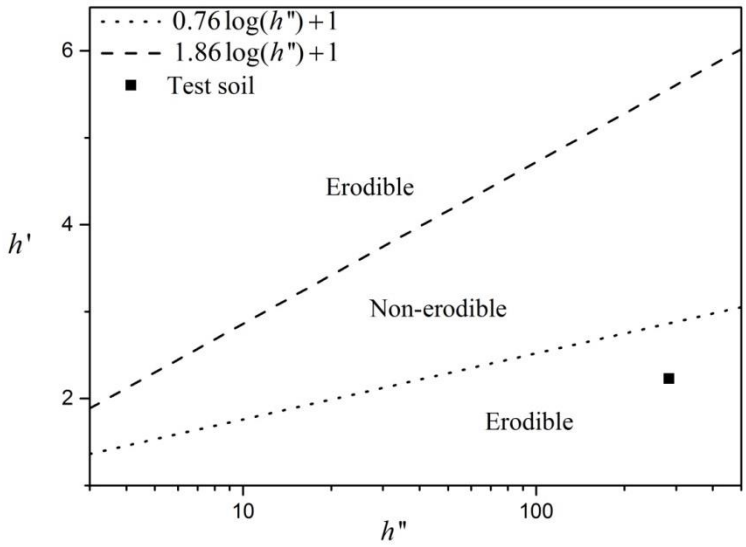

Figure 3-11 Evaluation of the erodibility of the test soil according to Burenkova (1993)'s criterion.

Wan and Fell (2008)

Wan and Fell (2008) modified Burenkova (1993)'s method for silt-sand-gravel soils based on a comprehensive laboratory investigation and by incorporating experimental data of others. It describes a more clear-cut boundary between internal stable and unstable soils.

Wan and Fell (2008) defined probability contours of internal instability based on Burenkova (1993)'s graphical method. The probability contours for silt-sand-gravel soils, with less than 10% clay, are defined by the following equations:

$$P = \exp(Z)/[1-\exp(Z)] \quad (3\text{-}5)$$

$$Z = 3.875\log(h'') - 3.591h' + 2.436 \quad (3\text{-}6)$$

where P represents the probability of internal instability of the soil. The probability contours are plotted in Figure 3-12. It can be seen that the probability of internal instability of the test soil is greater than 95%.

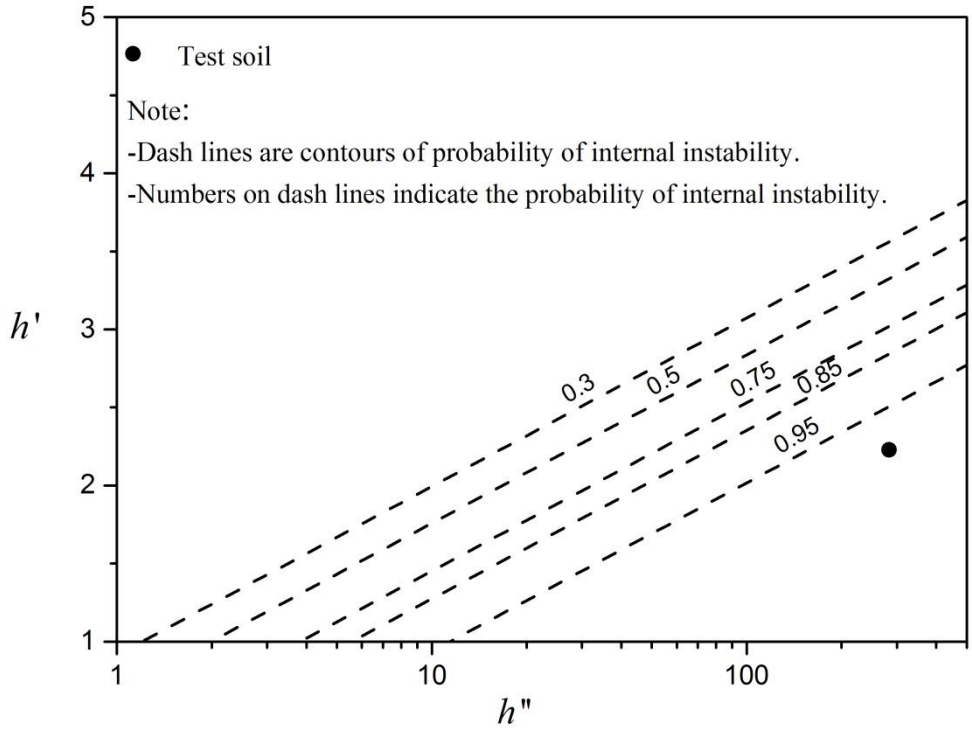

Figure 3-12 Evaluation of the test soil based on the method of Wan and Fell (2008).

The above-mentioned methods to evaluate the erodibility of soils are summarized in Table 3-2. The erodibility of the test soil is expected to erode and be internally unstable.

Table 3-2 The evaluation of the mixture's erodibility using various methods

Criteria	The mixture is internally stable if	Stability of gap-graded soil
U.S. Army (1953)	$C_u < 20$	U
Istomina (1957)	$C_u \le 20$	U
Lubochkov (1965)	$(\Delta S1/\Delta S2)/F \le 1$	U
Kezdi (1979)	$(d_{15c}/d_{85f})_{\max} \le 4$	U
Kenney and Lau (1985, 1986)	$(H/F)_{\min} > 1 (0 < F < 0.2)$	U
Burenkova （1993）	$0.76\log(h'')+1 < h_0 < 1.86\log(h'')+1$	U
Wan and Fell (2008)	$P = \exp(Z)/[1-\exp(Z)]$ $Z = 2.378\log(h'') - 3.648h' + 3.701$	$P > 95\%$

U=unstable; P=probability of internal instability.

3.5 A CONVENTIONAL SAMPLE FORMATION METHOD THAT PRODUCES A HETEROGENEOUS POST-EROSION PARTICLE SIZE DISTRIBUTION

Moist tamping is often used to form the samples for well-graded soils. Here the gap-graded test was formed into samples using this technique. Several thin soil layers were tamped, layer by layer, employing the modified "undercompaction" method of Vo and Russell (2013) to achieve a uniform density. The Vo and Russell method is similar to that of Bradshaw and Baxter (2007). The compaction energy applied to each layer of soil in forming the sample was controlled to achieve a uniform density throughout the sample. An electric Kango percussion hammer fitted with a round steel pad with a diameter of 195 mm, able to cover most of the top surface of the 200 mm diameter soil sample surface and avoid compaction energy losses through contact with the compaction mold, was used to apply compaction energy. During compaction the electric Kango percussion hammer was kept vertical by the operator to make the energy distribution as

even as possible. After the completion of a compaction layer, the top surface was scratched using a steel knife to reduce the effects of compaction layers.

A few trials were conducted on a single layer of soil which weighed one-sixth of the total weight of the soil sample. The relationships between compaction duration and dry density for a single layer, having a moisture content of 7.3%, are obtained as shown in Figure 3-13. Figure 3-14 shows 6 compacted soil layers.

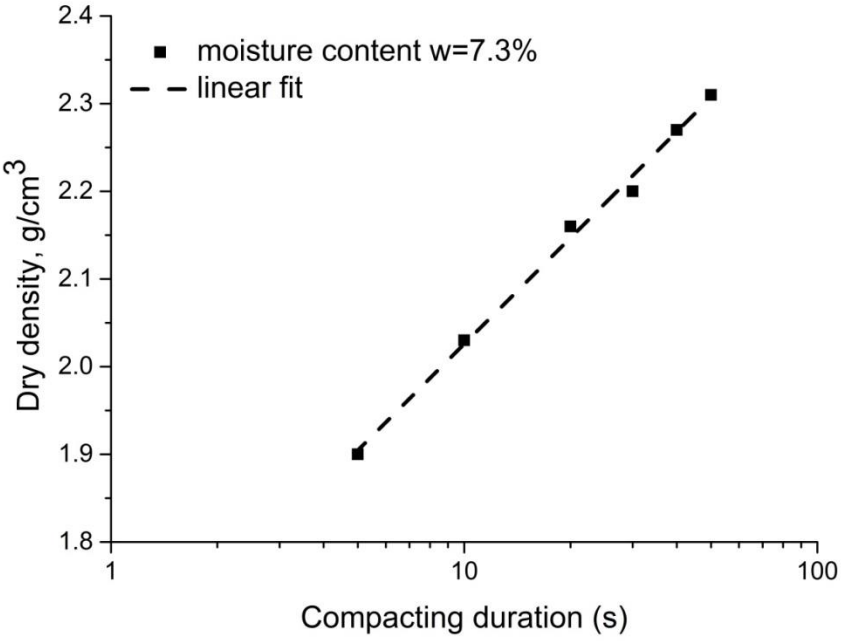

Figure 3-13 Compacting duration versus dry density for the test soil in a single layer of the same thickness used to create the samples.

Figure 3-14 Photo of compaction layers.

According to Skempton and Brogan (1994) and Fell et al. (2003), cohesionless soils compacted to a relative density greater than 65% have a low likelihood of internal erosion. In this study, all the samples were prepared to target a density of 2.08 Mg/m^3 when the moisture content was 7.3%, which corresponds to a relative density of 50%. The corresponding compacting duration for a single layer to reach the target is 14.5 s. Compaction trials on a layered soil showed that, when the top layer was subjected to 14.5 s of compaction, the top layer absorbed 75% of compaction energy, the second layer absorbed 20% of the compaction energy and the bottom layer absorbed 5% of the compaction energy. It follows, using the Vo and Russell (2013) technique, that the compaction times for each layer of a six-layered sample are 10.1, 14.5, 14.6, 14.3, 14.2, 19.3 s (from bottom to top) and application of this series of compaction times will produce a sample with a density of 2.08Mg/m^3 (50% relative density) throughout. The non-monotonic compaction durations for each layer stem from the differing amounts of compaction energy being absorbed and accumulated in layers as a sample is formed. A thin ring-shaped layer of dry Sydney sand was placed on the top of each compacting layer as a mark. Thus the thickness of each compacting layer can be measured. The uniformity of the density of a sample was checked by measuring the thickness of each layer. For each compacted layer the maximum,

minimum and average ratios of actual density to target density were 1.08, 0.99 and 1.03, respectively.

Figure 3-15 shows a photo of a sample seated on the pedestal during sample installation. The top and bottom perforated stainless steel plates (hidden by a membrane) fit well with the pedestal and top cap. Two membranes were used to prevent leakage and puncture of the membrane due to the presence of angular gravel particles. Figure 3-16 shows a sample seated in the triaxial apparatus with consolidation stress.

Figure 3-15 A photo of compacted soil sample with dry sand mark.

Figure 3-16 An example of the installation of a test sample.

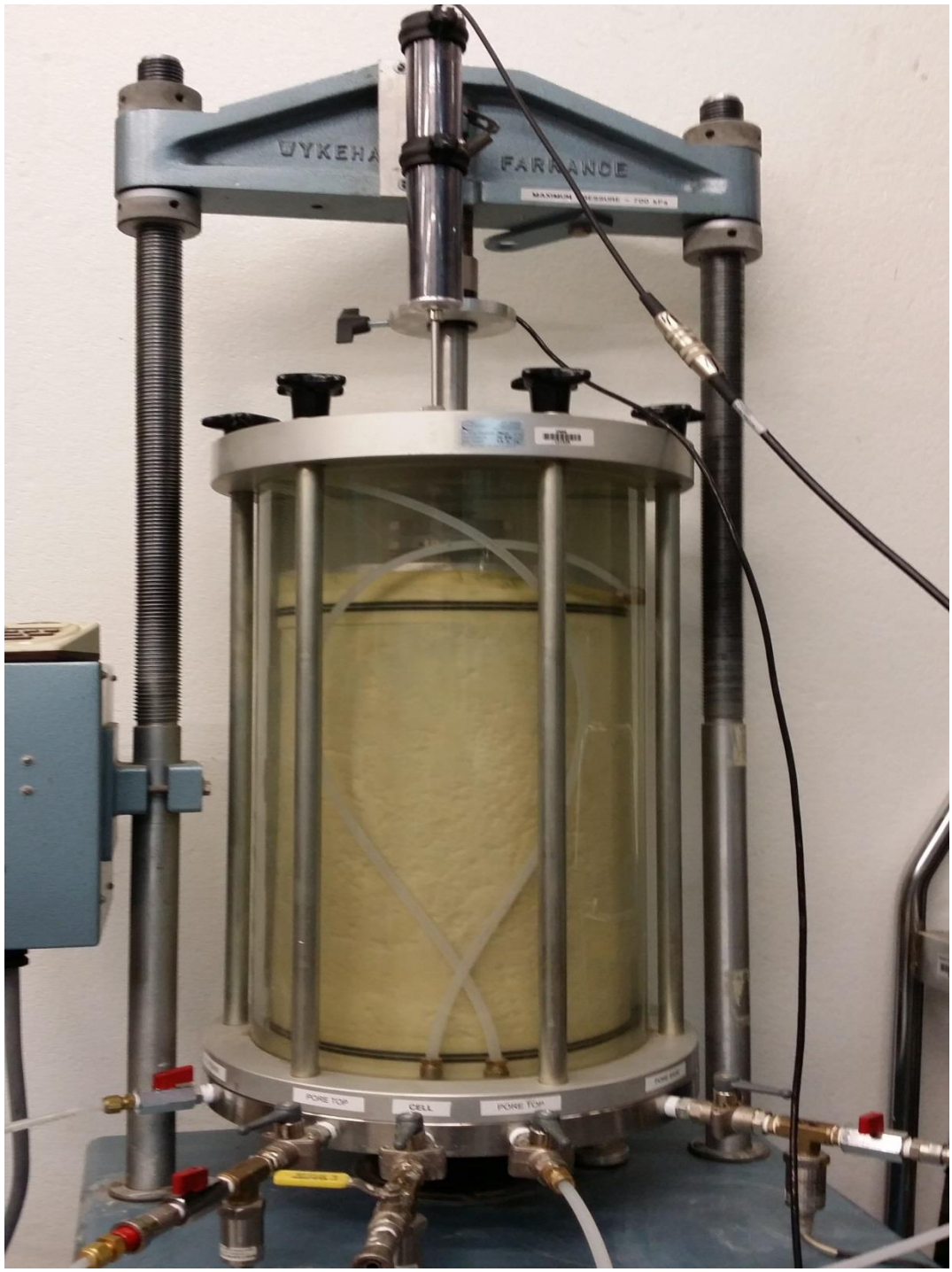

Figure 3-17 A photo of a test sample in the triaxial apparatus.

Eroding a homogeneous sample formed in this way results in heterogeneous particle size distributions in different layers of the sample. To illustrate this consider a typical eroded sample divided into quarters of equal thickness along its length. For this particular sample, the erosion process involved passing 8×10^{-3} m^3 of water upwards through the sample, then 8×10^{-3} m^3 of water downwards, then another 8×10^{-3} m^3 of water upwards, with a hydraulic gradient of 3.1 for each stage. The interval of each erosion stage was about 1 minute. During erosion, each sample was subjected to an isotropic confining stress of 50 kPa. The hydraulic gradient of i = 3.1 is sufficient to initiate and maintain erosion. A constant head tank imposed a pore water pressure of about 10 kPa where water entered a sample. The water pressure was 0 kPa where water exited the sample. Therefore a slight gradient of effective stress exists across a sample during erosion. The 1st quarter is at the sample top, with others numbered sequentially to the sample bottom. The particle size distributions for each quarter after erosion and for the initial condition, determined by wet sieving, are shown in Figure 3-18. Clearly the concentrations of fine particles in each quarter are different. The 4th quarter has a fines concentration and overall particle size distribution that are almost identical to the initial condition. However, the 3rd, 2nd and 1st quarters have progressively smaller concentrations of fine particles. The largest loss of fine particles occurs in the upper (1st) quarter. These observations are very similar to those made by Kenney and Lau (1985), Chang and Zhang (2011) and Ke and Takahashi (2014b).

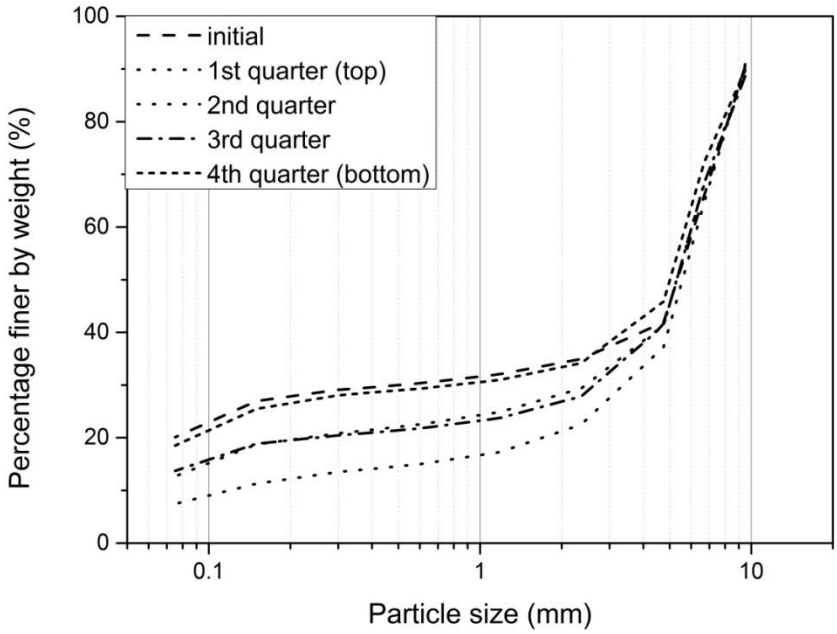

Figure 3-18 Typical post-erosion particle size distributions for when conventional sample preparation is used.

Many factors may give rise to an erosion-induced heterogeneous particle size distribution through a sample. Kenney and Lau (1985) supposed that mobile particles can only travel a certain distance before they redeposit. If the soil sample is longer than the limiting travel distance then heterogeneity in the particle size distribution will result. The deposited particles are not remobilized as seepage continues. The hydraulic gradient along the sample length has altered and internal flow channels have formed such that the driving hydraulic forces are insufficient for their remobilization. Skempton and Brogan (1994), Bendahmane et al. (2008) and Moffat et al. (2011) suggested that heterogeneous effective stress and hydraulic gradient along the sample length during erosion contribute to the resulting heterogeneous particle size distribution. Bendahmane et al. (2008) found the application of a high hydraulic gradient is likely to cause a local pore pressure rise at the flow entering end of a sample and hence a reduction in the consolidation of the sample. At the flow exit end of the sample, the pore water pressure is zero.

In the next section a new sample formation procedure is detailed. It results in a more homogeneous particle size distribution to exist post-erosion.

3.6 A NEW SAMPLE FORMATION PROCEDURE THAT PRODUCES A HOMOGENEOUS POST-EROSION PARTICLE SIZE DISTRIBUTION

A new sample formation procedure is detailed here which involves the relocation of fines during erosion in an initially heterogeneous sample. It arrives at a homogenous particle size distribution throughout the sample. While it is desirable to have a homogeneous sample at all times in the erosion process involves varying hydraulic gradients and rates of particle movements making it practically unachievable.

Consider the sample described in Section 3.5, with an initially homogenous particle size distribution, and the three-stage erosion process. Also consider the post-erosion particle size distribution curves in each quarter of the sample as shown in Figure 3-18. This sample is referred to as GG15HET, where the prefix ‘GG’ indicates gap-graded and the suffix ‘HET’ indicates the sample has a heterogeneous post-erosion particle size distribution. The suffix ‘HOM’, used later, indicates a homogeneous post-erosion particle size distribution. The erosion mass loss of fine particles in each quarter was assessed using the curve matching technique proposed by Kenney and Lau (1985) and is assumed to be representative of the midpoint of the quarter. The erosion mass loss varies along the sample length and may be fitted (approximately) by a linear relationship (Figure 3-19). The symbols in Figure 3-19 represent the experimental measurements and the dashed line represents the linear fit. The average erosion mass loss along the entire sample length is represented by the point where a horizontal line at 200 mm (with distances measured downwards from the top of the sample) intercepts the linear fit, which is 7.22%. The erosion mass losses at 50, 150, 250 and 350 mm can similarly be determined using intercepts with the linear fit. It can be seen that the fines losses at 50 mm and 150 mm were 5.8%

and 2% greater than the average. At 250 mm and 350 mm the fines losses were 5.8% and 2% less than the average.

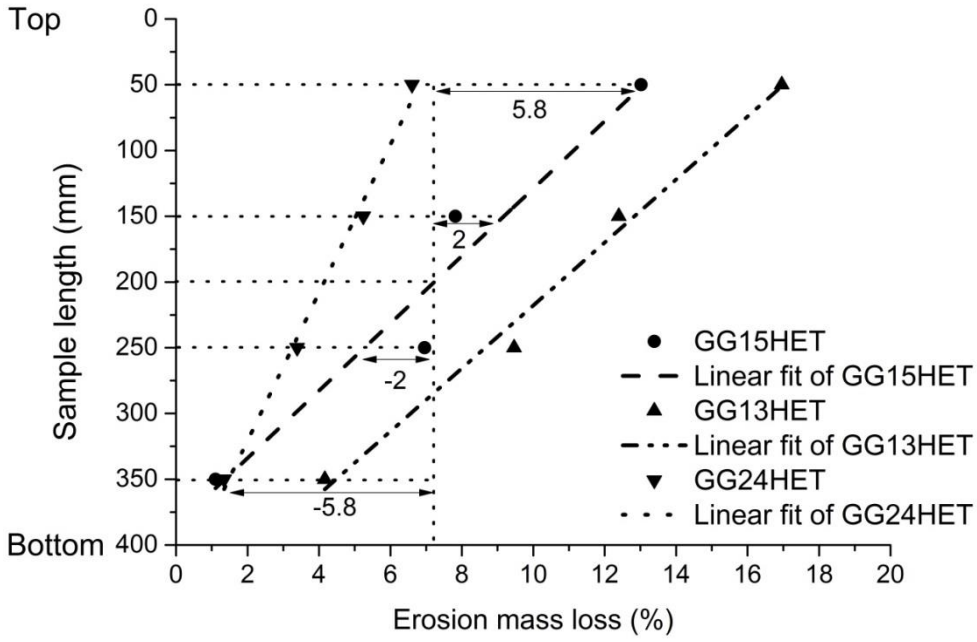

Figure 3-19 Erosion mass losses along the sample length.

The new sample formation procedure involves adjusting the fines concentrations in each sample layer during sample formation and prior to erosion to counteract these changes, keeping the global density of the sample uniform. Based on the GG15HET sample response, the fines concentrations in the 1st (top), 2nd, 3rd and 4th quarters are set to be about 5.8% greater, 2% greater, 2% less than and 5.8% less than for the initial condition (Figure 3-19), respectively. To achieve this, the fines concentrations in a six-layered sample need to be obtained from the linear fitting in Figure 3-19. For sample compacted by six compaction layers, the amount of fines adjustment for each layer is the horizontal difference between erosion mass loss of the midpoint of each layer and erosion mass loss at 200 mm from the linear fitting in Figure 3-19, assuming the loss in each layer could be represented by the loss at the midpoint of each layer. Thus, from top to bottom layer, namely at 33.3, 99.9, 166.5, 233.1, 299.7, 366.3 mm, the fines adjustment

for each layer is 6.4%, 3.9% ,1.3%, -1.3%, -3.9% and -6.4%. So after adjustment, the percentage by weight of fine particles of each layer is 27.2%, 28.8%, 30.4%, 31.7%, 33.1% and 34.7% from the top to bottom. A few trail compaction tests were done on single layers with those adjusted fines contents and showed that the effects of the fines adjustments on the relationship between compacting durations and dry density were neglected. Since the total mass of each quarter is different the target compaction durations of each quarter were scaled to ensure the soil absorbs the same amount of compacting energy. From the top layer to the bottom layer the target compaction durations for each layer were 15.4, 15.1, 14.7, 14.3, 13.9 and 13.6 s. After applying the undercompaction method (Vo and Russell (2013)), the duration series becomes 20.5, 14.7, 14.3, 14.3, 13.8 and 9.4 s. The coarse particles act as the soil skeleton and do not relocate during internal erosion. The content of coarse particles (by mass) in each layer is the same and does not change. When subjected to the same erosion sequence a more homogenous particle size distribution results.

The erosion mass loss and its linear fit may depend on the seepage pattern. For sample GG13HET the erosion process involved passing 8×10^{-3} m^3 of water upwards, then downwards, then a further two up-down cycles (so a total of 48×10^{-3} m^3 passed through). For sample GG24HET the erosion process involved passing 8×10^{-3} m^3 of water upwards only. Clearly, GG13HET exhibited a greater erosion mass loss than GG15HET, which in turn exhibited a greater erosion mass loss than GG24HET, as can be seen in Figure -19.

According to Skempton and Brogan (1994) the fine and coarse fraction division point S_f could be read off the particle size distribution curve. It should be less than 35% if the coarse particles are not “floating” in a matrix of fines; and there is a critical content of fine particles S^*, below which the fine particles in a gap-graded soil matrix do not fill up the voids in coarse component.

In summary, the steps to be followed in the new sample formation procedure are:

1. Prepare a homogenous sample of known particle size distribution by moist tamping six layers so each layer in the completed sample has at the same thickness and density.
2. Subject the sample to the desired erosion sequence.
3. After erosion split the sample into a number of layers of equal thickness along its length (at least four) and determine the post-erosion particle size distributions in each layer.
4. Plot the erosion mass loss of each layer against the sample length (to the midpoint of each layer) and fit the data using a linear relationship.
5. Prior to forming another sample by moist tamping (six layers were used here but could be any number greater than four) determine the fines concentrations required in each layer so that the erosion (the same as that used in Step 2) will result in homogeneity of the particle size distribution. To do this assume that the erosion will remove fine particles at locations along the sample length (taken as the midpoints of each of the tamped layers) according to the linear relationship determined in Step 4. Adjust the compaction energy applied to each layer in Step 1 to reflect the increased or decreased mass of soil in each layer, ensuring each layer in the formed sample has the same dry density.
6. Subject the sample to the same erosion sequence as in Step 2.
7. After erosion and subsequent triaxial testing split the sample into a number of layers of equal thickness along its length (at least four) and confirm that the particle size distributions in each layer are the same.

3.7 A DEMONSTRATION OF THE EFFECTIVENESS OF THE NEW FORMATION PROCEDURE

Using the new procedure three new samples were prepared, denoted GG23HOM, GG32HOM, and GG27HOM, designed to counteract the erosion induced heterogeneities of particle size distributions observed for samples GG15HET, GG13HET and GG24HET, respectively.

To aid the saturation of samples, they were first flooded with carbon dioxide (CO_2) gas. The pressure of CO_2 at the base inlet was about 15 kPa while a hydrostatic pressure of 20 kPa was applied to external boundaries. The introduction of carbon dioxide was allowed to occur 30 minutes, appropriate to replace most of the air in the voids of the samples. Water was then passed through the soil samples, entering the base. The water inflow was driven by a constant water head, which provided an average hydraulic gradient of 0.05. The water inflow rate was sufficiently slow to minimize the filtration of fine particles in the samples (inevitably, a very small portion of fines near the top surface of the sample were transported out of sample). The inlet and outlet valves were then closed and the pore pressure was slowly increased to 10 kPa. A number of control samples were prepared for conventional triaxial compression testing without any internal erosion, and for these the application of back pressure began after the introduction of water. The pore pressure and cell pressure were increased incrementally and slowly. The magnitude of each increment was 20 kPa. During this stage, the difference between cell pressure and pore pressure was held constant at 10 kPa. A number of samples were prepared for internal erosion and subsequent triaxial testing, and for these at an effective stress of 20 kPa was applied during the saturation process with a 5 kPa constant back pressure. Prior to consolidation, erosion, and subsequent triaxial testing, the B-value was determined to confirm that the samples were well saturated.

Consolidation involved by gradually increasing the cell pressure to the desired value, slowly (2 kPa per minute) to avoid potential soil particle migration. During consolidation the pore volume was recorded every minute. All the samples were isotropically consolidated until the preferred effective stresses were reached. After consolidation the soil samples were ready for erosion tests and subsequent triaxial compression tests.

The three samples GG23HOM, GG32HOM and GG27HOM, were subjected to the same water seepage sequences that GG15HET, GG13HET, and GG24HET were subjected to. The durations required for the collected effluent to reach target volumes are recorded. During the internal erosion tests, the stress states of the soil samples were maintained at the same levels as what

prevailed after consolidation. The seepage directions were reversed after every 8×10^{-3} m^3 of water passes through the samples, causing the effective stress gradients to be reversed also.

The constant water head and hydraulic gradient should be sufficiently high to cause suffusion within a sample. However, they should not be so high that they cause large effective stress differences throughout the sample. As mentioned in Section 3.3.3, the seepage, induced by a constant water head of 1.24 m (or 3.2 m in some of the tests in Chapter 4) at the bottom of soil sample applies a 12.1 kPa water pressure to the bottom of the soil sample. The outlet at the top of the soil sample is open to the atmosphere thus the water pressure is 0 kPa. When the seepage direction reversed, an 8.2 kPa water pressure is applied to the top of the soil sample and 0 kPa is applied to the bottom. Compared to the consolidation pressure being applied, the water pressure differences inside a sample are minor.

Once the seepage sequence was completed the confining pressure was raised to 260 kPa and the pore pressure was raised to 210 kPa, imposing a uniform and isotropic effective stress of 50 kPa on each sample. A drained triaxial compression test was then conducted.

The drained triaxial compression tests were conducted at a strain rate of 0.2 mm/min on seven samples, six having been subjected to different amounts of internal erosion (three for the conventional and three for the new sample formation procedures) plus one which had not been subjected to internal erosion and was prepared to have an initial homogeneous particle size distribution. This strain rate is sufficiently slow for drained conditions to prevail. The confining and pore pressures are maintained constant at 260 kPa and 210 kPa, respectively. The axial displacement, axial load, pore water volume, and cell volume are recorded at regular intervals during the tests. After each test the post-erosion particle size distribution in each quarter of a sample was determined by wet sieving.

3.7.1 Flow rates during erosion

The flow rate was used here as an indicator of the progress of internal erosion. Richards and Reddy (2009) suggest that hydraulic velocity is a better indicator than the flow rate to monitor the progress in cohesionless soils. However, since the true cross-sectional area of seepage flow in a sample was not measured here it was not possible to determine the hydraulic velocity in a reliable way.

The development of flow rate with time for samples prepared by the two methods are shown in Figure 3-20. For samples subjected to internal erosion for long periods, the flow rate generally increased with time until a certain time was reached, beyond which it became stable. An increasing flow rate suggests that fine particles are being removed creating additional void space. At a certain time, once a large number of fine particles had been removed, stable flow channels had formed within the sample and a stable flow rate was observed. The variation of flow rate for both sample formation procedures shows that there is no major influence of the relocation of fine particles on the flow rate.

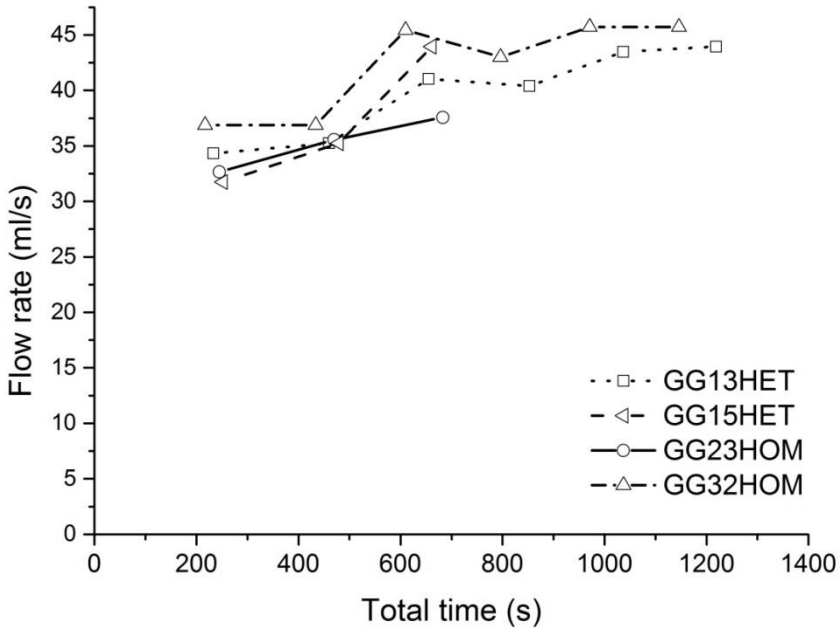

Figure 3-20 Flow rate with time.

3.7.2 Post-erosion particle size distributions and densities

After erosion and subsequent triaxial testing, each sample was quartered into layers of equal thickness. The particle size distribution of each layer was determined by wet sieving. The particle size distributions for sample GG23HOM are shown in Figure 3-21. Each particle size distribution curve moved downwards from the initial position (of the control test sample) by about the same amount. Figure 3-22 shows the percentage of erosion mass loss along the sample length for GG23HOM (relative to the control sample) and GG15HET. The erosion mass loss is far more uniform along the sample's length for the new preparation method compared to the conventional method. These observations indicate that a (nearly) homogeneous particle size distribution results from the new preparation method.

The samples GG13HET and GG32HOM had a total of 48×10^{-3} m^3 of water passed through them through six upward-downward seepage cycles. Samples GG24HET and GG27HOM had 8×10^{-3} m^3 of water passed through them in one upward cycle.

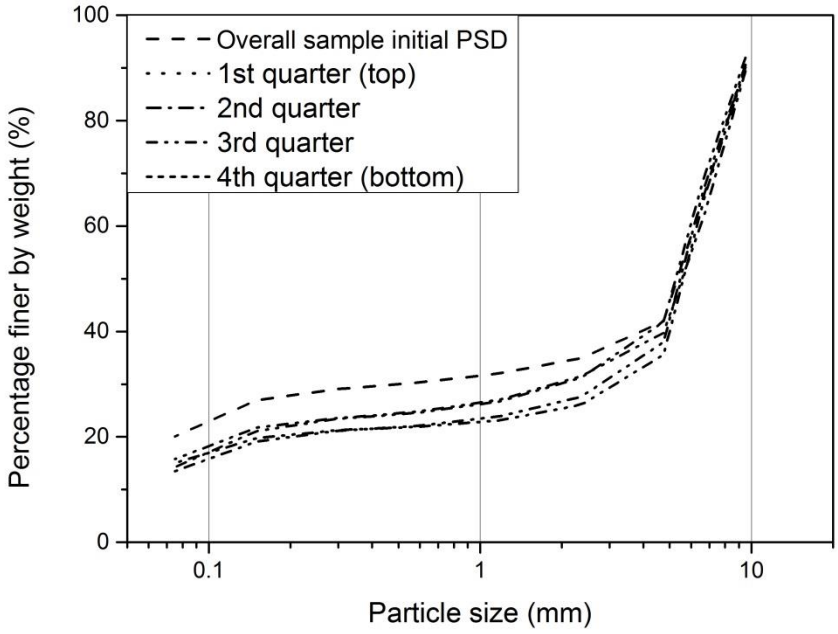

Figure 3-21 The post-erosion particle size distributions for sample GG23HOM formed using the new procedure.

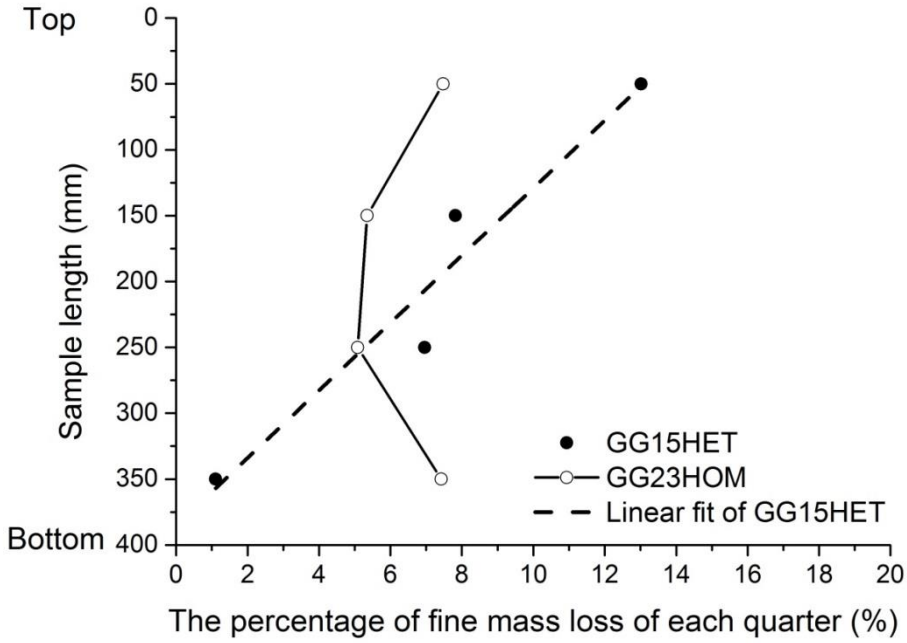

Figure 3-22 Percentage of erosion mass losses along the sample length for samples formed using the conventional (solid symbols, GG15HET) and new procedures (hollow symbols, GG23HOM).

The axial displacement was measured by reading the mark of a laser pointer. However, no axial displacement was observed for the samples. Thus the density of each quarter of the eroded sample can be calculated once the fine mass loss of each quarter is known. The densities of each quarter of the samples are given in Table 3-3. According to Table 3-4, for sample compacted by method described in section 2.6, the top quarter has the minimum post-erosion density and the bottom has the maximum post-erosion density, while the middle two quarters have approximately the same density. This is consistent with the trend of post-erosion particle size distributions observed by Kenney and Lau (1985). It is noticeable that the variations in post-erosion densities are reduced by using the proposed sample formation method.

Table 3-3 Post-erosion densities of each quarter for samples with and without erosion

	The quarter from top to bottom	Post-erosion density (g/cm^3)
Sample without erosion	1 (top)	1.83
	2	1.94
	3	1.96
	4 (bottom)	2.07
Sample with erosion	1 (top)	1.93
	2	1.97
	3	2.01
	4 (bottom)	1.99

The samples GG13HET and GG32HOM had a total of 48×10^{-3} m^3 of water passed through them through 3 upward-downward seepage cycles. Samples GG24HET and GG27HOM had 8×10^{-3} m^3 of water passed through them in one upward cycle. The post-erosion particle size distributions are shown in Figures 3-23, 3-24, 3-26 and 3-27 and the erosion mass losses along the sample lengths are shown in Figures 3-25 and 3-28. Again, for the new preparation procedure, the particle size distribution curve for each sample quarter moved downwards from the initial position by about the same amount. The percentage of erosion mass loss is also more uniform along the sample's length for the new preparation method compared to the conventional method. These observations further indicate the ability of the new preparation method to create (near) homogenous particle size distributions.

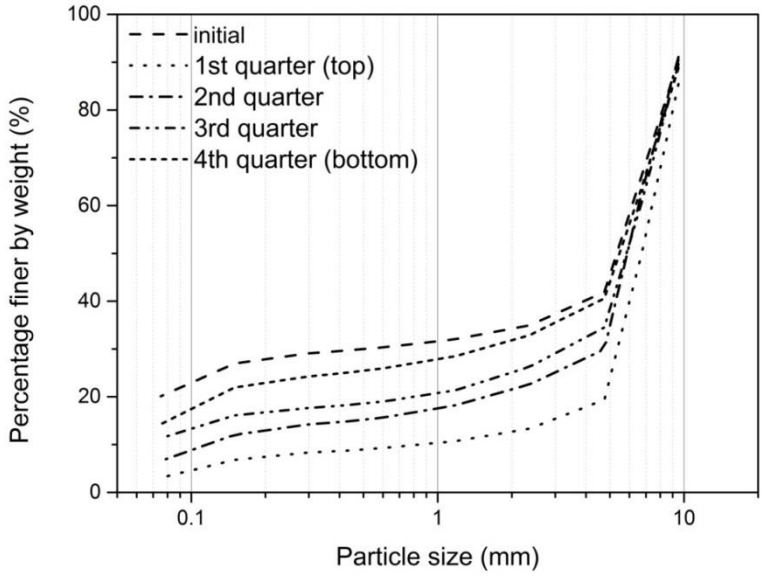

Figure 3-23 Post erosion particle size distribution of soil sample GG13HET formed using the conventional procedure.

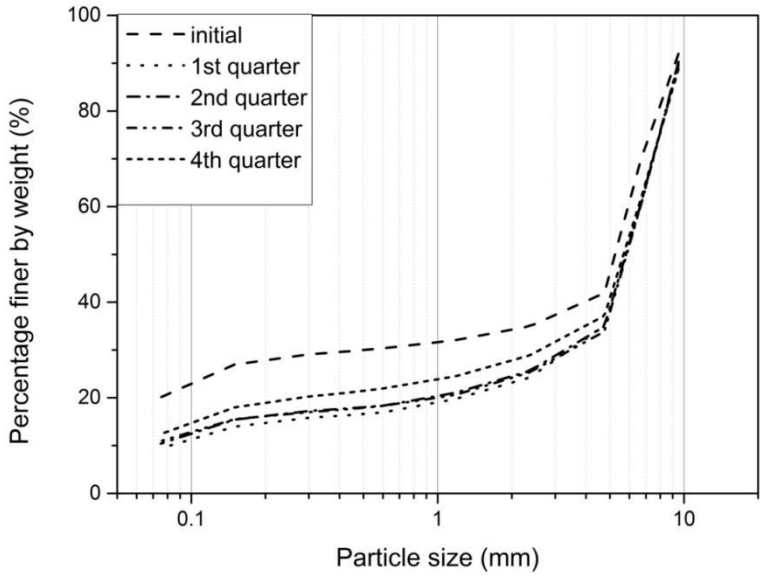

Figure 3-24 Post-erosion particle size distributions for sample GG32HOM formed using the new procedure.

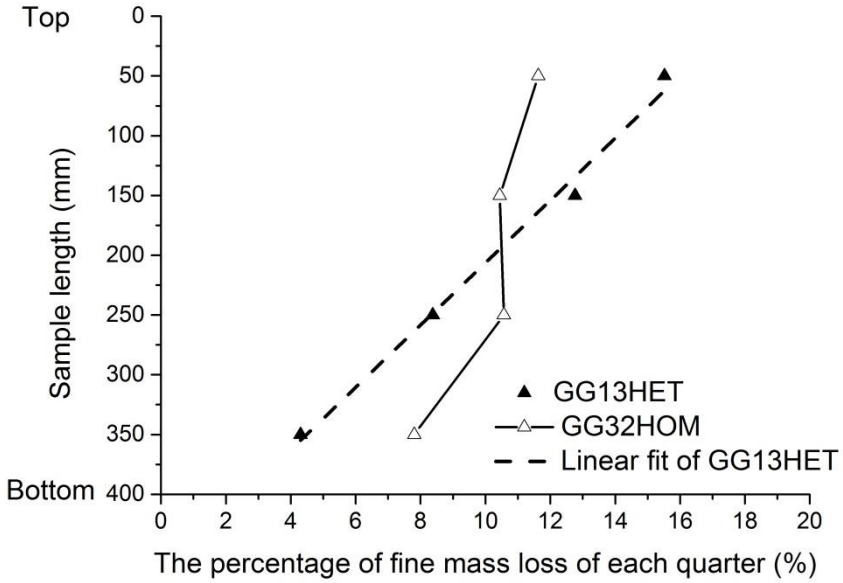

Figure 3-25 Percentage of erosion mass losses along the sample length for samples formed using the conventional (solid symbols, GG13HET) and new procedures (hollow symbols, GG32HOM).

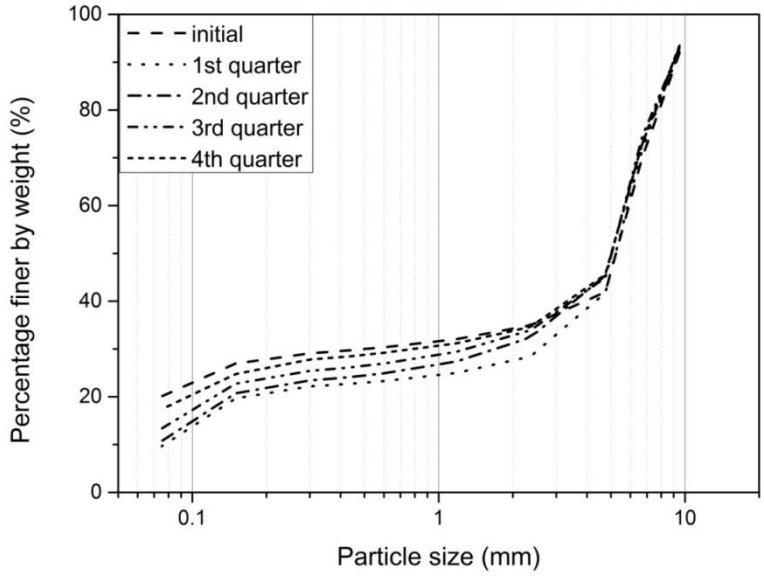

Figure 3-26 Post erosion particle size distribution of soil sample GG24HET formed using the conventional procedure.

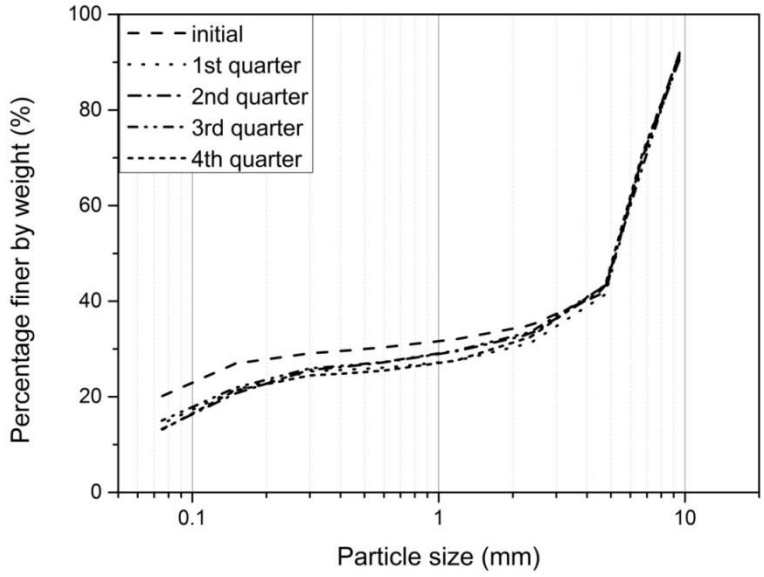

Figure 3-27 Post-erosion particle size distributions for sample GG27HOM formed using the new procedure.

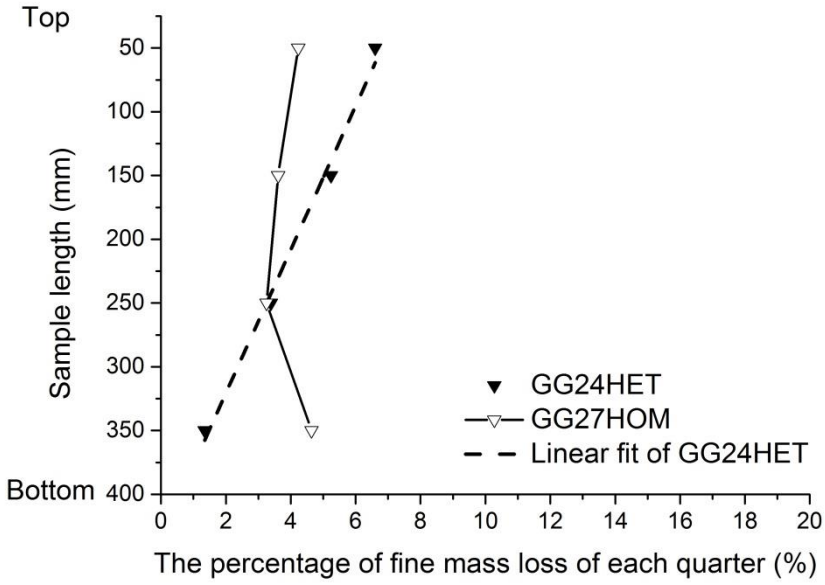

Figure 3-28 Percentage of erosion mass losses along the sample length for samples formed using the conventional (solid symbols, GG24HET) and new procedures (hollow symbols, GG27HOM).

3.7.3 Evolution of eroded mass

A few researchers (Bendahmane et al., 2008; Ke and Takahashi, 2014b; Ouyang and Takahashi, 2015) have recorded the evolution of cumulative eroded soil mass. Typically, the cumulative eroded soil mass increases dramatically in the early stages of seepage before increasing gradually and eventually approaching a constant, as shown in Figure 3-29. The increased mass loss is less than 1‰ by mass in 180 seconds and sample GG03HET was subjected to seepage cycles until the effluent became clear, which indicated the end of internal erosion (Ke and Takahashi, 2014). The point where the cumulative eroded mass shows no further increase indicates the end of internal erosion. The initiation of the particle removal can be identified by the effluent becoming turbid. The cumulative eroded soil mass for GG13HET and GG32HOM, expressed as a percentage of the total initial soil mass, is plotted against the logarithmic of time in 3-30, along with data from other researchers. Straight lines fit the data well. The lines which fit GG13HET and GG32HOM show general agreement in the evolutions of the cumulative eroded masses, indicating there is only a small, if any, influence of the relocated fine particles on particle removal induced by seepage. For the triaxial erosion tests on gap-graded soils at initially isotropic stress states, despite the hydraulic conditions varies, the time at which erosion initiates may be approximated by extrapolating the linear fit down to the zero cumulative eroded soil mass axis. For example, the onset of internal erosion for the erosion test of Ke and Takahashi (2014b) is about 500 s after the sample had been subject to the hydraulic gradient.

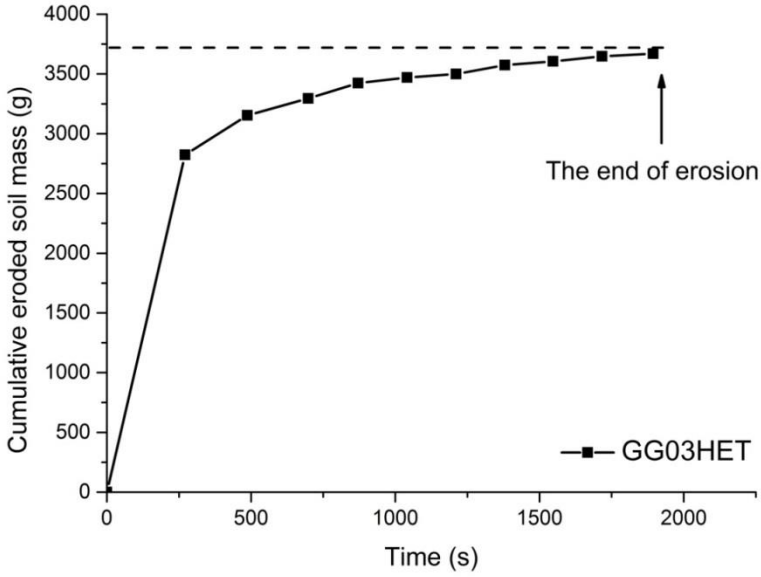

Figure 3-29 Typical evolution of eroded soil mass.

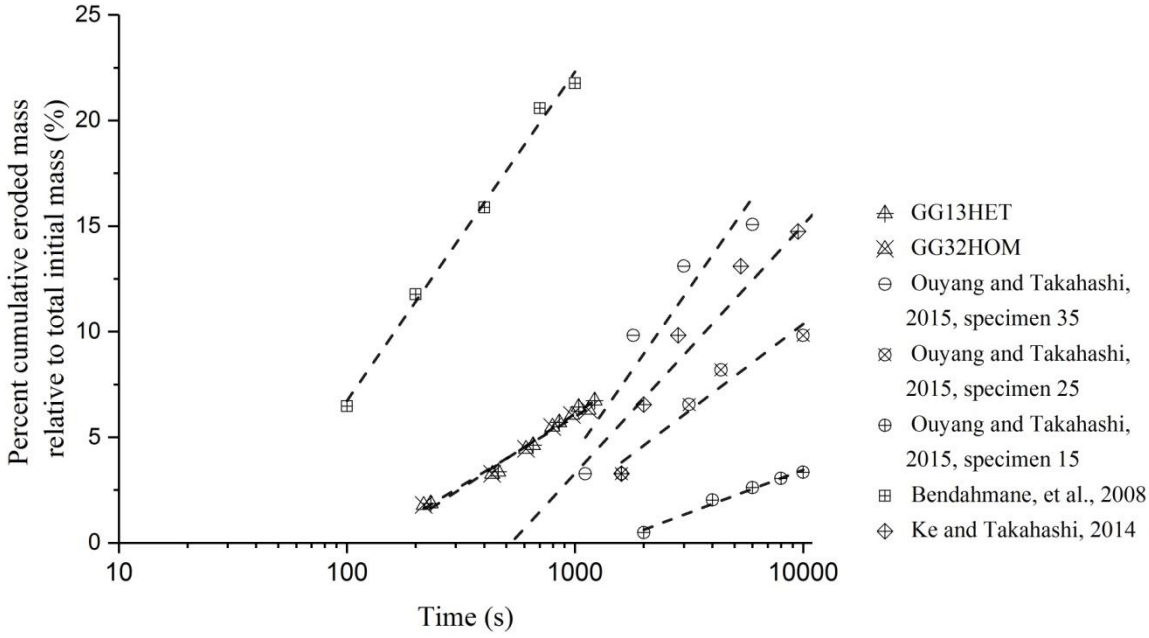

Figure 3-30 Percent of cumulative eroded soil mass relative to total initial mass.

3.7.4 Drained triaxial compression test results for samples formed using the conventional and new procedure

The tests have been conducted on eroded samples prepared by the conventional and new procedures immediately after the erosion processes ended. The properties of the samples are noted in Table 3-4.

The test on sample GG14 is a conventional drained triaxial test with results that benchmark the mechanical behavior of the soil without internal erosion. Samples GG24HET, GG27HOM, and GG29HOM were subjected to 8×10^{-3} m^3 of upward seepage prior to the triaxial test being conducted. These samples were prepared, eroded and tested under identical conditions and the good agreement of the results confirms the repeatability of the procedures followed. Samples GG15HET and GG23HOM were subjected to 24×10^{-3} m^3 of seepage, with the seepage direction alternating at 8×10^{-3} m^3 intervals. GG13HET and GG32HOM were subjected to 48×10^{-3} m^3 of seepage, with the seepage direction alternating at 8×10^{-3} m^3 intervals. The different amounts of seepage caused different amounts of fine particle removal, as shown in Table 3-5 and the figures that follow.

Photographs of the failed samples GG24HET and GG27HOM are shown in Figure 3-31. The shear plane of GG24HET was located entirely in the upper three quarters of the sample where the fine particle losses were greatest. The deformation of the sample was much smaller in the bottom zone than the upper three quarters. Compared to the upper three quarters, the bottom zone (within the dashed line at the bottom of the sample GG24HET) was relatively intact, while this was not the case in sample GG27HOM. The shear plane of GG27HOM was located in the middle of the sample, as is the norm for a sample with a homogenous void ratio and particle size distribution prior to the test commencing.

Figure 3-32 plots the stress-strain curves together with the volumetric strain curves for the first set of tests GG14, GG24HET, GG27HOM and GG29HOM. Figure 3-33 shows plot of the stress-strain curves together with the volumetric strain curves for the second set of tests GG15HET, GG23HOM and GG14. Figure 3-34 shows plot of the stress-strain curves and the volumetric strain curves for the third set of tests GG13HET, GG32HOM and GG14.

All the above samples exhibited a strain hardening response initially which was followed by strain softening. The samples were generally dilative when sheared. The peak strength of an eroded sample with a homogeneous particle size distribution was slightly higher than that of a sample which had a heterogeneous particle size distribution, as can be seen in Figures 3-32(a), 3-33(a) and 3-34(a). The constant volume (large-strain) shear strengths exhibited a similar trend. At large strains, where the initial (post-erosion) sample density was not expected to affect the strength, the increased coarseness of particle size distribution following erosion caused a strength increase. This trend is consistent with findings by Chang et al. (2014).

The peak strengths for all samples which had eroded were less than that of the sample which had not eroded. The removal of fine particles from a gap-graded soil reduced the strength, in agreement with Muir Wood et al. (2010), Scholtès et al. (2010), Ke and Takahashi (2014b) and Chang et al. (2014). For samples (GG27HOM, GG23HOM, GG32HOM) with homogeneous post-erosion particle size distributions, but increasing amounts of fine particles lost by erosion, the peak strength decreased as the fine particle losses increased. It can be seen from Table 3-5, the percentages of fines mass loss of GG14, GG27HOM, GG23HOM, GG32HOM were 0, 3.9%, 6.32%, and 10.08%, respectively, the peak strength of each sample were 386, 358, 328 and 309 kPa. Although samples GG24HET, GG15HET and GG13HET showed a similar trend in that as the loss of fines increased, the peak strength decreased, they each had heterogeneous post-erosion particle size distributions. From the point of view of critical state soil mechanics, for soil samples under isotropic stress states, as fine particles were removed by internal erosion the void ratio increased gradually and the critical state line moved upwards gradually as well. According to Muir Wood et al. (2010), the increase in the void ratio caused by erosion would be greater

than the upward shift of the critical state line, thus resulting in an increasing state parameter as internal erosion continues. The increasing state parameter would further result in a decreasing peak strength (Gajo and Muir Wood 1999; Muir Wood 2004), causing the peak strength decreases as the fine particle losses increases in these tests. This will be explained in more detail here in Chapter 5.

At small shear strains the samples with heterogeneous post-erosion particle size distributions exhibited a greater amount of contraction compared with samples with homogeneous post-erosion particle size distributions, as shown in Figures 3-32(b), 3-33(b) and 3-34(b). However, there were some variations in the change of volume at large shear strains. In Figure 3-32(b) GG15HET, that is the sample with a heterogeneous post-erosion particle size distribution, exhibited less dilation at large shear strain, while in Figures 3-32 (b) and 3-34(b) the samples GG23HOM and GG32HOM with homogeneous post-erosion particle size distributions exhibit the least dilation. These contrasting results might be because of the different amounts of fine particle loss, even though the same erosion conditions were applied these tests. Further data is needed to explore and confirm this aspect of behavior and understand its causes.

Tests on samples GG27HOM and GG29HOM were conducted to further confirm repeatability, in which 3.9% and 4.2% of fines were removed by erosion. Figure 3-33(a) and (b) show the stress-strain curves and volumetric changes. The stress-strain curves for these two samples exhibit good repeatability, although some minor differences of large strain strengths are evident.

The peak strengths, and friction angles at peak and large strains, are listed in Table 3-5 along with the percentages of fines lost by erosion. The cohesion is assumed zero when determining the friction angles.

Table 3-4 Summary of triaxial compression test conditions and results.

Sample	Seepage passing through (10^{-3} m^3)	Percentage of fine particle mass loss (%)	Peak strength (kPa)	Friction angle at peak (°)	Friction angle at large strain (°)	Sample preparation method	Post-erosion particle size distribution
GG14	0	0	386	52.6	43.8	Conventional	--
GG24HET	8	4.1	330	50.1	43	Conventional	heterogeneous
GG27HOM	8	3.9	358	51.4	43.3	New	homogeneous
GG29HOM	8	4.2	356	51.3	42.6	New	homogeneous
GG15HET	3×8	7.1	301	48.6	41.4	Conventional	heterogeneous
GG23HOM	3×8	6.32	328	50.0	42.6	New	homogeneous
GG13HET	6×8	10.2	294	48.3	41.5	Conventional	heterogeneous
GG32HOM	6×8	10.08	309	49.1	42	New	homogeneous

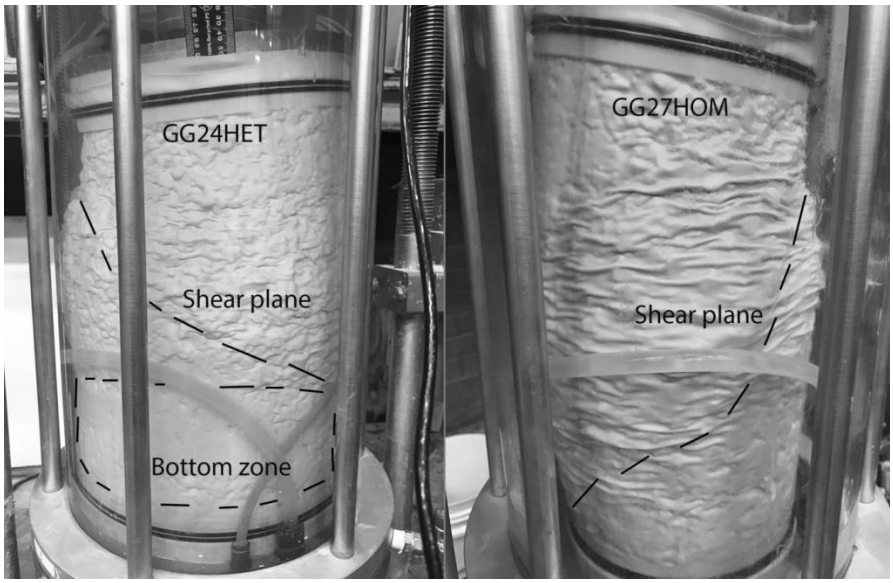

Figure 3-31 Failed samples of GG24HET and GG27HOM.

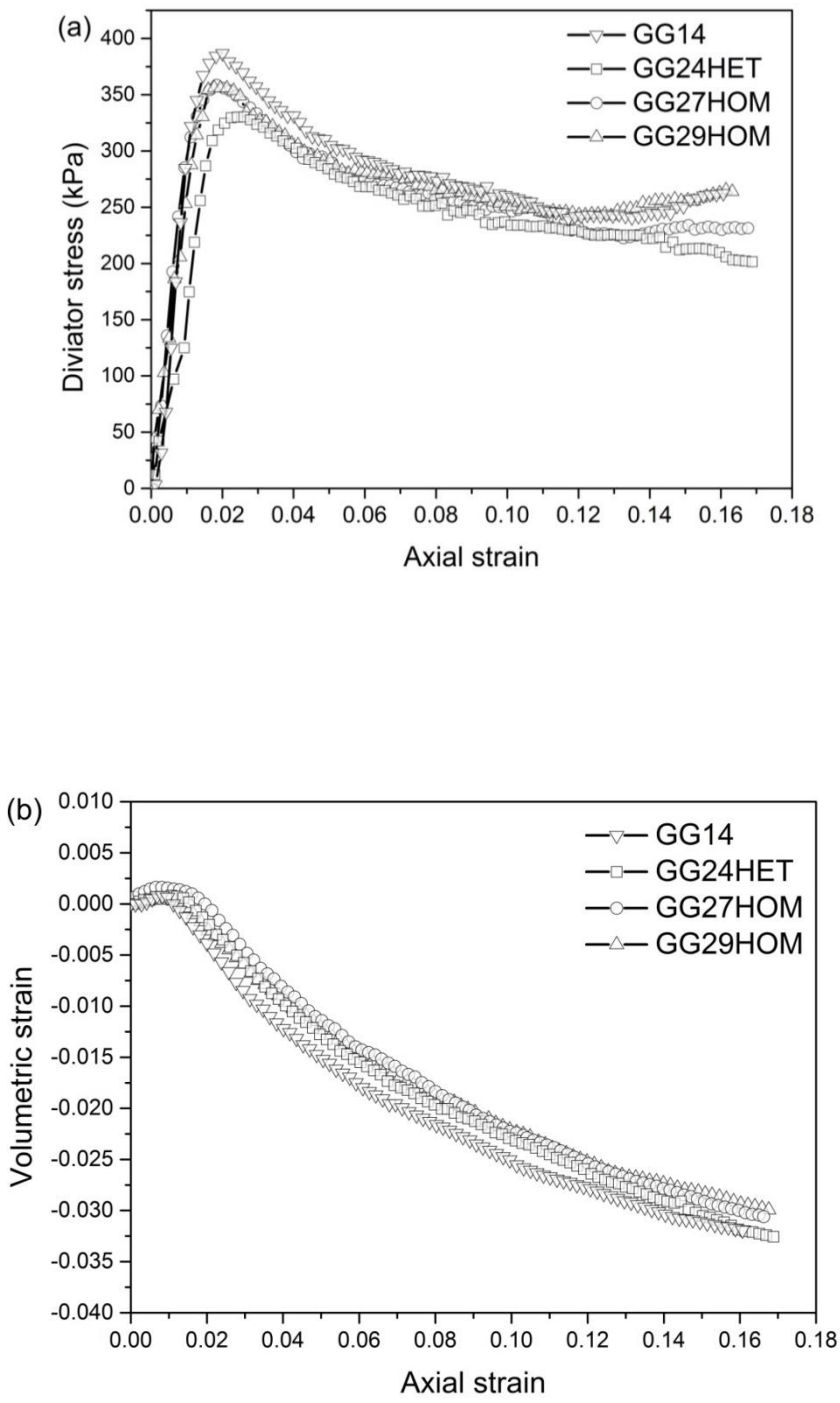

Figure 3-32 Drained compression tests on samples subjected to internal erosion. (a) Stress-strain relationships. (b) Volumetric strain and shear strain relationships.

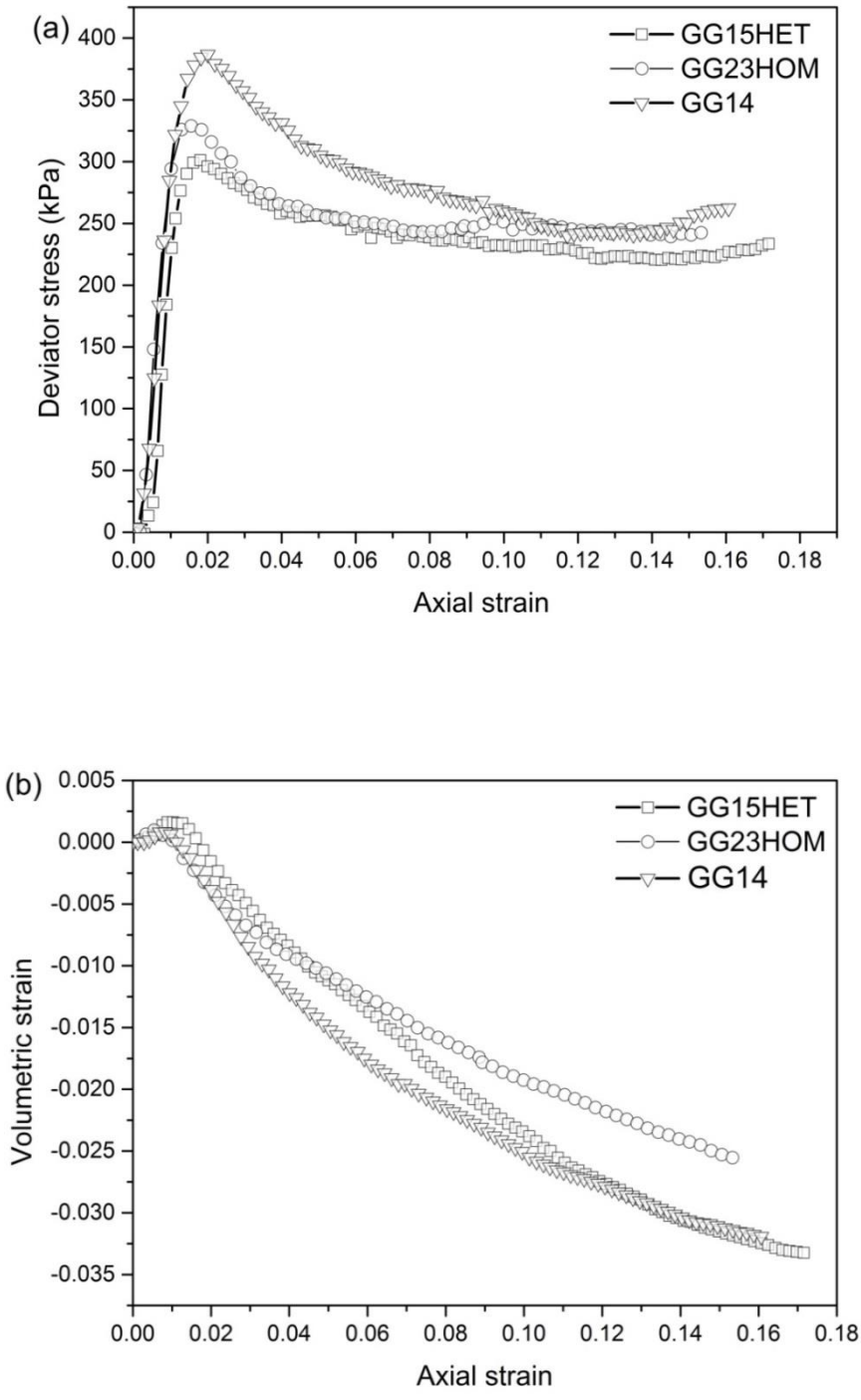

Figure 3-33 Drained compression tests on samples subjected to internal erosion. (a) Stress-strain relationships. (b) Volumetric strain and shear strain relationships.

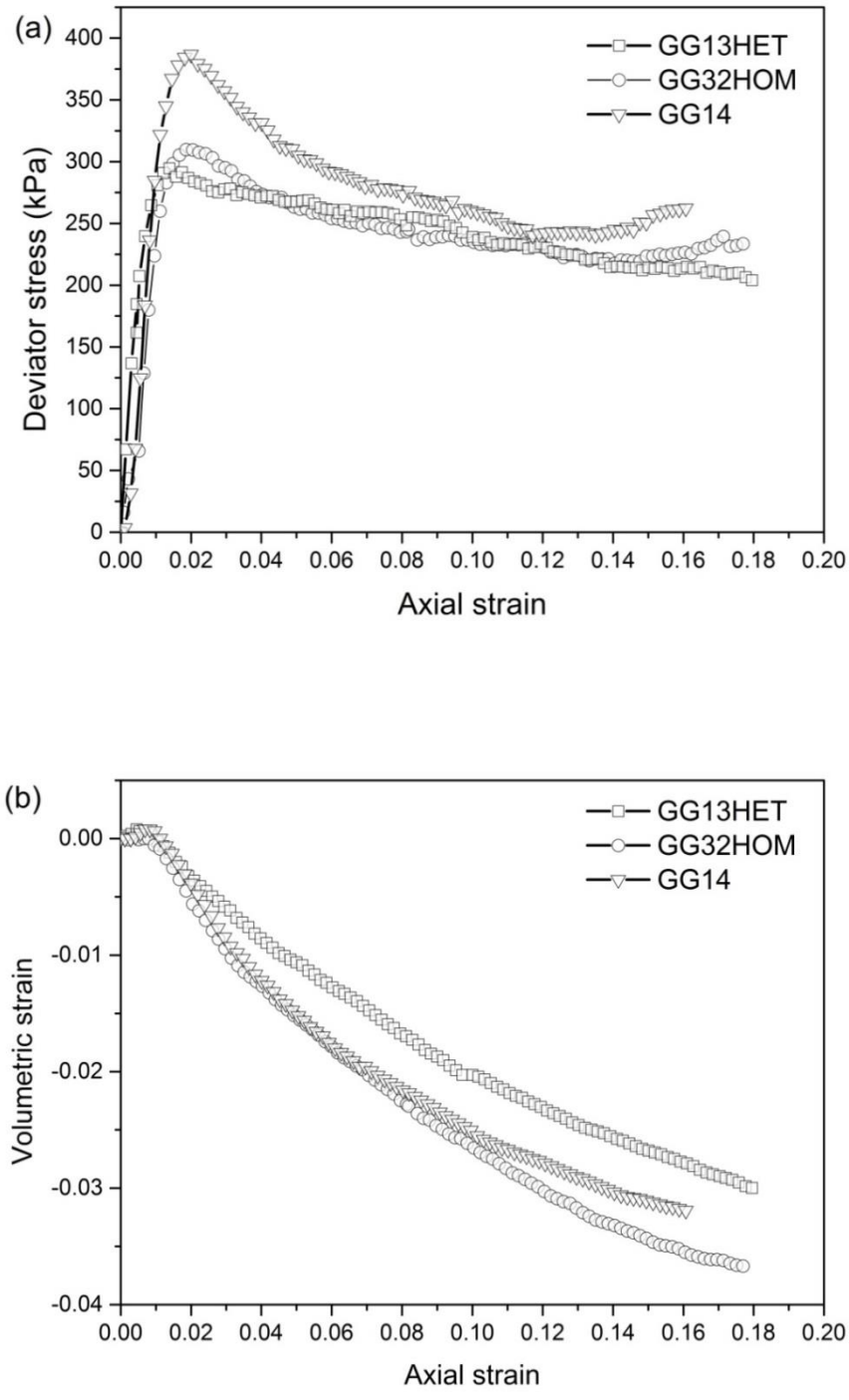

Figure 3-34 Drained compression tests on samples subjected to internal erosion. (a) Stress-strain relationships. (b) Volumetric strain and shear strain relationships.

3.8 DISCUSSION AND CONCLUSION

A triaxial erosion apparatus which enables seepage to pass through soil sample, upwards or downwards, to cause internal erosion under varying confining pressures and then sheared has been introduced. A new sample preparation method was detailed which accounts for and corrects for the different amounts of erosion mass loss which occur along the length of a sample. It produces a more homogeneous particle size distribution throughout a sample post-erosion when compared to that from a conventional sample preparation procedure. It involves the reallocation of fine particles in each compacted layer of a heterogeneous sample so that the subsequent erosion produces a homogenous particle size distribution throughout the sample. It is a reasonable and practical compromise for producing samples for triaxial testing, enabling the observed mechanical behaviors to be linked to measures of the initial state including the particle size distribution, void ratio and state parameter.

Drained triaxial compression test results for samples with homogenous and heterogeneous post-erosion particle size distributions were compared. For two samples which had the same amount of fines removed by erosion, the one with a homogeneous particle size distribution exhibited the greater peak strength.

This new sample formation method, however, aims to produce homogeneous post-erosion particle size distribution for the study of mechanical consequences of internal erosion on soils. The amounts of fine particle relocation in compaction layers are determined from a conventional triaxial erosion test on soils with a certain amount of erosion. It results in a sample with

heterogeneous particle size distribution before internal erosion. Thus, this sample formation method is designed for experimental purposes.

For samples with homogeneous post-erosion particle size distributions, but different amounts of fines lost by erosion, the peak strength decreased as the amounts of fines lost increased. This may be linked to an increasing state parameter, although more data which combines changes of void ratio, particle size distribution and the critical state line is needed to confirm this hypothesis. This will be explored in Chapter 5 and 6. The strength change indicates that a prompt remedy is of great importance for earth dams showing an early sign of internal erosion.

CHAPTER 4 ADDITIONAL TRIAXIAL EROSION TESTS

4.1 INTRODUCTION

4.1.1 Overview

This chapter presents additional results of the experimental investigation of a gap-graded cohesionless soil subjected to different amounts of internal erosion (suffusion) under different effective stress states. The main objectives of the laboratory investigation were to:

- investigate erosion characteristics of the test soil with different relative densities under different hydraulic conditions and stress states, namely, to monitor flow rate, cumulative eroded mass, axial strain and volume strain during erosion.
- study the stress-strain behavior of the test soil having been subjected to different amounts of internal erosion under different effective stresses.

This chapter mainly focuses on the findings of the experimental investigation. Testing apparatus, sample formation procedure and testing procedures were detailed in Chapter 3. The findings in this Chapter and those of Chapter 3 will provide experimental data and evidence so that the fractal characteristics of the soil can be detailed in Chapter 5 and a constitutive model for soil when subjected to internal erosion can be developed in Chapter 6.

4.1.2 Needs for research on gap-graded cohesionless soils subjected to different amounts of internal erosion under different effective stress states

The recognition that the grading of soils in water retaining structures (embankment dams, levees, and dikes) may change with time in some circumstances during their service life due to internal

erosion is obviously crucial for understanding and modelling the behavior of soils having undergone internal erosion. The soils forming the containment structures may exhibit varying particle size distributions at different stages due to the time-dependency of the loss of fine particles caused by internal erosion. The changing grading (i.e., the changing particle size distribution) certainly has significant influences on critical state parameters (Luzzani and Coop 2002; Muir Wood and Maeda 2008), for example, which control the stress-strain behavior of the soil. Therefore, it is important to study the soil's response to different amounts of internal erosion for dam engineers and owners to predict the likely hydraulic and mechanical consequences at different stages of internal erosion.

As discussed in Section 3.5.2 the gap-graded cohesionless soil used in this study is susceptible to internal erosion. Different amounts of erosion, which progressively changes the soil's grading while maintaining a constant confining stress, are caused by passing water through compacted samples inside a triaxial apparatus in an upward and/or downward direction.

Different volumes of seepage, driven at a certain constant hydraulic gradient, were introduced into the test soil samples to cause different amounts of fine particle losses. The method of introducing different volumes of seepage water to cause different amounts of internal erosion is able to provide adequate control over the varying hydraulic conditions and stress states, which are expected to influence the test soil's behavior during erosion as well as subsequent drained monotonic compression.

4.2 CHARACTERISTICS OF THE TEST SOIL WHEN SUBJECTED TO DIFFERENT AMOUNTS OF INTERNAL EROSION

4.2.1 Introduction

The triaxial erosion tests include two parts, namely a seepage test under a certain effective confining stress by passing water upwards or downwards through a sample with a constant water head and then a drained triaxial test under the same effective confining stress.

Recently, laboratory experiments helped researchers make advances in the understanding the influences of seepage-induced internal erosion on soils. Early laboratory investigations focused solely on the change in particle size distribution as a sign of internal instability (Burenkova 1993; Kenney and Lau 1985; Lubochkov 1965). Cumulative mass loss due to internal erosion is commonly used to quantify internal instability (Bendahmane et al. 2008; Moffat 2005; Skempton and Brogan 1994; Wan 2006). Lafleur et al. (1989) was one of the first to report an erosion induced changes in hydraulic conductivity, obtained by measuring the hydraulic gradient and flow rate. The hydraulic gradient and flow rate are commonly recorded as indicators of the onset and development of internal instability (Bendahmane et al. 2008; Moffat et al. 2011; Skempton and Brogan 1994; Wan and Fell 2004). The recognition of whether or not deformations occurs due to seepage, including axial strain, radial strain and volumetric strain, has not received as much attention. Some have used a flexible-wall permeameter and triaxial erosion apparatus to measure soil deformation (Bendahmane et al. 2008; Chang and Zhang 2011; Ke and Takahashi 2014b). Fannin and Slangen (2014) suggest that three things should always be measured including (1) mass loss (and particle size distribution), (2) deformation (axial strain, radial strain, and/or volume strain) and (3) hydraulic properties (hydraulic gradient, flow rate, discharge velocity and/or hydraulic velocity).

The erosion characteristics measured in this investigation include the flow rate of seepage with time, cumulative eroded mass with time or volume of seepage water with time, axial strain and volume strain during internal erosion, and post-erosion particle size distributions throughout the sample.

The triaxial erosion tests have been designed to simulate internal erosion (suffusion) within earth water retaining structures. In triaxial erosion tests, the volume of seepage that passes through soil samples to cause different amounts of internal erosion were varied. The specific seepage upward-downward seepage cycles used are given in Table 3-5. The consolidation stresses applied to soil samples were 50, 100, or 200 kPa. The hydraulic gradients applied were either 3.1 or 8.

4.2.2 Flow rate and permeability with time

As mentioned in Section 3.8.1, the flow rate may be used as an indicator of the progress of internal erosion. It is not practically possible to determine the hydraulic velocity in a reliable way. The flow rate is defined as the rate of discharge:

$$q = \frac{V}{t} \qquad (4\text{-}1)$$

where V is the discharge volume and t is time.

The discharge volume was collected at different stages. The amount of eroded soil particles in the discharge volume was also determined.

The average permeability is defined as:

$$k_{ave} = \frac{q}{iA} \qquad (4\text{-}2)$$

where A is the cross-sectional area of the test sample.

From Section 3.8.1, we know that the flow rate generally increases with time until a certain time is reached, after which the flow rate becomes stable. An increasing flow rate suggests that fine particles are actively being removed creating additional void space and flow channels in the soil sample.

A photograph in Figure 4-1 shows a soil which has been subjected to internal erosion. Flow channels (in red circles) are formed within the soil sample due to the passing of water and fine particles. It is also interesting to notice that some parts of fine particles exhibit signs that water passed through, as shown in blue squares in Figure 4-1, while other parts of fine particles do not have a flowing texture, as shown in the green square. The direction of flow channels aligns with the flow direction. The observed flow channels are 2 mm in diameter, which is smaller than the minimum particle size of 10 mm for the basalt, indicating that fines were transported by seepage through the voids around the coarse fraction, which also acts as the soil skeleton.

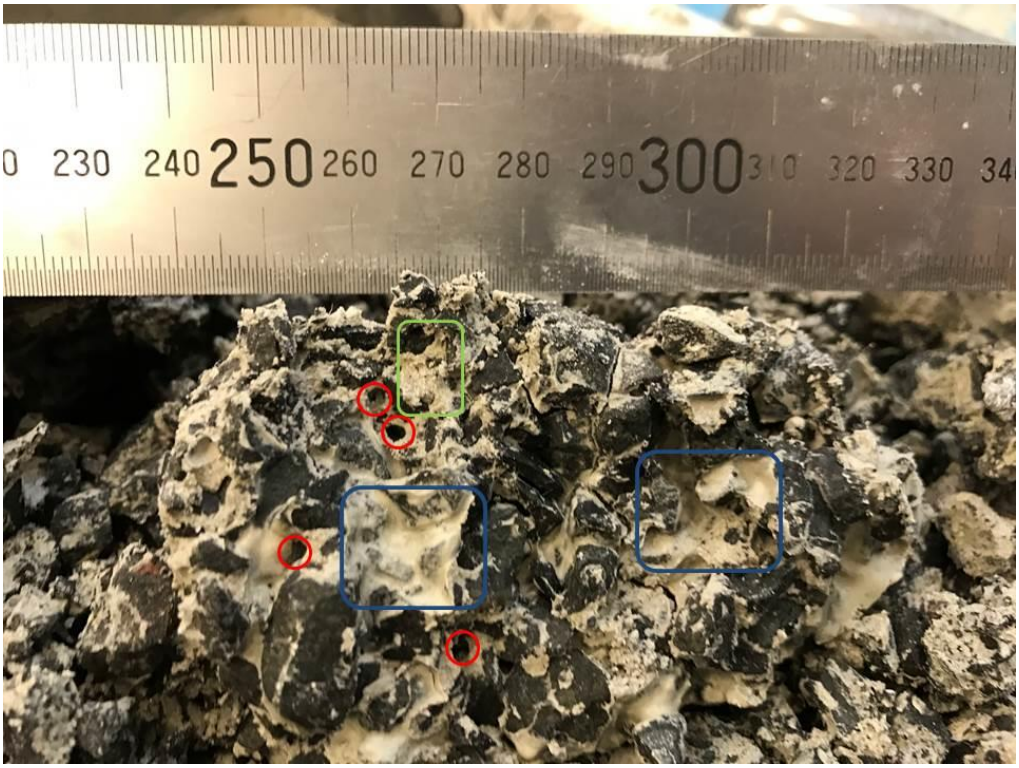

Figure 4-1 A photograph of soils subjected to internal erosion.

Once a certain number of flow channels had formed within the soil sample during internal erosion, there was no need for the creation of more flow channels. The existing flow channels were sufficient to permit seepage at the current hydraulic gradient. Once stable flow channels are formed within the soil sample, the flow rate tended to be stable as well, indicating a stable state and the end of internal erosion.

The effect of initial relative density on the flow rate

To investigate the effect of initial relative density on flow rate during erosion, three samples, denoted as GG03, GG04, and GG08 with initial relative densities of about 30% 50%, and 70%, respectively, were prepared according to sample formation method described in Section 3.6. All soil samples had homogeneous particle size distributions and density throughout. The hydraulic gradient was 8 and a confining pressure was 50 kPa was applied as erosion took place. Each

sample had a total of 96×10^{-3} m^3 of water passed through them, through six upward-downward seepage cycles. The interval between each upward or downward seepage cycle was about 1 minute. Figure 4-2 shows the flow rate and average permeability with time. It is noted that each symbol, either a square, triangle or circle, indicates the end of a cycle of 8×10^{-3} m^3 of seepage.

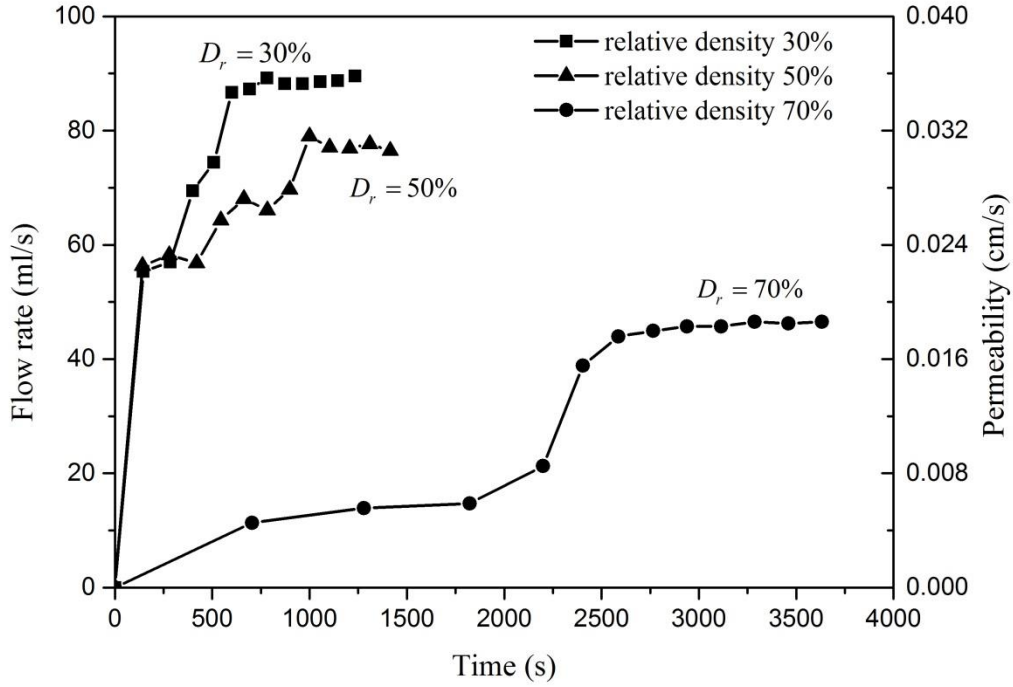

Figure 4-2 Flow rate and permeability with time considering the effect of initial relative density.

It can be seen from Figure 4-2 that the flow rate of all samples increased until stable flow rates were reached. It can be noted that the flow rate of the soil sample which had an initial relative density of 30% was the highest while the flow rate of the soil sample which had an initial relative density of 70% was the lowest. Flow rate within a soil sample increases with the decrease of the soil density. The different flow rates indicate that there is more energy dissipated (or head lost) in a dense soil implying that there is greater viscosity between the seepage water and soil particles. These findings are in accordance with those of Wan and Fell (2004). They

observed that samples compacted to a higher dry density had a higher erosion resistance than samples compacted at a lower dry density. Therefore, from the point of view of dam engineering, it can be concluded that it is crucial to compact soils to dense state to increase their ability to resist internal erosion.

It is also interesting to note that the flow rate for the sample with an initial relative density of 70% slightly increases for the first 2000s, then rapidly increases before finally becoming stable. This may be due to the fact that it usually takes a long time for the initiation and development of internal erosion within soils with high relative densities. As fine particles are gradually transported out from the soil sample, the density of the soil sample decreases while the flow rate increases.

The average permeability with time for each sample shows the same trend as the flow rate.

The effects of hydraulic gradient on flow rate

The magnitude of the hydraulic gradient influences the initiation and development of internal erosion. Some researchers identified a the critical value of the hydraulic gradient that internal erosion to initiate, by starting with a very small hydraulic gradient and then gradually increasing it until internal erosion was observed (Moffat 2005; Moffat et al. 2011; Sibille et al. 2015; Skempton and Brogan 1994; Wan and Fell 2004), other researchers monitored the evolution of the hydraulic gradient within a soil sample during internal erosion under a constant water head or a constant flow rate (Lin Ke 2014; Moffat et al. 2011). Bendahmane et al. (2008) found that the rate of internal erosion increases with the increase of the hydraulic gradient.

In order to investigate the effect of hydraulic gradient on flow rate here, two hydraulic gradients, 3.1 and 8, were applied to soil samples with the same confining stress (50 kPa) and the same

initial relative density (50%). A few trail tests were conducted first and showed that hydraulic gradients of 3.1 and 8 were sufficient to trigger the initiation of internal erosion within a soil sample with initial relative density of 50% under a confining stress of 50 kPa. Two tests, denoted as GG04 and GG29 were then conducted to investigate the effect of hydraulic gradient on flow rate. The test results are plotted in Figure 4-3. Once the erosion started, the flow rates of both samples increased until stable values were reached. The flow rate of the sample GG04 under a hydraulic gradient of 8 has a higher flow rate at all each stage compared to that for sample GG28 under a hydraulic gradient of 3.1. The total time consumed to cause passage of $8\times12\times10^{-3}$ m^3 of seepage water through the sample under hydraulic gradient of 8 was much less than that for the sample under a hydraulic gradient of 3.1. This can be explained by the fact that higher hydraulic gradient caused by higher water head leads to a higher flow rate of seepage.

The average permeability with time for each sample shows the same trend as flow rate.

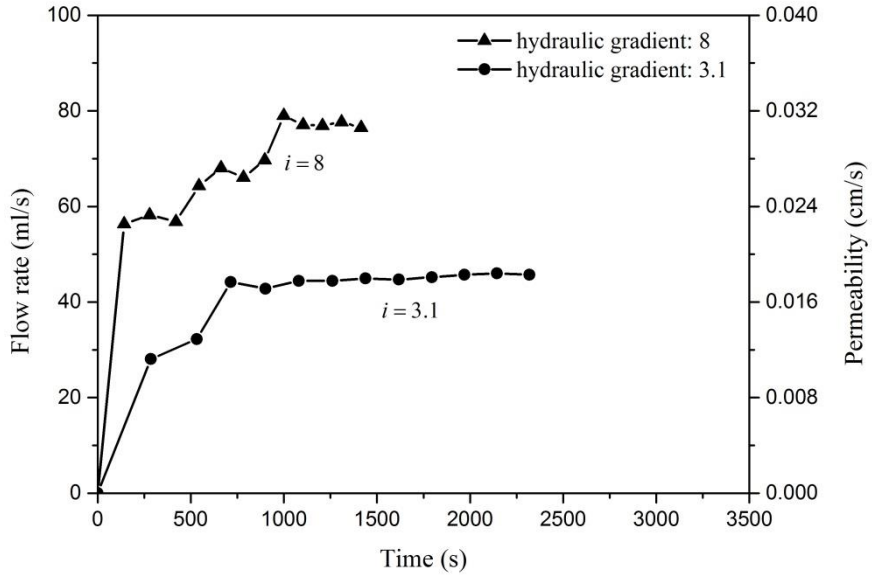

Figure 4-3 Flow rate and permeability with time considering the effect of initial hydraulic gradient.

The effect of confining stress on flow rate

Chang and Zhang (2012) observed that the critical hydraulic gradient for the initiation of internal erosion increases with the increase of the confining stress applied to a sample. They interpreted that at higher confining stresses the decreases of void ratio which occur due to compression as erosion take place were more pronounced. Here, the flow rate is used as indicator of the process of internal erosion, therefore, it is important to study the effect confining stress on flow rate.

The variation of flow rate with time for three tests, each of which was under a confining stress of 50, 100 or 200 kPa (denoted as GG11, GG17 and GG20, respectively) are shown in Figure 4-4. All samples have an initial relative density of 50% after compaction and were subjected to a seepage of 45×10^{-3} m^3 (through 3 upward-downward seepage cycles) under a hydraulic gradient of 8, sufficient for the onset of internal erosion under the largest confining stress 200 kPa. The flow rates of all samples increased with time. However, the sample under the least confining stress exhibited the largest flow rate. The sample under the largest confining stress exhibited the smallest flow rate. The initiation of significant internal erosion within samples occurs later as the confining stress is increased.

Due to different confining stresses, the samples exhibited different amounts of volumetric compression after erosion. The void ratios before the introduction of seepage of samples under 50, 100, and 200 kPa were 0.296, 0.281, and 0.278 respectively. These correspond to relative density of 56%, 60% and 61%, respectively.

The average permeability with time for each sample shows the same trend as the flow rate.

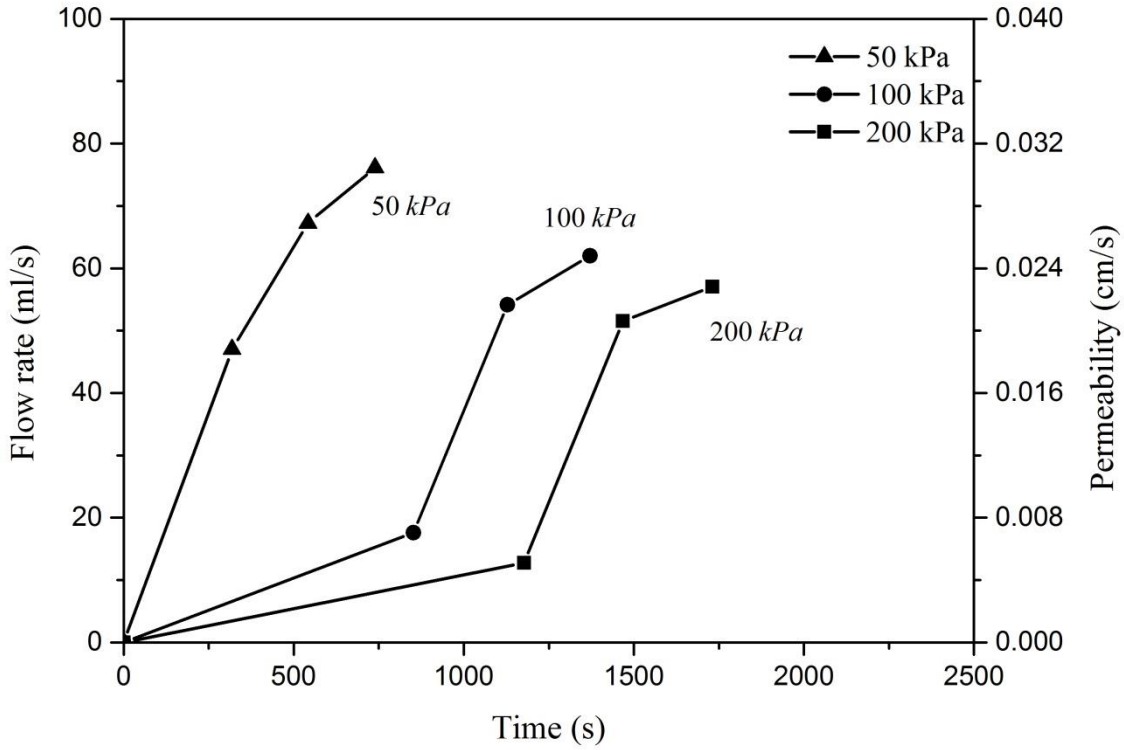

Figure 4-4 Flow rate and permeability under different confining stress.

4.2.3 Cumulative eroded soil mass with time

The cumulative eroded soil mass is another indicator that reflects the process of the initiation and development of internal erosion. The typical evolution of the cumulative eroded soil mass has been discussed in Section 3.8.3.

The cumulative eroded soil mass does not relate directly to the loss of fine particles. Not all fine particles that are lost from a sample are transported to the effluent collection system. Some are trapped in the drainage lines and conical depressions in the apparatus at each end of a sample. Even so, the cumulative soil mass is a useful indicator of erosion initiation and progression. In an extreme case, when the relative density of the soil sample was very low, a large number of

fine particles exited the sample quickly and blocked the drainage system, preventing an accurate judgment of the development of internal erosion to be made.

This section will focus on the effects on initial relative density, water head and confining stress on the cumulative eroded soil mass with time.

The effect of initial relative density on the cumulative eroded soil mass

The testing results of the cumulative eroded soil mass from samples GG03, GG04, and GG08, which had an initial relative densities of about 30%, 50%, and 70%, are presented in Figure 4-5. Each sample had a total of 96×10^{-3} m^3 of water passed through them, through six upward-downward seepage cycles. The cumulative eroded soil mass increases with time until a stable value is approached. It is noted that the first 8×10^{-3} m^3 of water transported a large amount of the eroded soil mass compared to subsequent seepage stages. And the mass of eroded soil gradually decreases with time. This is consistent with what others have reported in the literature, as mentioned in Section 3.8.3.

It is also noted that the cumulative eroded soil mass increases with the decrease of initial relative density. This is expected since, as described earlier, the flow rate also increases with the decrease of relative density.

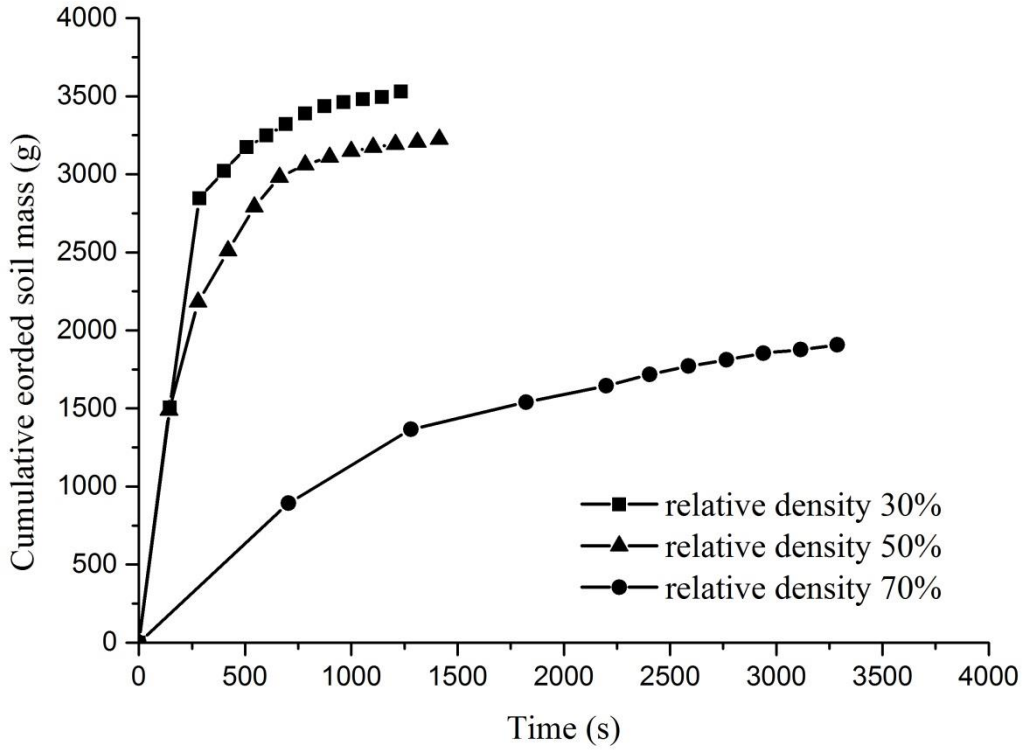

Figure 4-5 The effects of initial relative density on the evolution of cumulative eroded soil mass.

The effects of hydraulic gradient on the cumulative eroded soil mass

The cumulative eroded soil mass (total eroded soil mass, g) for samples GG04 and GG29, which were subjected to seepage with hydraulic gradient of 8 and 3.1, respectively, are presented in Figure 4-6. It is noted that the soil sample subjected to seepage with hydraulic gradient of 8 experienced significantly more fine particle loss at the beginning of internal erosion compared to that of the soil sample subjected to seepage with hydraulic gradient of 3.1. This is consistent with Sibille et al. (2015)'s conclusion that the cumulative eroded soil mass increases with hydraulic gradient.

The higher hydraulic gradient induces a higher hydraulic shear stress. When seepage passing through the soil skeleton that made up by coarse particles, in which fine particles attach to the surface of coarse particles or fill the pore space around coarse particles, the fine particles are more easily removed as hydraulic shear stress increases.

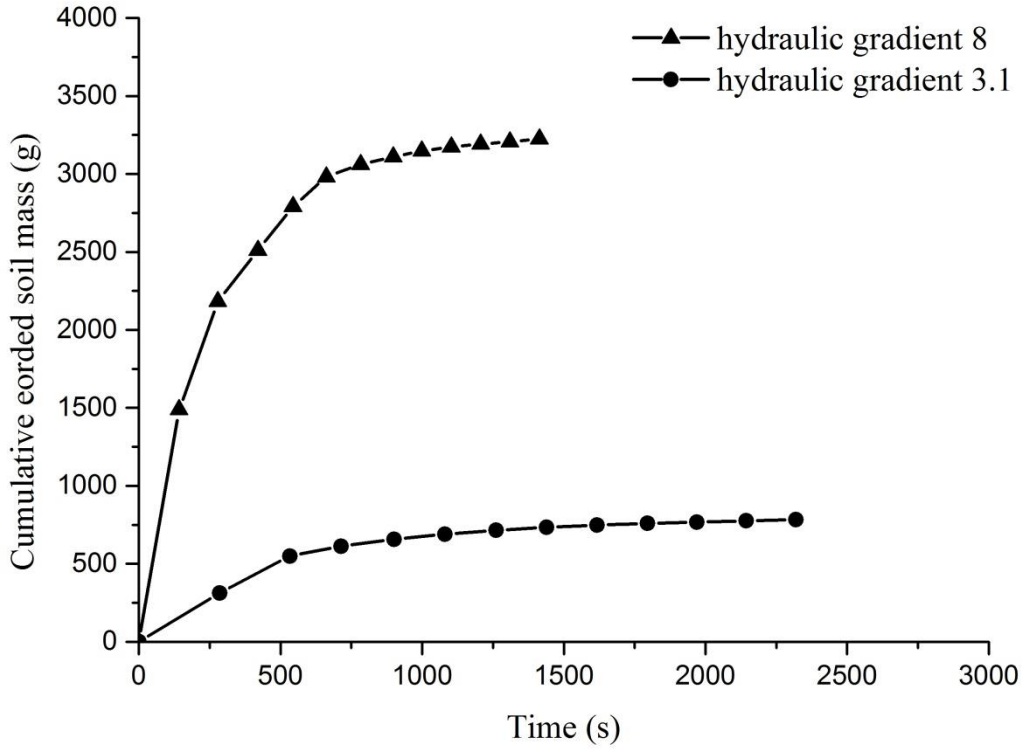

Figure 4-6 The effects of hydraulic gradient on the evolution of cumulative eroded soil mass.

The effect of confining stress on cumulative eroded soil mass

The evolution of cumulative eroded soil mass for samples GG11, GG17 and GG20 (each under a confining stress of 50, 100 and 200 kPa, respective) are compared to investigate the effects of confining stress. The cumulative eroded soil mass with time for each sample is plotted in Figure 4-7. It is noted that cumulative eroded soil mass is greatly effected by confining stress. The

cumulative eroded soil mass of the sample with 50 kPa confining stress exhibits a rapid increase compared to those for the other two samples with 100 and 200 kPa confining stress. It is evident that the initiation of internal erosion occurs later as the confining stress is increased. As discussed in Section 4.2.2, soil samples under high confining stresses are densified and their relative densities are increased.

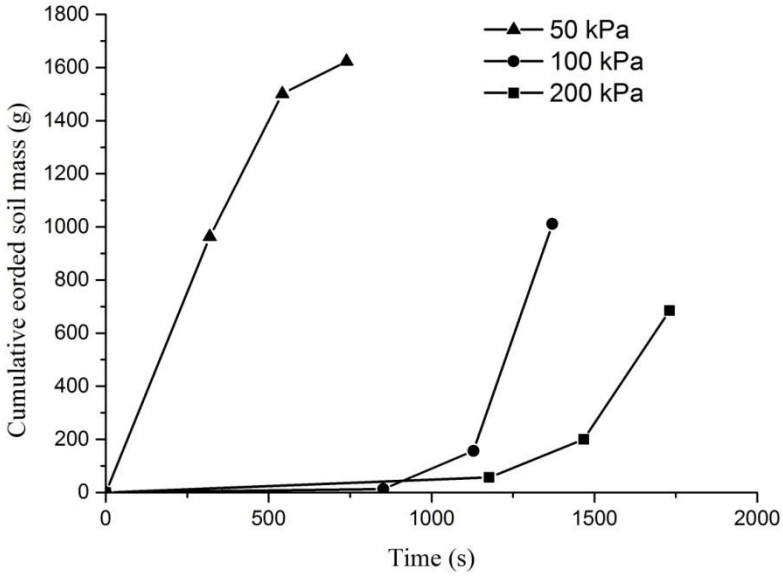

Figure 4-7 The effects of effective stress on cumulative eroded soil mass.

The limitation of using the cumulative eroded soil mass as an indicator of the development of internal erosion

A major limitation of using the cumulative eroded soil mass as an indicator of the development of internal erosion is that it may underestimate the fine particle loss during internal erosion. The mass of fine particles lost, primarily by deposition in the drainage system and the conical cavities at each end of the sample, may be considerable.

A summary of internal erosion test conditions is given in Table 4-1. A comparison of the cumulative eroded soil mass and the total fine mass of soil samples tested is given in Table 4-2.

Table 4-1 Summary of internal erosion test conditions

Soil sample	Initial relative density	Confining stress (kPa)	Hydraulic gradient	Seepage passing through (10^{-3} m^3)
GG03	30%	50	8	12×8
GG04	50%	50	8	12×8
GG08	70%	50	8	12×8
GG11	50%	50	8	3×15
GG17	50%	100	8	3×15
GG20	50%	200	8	3×15
GG29	50%	50	3.1	12×8

Table 4-2 Comparison between the cumulative soil mass and the total soil mass

Soil sample	Cumulative eroded soil mass at the end of erosion (g)	Deposited soil mass (g)	Fine mass loss during saturation (g)	Total mass loss (g)	The ratio between cumulative eroded soil mass and total loss
GG03	3528.8	489.1	40.5	4199.8	0.840
GG04	3224.2	422.1	55.3	3701.6	0.871
GG08	1944.3	378.4	22.8	2345.5	0.829
GG11	1623	211.5	23.7	1858.2	0.873
GG17	1010.9	177.1	8.7	1196.7	0.845
GG20	684.6	262.4	15.2	962.2	0.710
GG29	783	341.1	71.4	1197.5	0.654

The mass of fines lost including deposited in the drainage system and conical cavities, should not be overlooked as it may result in the wrong calculation in grading state index, which is a key parameter in modelling the influences of internal erosion on a soil's mechanical behavior (Kikumoto et al. 2010; Muir Wood et al. 2010; Muir Wood and Maeda 2008).

4.2.4 Other observations

Vertical settlement

The vertical settlement was measured by reading the vertical differences between where a horizontal laser mark was projected on the top cap of the soil sample before and after the seepage test. Of all the triaxial erosion tests, only a few indicated a small vertical settlement, being less than 1 mm. Therefore, the vertical settlement was neglected in subsequent calculations of volume and height.

Volume strain

The volume change was determined using the differences of triaxial cell volume change recorded at the end of each upward-downward erosion circle. The volume changes in all tests were minor. A typical volumetric strain evolution is shown in Figure 4-8. It is noted that the soil sample reduced in volume at all times, albeit it by very small amounts, and the reduction was most pronounced during the initial stages when particle removal is most prevalent. The volumetric strain at the end of internal erosion was about 0.002, quite negligible, even though the changes in flow rate (as reported in section 4.2.2) were evident. Therefore, according to Fannin and Slangen (2014)'s recommendations, the classification of the internal erosion is suffusion. In other words, a seepage-induced fine mass loss occurs without a change in global volume, but is accompanied by an increase in flow rate or hydraulic conductivity.

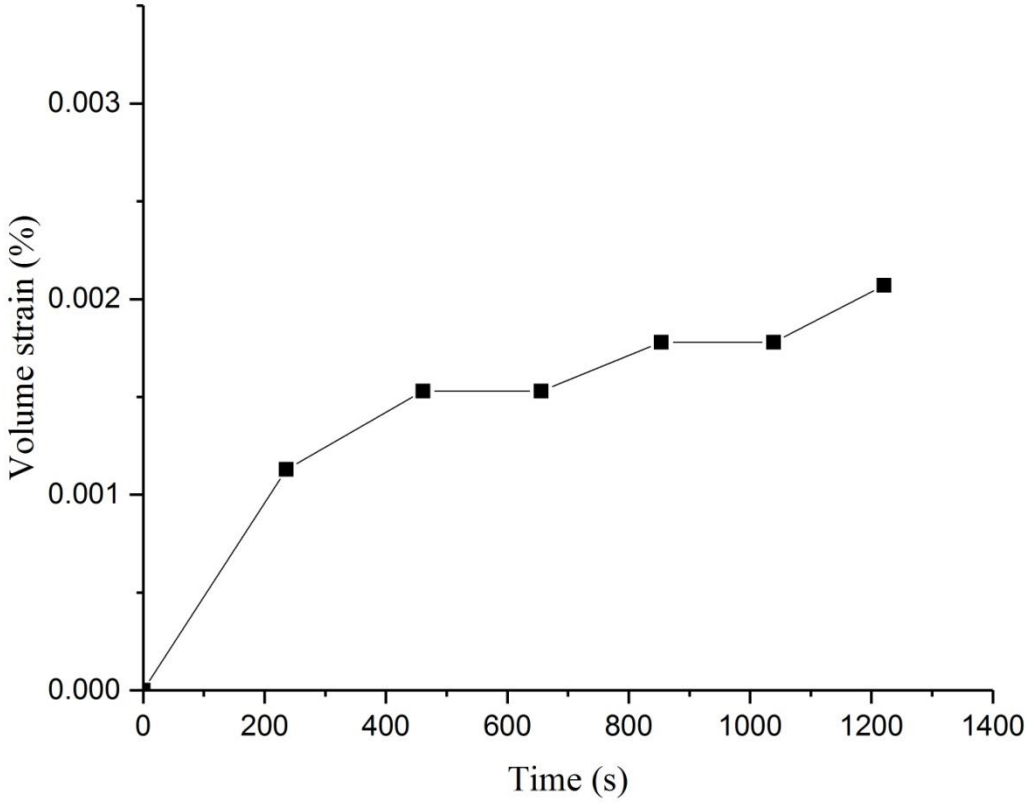

Figure 4-8 Volumetric strain with time.

Color of effluent

It is common to use turbidity to describe the degree to which the exiting seepage water looses its transparency due to the presence of suspended particles. In a series of erosion tests, Indraratna et al. (2008) found that there is a linear relationship between the concentration of particles in the seepage water and the turbidity.

However, in trials conducted here, it was found that at the early stages, when a large number of fines were washed out by the seepage, the turbidity meter was unreliable. Instead, a description of the color of the effluent is preferred here.

Typically, the color of the effluent was transparent during the first 10 seconds. Then erosion initiated and the color rapidly turned to dark pale (as shown in Figure 4-9). As internal erosion continued and gradually reduced, a gradual fade in color was observed, with the effluent becoming nearly transparency (as shown in Figure 4-10), indicating the end of internal erosion.

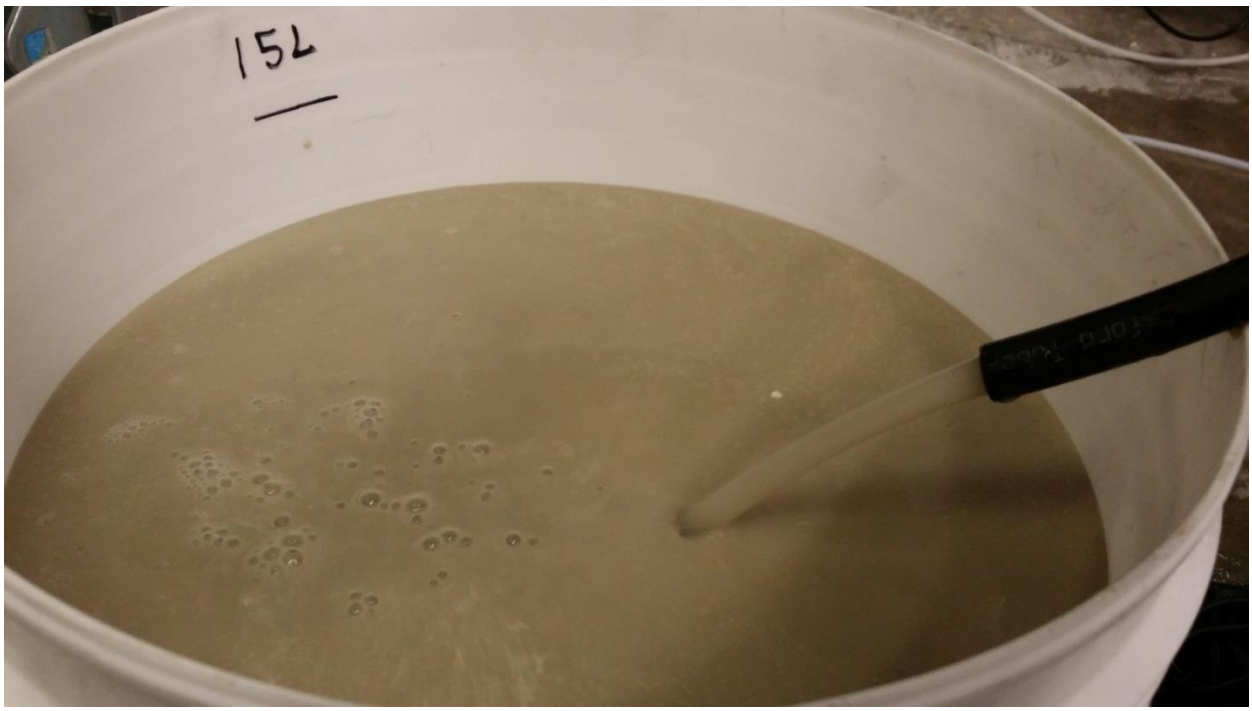

Figure 4-9 Photo of effluent at the early stage of internal erosion.

Figure 4-10 Photo of effluent at the early stage of internal erosion.

4.3 STRESS-STRAIN BEHAVIORS OF SOILS HAVING UNDERGONE INTERNAL EROSION

4.3.1 Introduction

To investigate the mechanical consequences of internal erosion on soils, numerous samples at an initial relative density of 50% were subjected to different amounts of internal erosion under a hydraulic gradient of 3.1. They were sheared under different effective confining stress, 50, 100, and 200 kPa, in drained conditions. This section presents the results of the tests.

The triaxial erosion tests involved subjecting cylindrical samples to a confining pressure (50, 100 or 200 kPa), introducing desired circles of upward-downward seepage flow to cause different amounts of internal erosion and measures the sample volume change which occurred. The subsequent triaxial compression shear tests were conducted at an axial displacement rate of 0.2 mm/min. Sample deformations were measured every 20 seconds. The compression tests, which usually took 6-7 hours to reach a shear strain of 18-20%, revealed asymptotic states which may be interpreted as critical states (Figures 3-30, 3-31 and 3-32).

Although sample volume change could be determined using either the pore water or cell water volume changes (as shown in Figure 4-11), the pore water volume change method was adopted as it was more straightforward and accurate. Before each test, the level of the oil-water interface in the pore volume change burette, which had a total volume change measuring capacity of 500 ml, was set to 200 ml. This allowed sufficient space for both compression (the oil-water interface to move upwards) and dilation (the oil-water interface to move downwards). As the pore volume changes in most tests were substantially larger than the burette's capacity, it was necessary to adjust the level of the oil-water interface during each test (usually midway through the test). This adjustment was done very quickly and skillfully without disturbance of the tests, so that it had a negligible effect on the volume change readings.

It was also necessary to check the magnitude of creep of the triaxial cell as each test including seepage and shearing took about 120 hours to complete. A cell creep test was performed by applying a cell pressure of 500 kPa (the highest cell pressure applied in any of the tests was 410 kPa) for 7 days without a sample inside and monitoring its volume change during this time. However, no volume change was observed during the creep test once the cell pressure read reached 500 kPa.

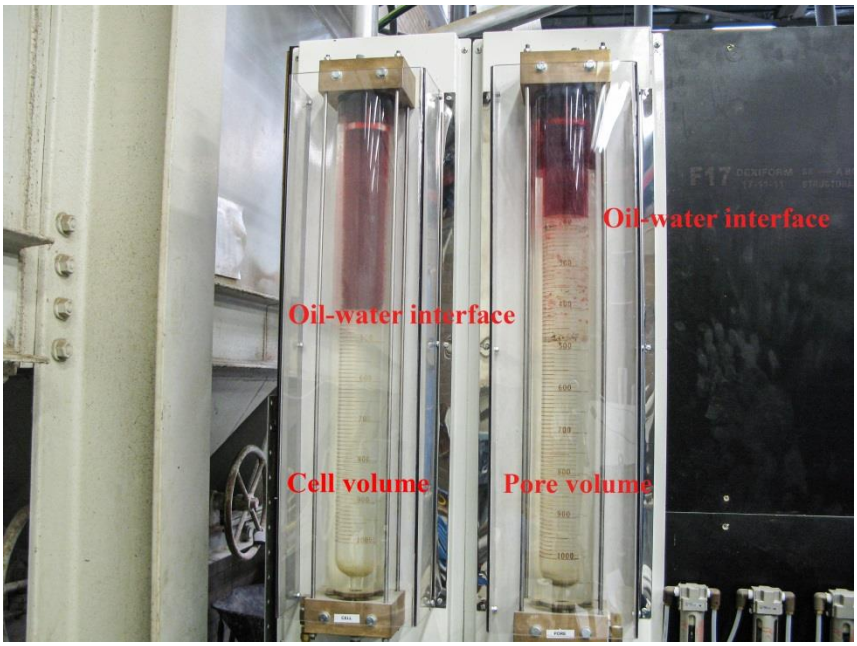

Figure 4-11 Oil-water interface for cell and pore volume determination.

The soil samples experienced different amounts seepage as they eroded. There are many ways to describe quantitatively the amount of internal erosion that a soil sample has experienced: (1) the volume of water that was passed through the soil sample; (2) the percentage of the total eroded soil mass; and (3) the grading state index, proposed by Muir Wood (2007). The above three descriptors are used in different contexts. To clearly describe the erosion process, the first descriptor is adopted. To quantify the consequences of internal erosion on soils in triaxial tests, a combination of the first and second descriptors may be used. To quantify the influences of internal erosion on particle size distribution for constitutive modelling, the third is used, and will be utilized extensively here in Chapter 6.

4.3.2 Conventional triaxial p'-q notation

The conventional triaxial $p'-q$ notations are used throughout:

Mean effective stress $p' = (\sigma_1' + 2\sigma_3')/3$;

Deviator stress $q = \sigma_1^{'} - \sigma_3^{'}$;

Volumetric (isotropic) strain $\varepsilon_p = \varepsilon_1 + 2\varepsilon_3$;

Shear (deviator) strain $\varepsilon_q = 2(\varepsilon_1 - \varepsilon_3)/3$.

where $\sigma_1^{'}$ and $\sigma_3^{'}$ are principal effective stresses, and ε_1 and ε_3 are the conjugate principal strains. A superscript dash denotes the invariant to be effective, subscripts 1 and 3 denote the axial and radial components respectively.

Compressive stresses and strains are assumed to be positive and volumetric (isotropic) strain is given as:

$$\varepsilon_p = -\ln(\frac{v}{v_0}) \qquad (4\text{-}3)$$

and has the incremental form:

$$\delta\varepsilon_p = \frac{-\delta v}{v} \qquad (4\text{-}4)$$

where v is the specific volume ($v = 1 + e$), e is the void ratio and v_0 is the specific volume at a reference condition.

4.3.3 Stress-strain behavior of soils having undergone different amounts of internal erosion under the effective confining stress of 50 kPa

Section 3.7.4 presented two sets of samples compacted by two different sample formation methods and subjected to 8, 24, and 48×10^{-3} m^3 of seepage under a hydraulic gradient of 3.1. The samples were then sheared under an effective confining stress of 50 kPa. The properties of the samples and experimental conditions are noted in Table 3-5. The results of those two sets of tests are replotted here in Figure 4-12 and Figure 4-14 and discussed, together with the other three tests that were conducted at different hydraulic conditions.

Three soil samples (denoted as GG12HET, GG11HET, GG09HET) were compacted using the conventional compaction procedure to an initial relative density of about 50% and subjected to 15, 45 and 90×10^{-3} m^3 of seepage under a hydraulic gradient of 8. The results of drained compression shear tests on these soil samples are presented here. The properties of the samples and experimental conditions are noted in Table 4-3. Figure 4-12(a) and (b) show the stress-strain behavior of the soils which undergone different amounts of internal erosion (GG14, which had not experienced erosion, was added for comparison). The friction angles in Table 4-3 were obtained by assuming zero cohesion.

From Figures 4-12, 4-13 and 4-14, it is again noted that the peak strengths (peak deviator stress) reduce as internal erosion increases, in agreement with Muir Wood et al. (2010), Chang and Zhang (2011), Ke and Takahashi (2014b). The strengths tend to decrease as the volume of seepage water and erosion increase. The rate at which the strength decrease occurs tends to dissipate as the volume of seepage water increases. This is consistent with the slow-down of the rate of eroded soil mass accumulation as presented in Section 4.2.3.

The constant volume (large strain) shear strengths exhibited a different trend. The sample which experienced the most erosion (from 90×10^{-3} m^3 of seepage) has a larger strength than those which experienced lesser internal erosion (from 15 and 45×10^{-3} m^3 of seepage). At large strains, where the initial (post-erosion) sample density is not expected to affect prevailing strength, the increasing coarseness of particle size distribution following erosion may be the cause for the

strength increase. This trend is consistent with the findings of Chang et al. (2014). However, the increasing coarseness of the particle size distributions in the eroded samples does not explain why they had lesser constant volume strengths than the sample which had not experienced internal erosion.

As can be seen in Figures 4-12(b), 4-13(b) and 4-14(b) the volumetric deformations of samples became less contractive at small shear strains with increasing amounts of internal erosion. Also, at large shear strains, the samples which had undergone erosion exhibited a reduced tendency for dilation compared to the sample which had not experienced internal erosion. The erosion caused the samples to become looser and thus tend to be more contractive at large shear strains, in agreement with Scholtès et al. (2010) and Chang and Zhang (2011).

Table 4-3 Summary of triaxial compression test conditions and results of GG14, GG12HET, GG11HET and GG09HET.

Sample	Seepage passing through (10^{-3} m^3)	Percentage of fine particle mass loss (%)	Peak strength (kPa)	Friction angle at peak (°)	Friction angle at large strain (°)
GG14	0	0	386	52.6	43.8
GG12HET	1×15	4.6	295	47	43
GG11HET	3×15	7.1	272	46.7	43.5
GG09HET	6×15	9.8	268	46.3	43.8

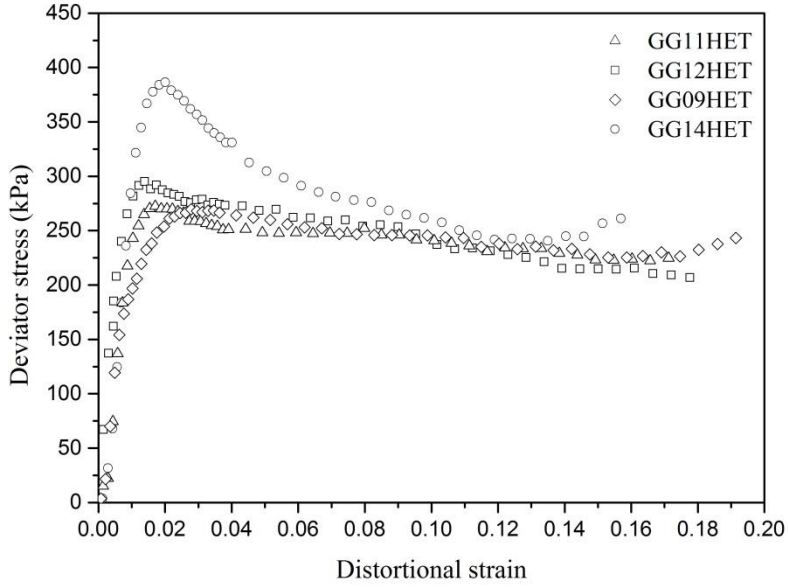

(a)

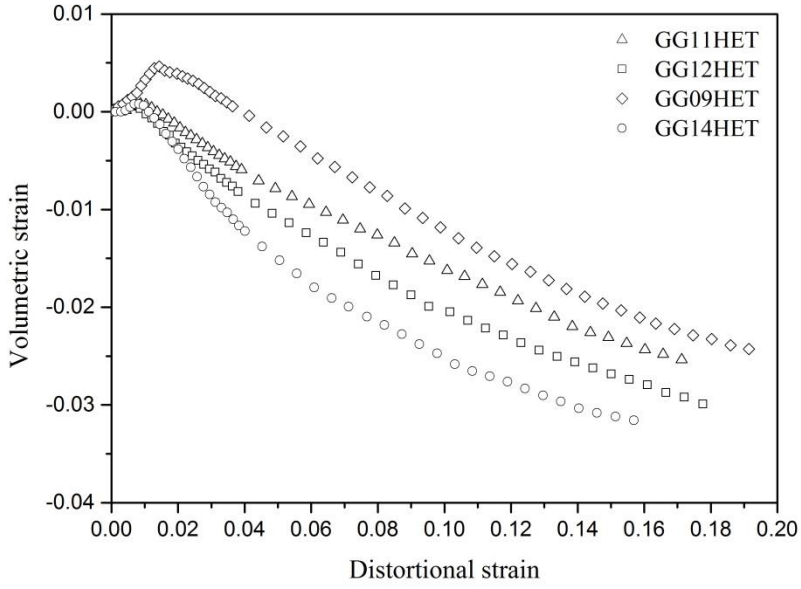

(b)

Figure 4-12 Drained compression tests on samples (GG11, GG12, GG09 and GG14) subjected to different amounts of internal erosion. (a) Stress-strain relationships. (b) Volumetric strain and shear strain relationships.

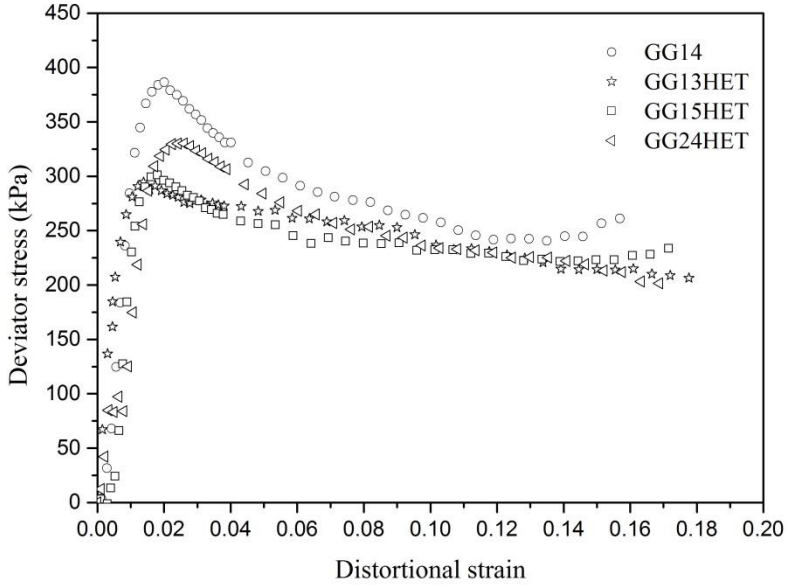

(a)

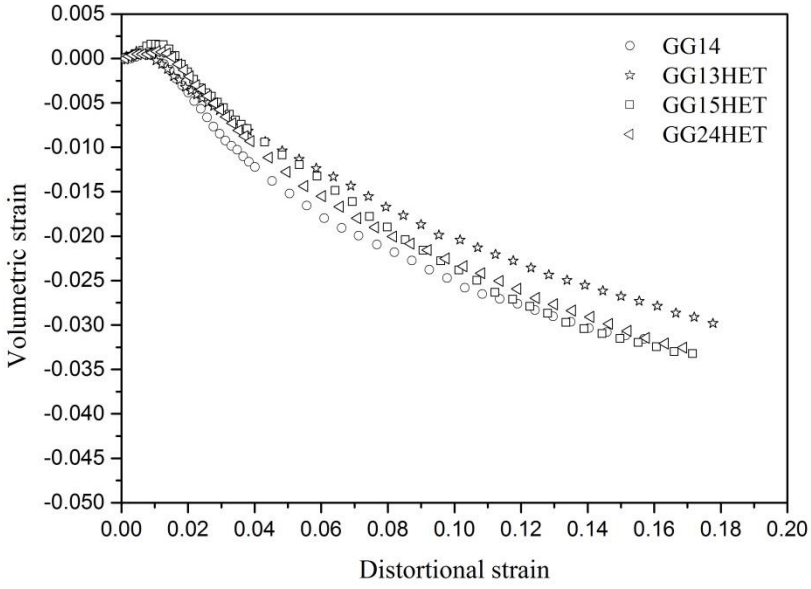

(b)

Figure 4-13 Drained compression tests on samples (GG14, GG13HET, GG15HET and GG24HET) subjected to different amounts of internal erosion. (a) Stress-strain relationships. (b) Volumetric strain and shear strain relationships.

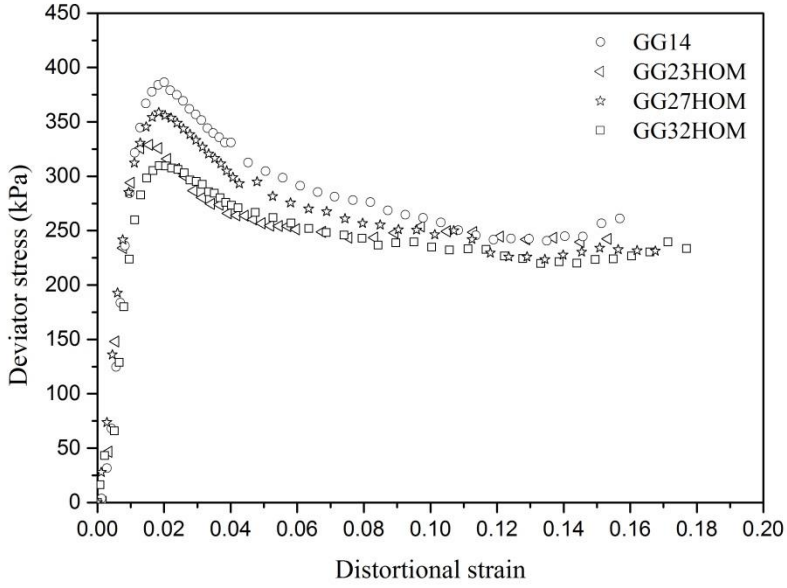

(a)

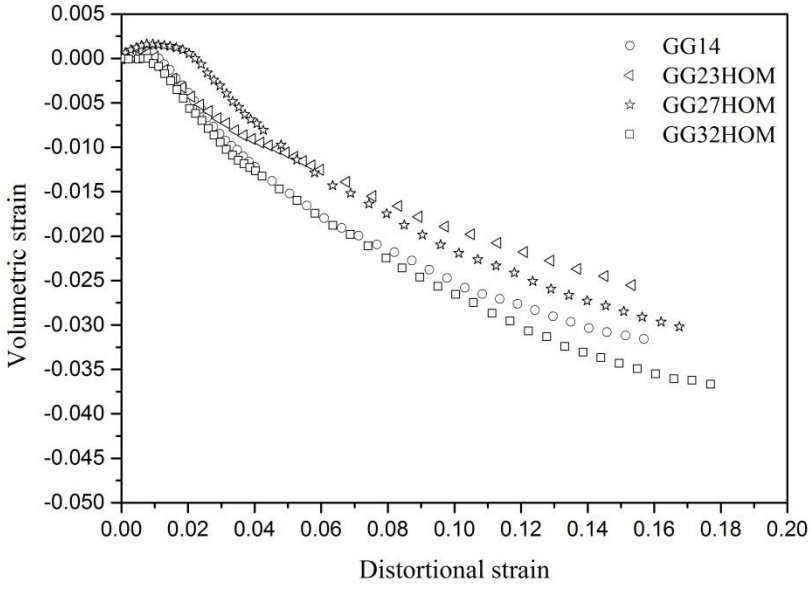

(b)

Figure 4-14 Drained compression tests on samples (GG14, GG23HOM, GG27HOM and GG32HOM) subjected to different amounts of internal erosion. (a) Stress-strain relationships. (b) Volumetric strain and shear strain relationships.

4.3.4 Stress-strain behavior of soils having undergone different amounts of internal erosion under the effective confining stress of 100 kPa

This section presents the results of drained monotonic triaxial compression of soil samples having undergone 8, 24, and 48×10^{-3} m^3 of seepage under a hydraulic gradient of 3.1. The applied effective confining stress was 100 kPa. Sample GG18 was compacted by the conventional compaction procedure and was not subjected to erosion prior to shearing. The samples GG39HOM, GG38HOM and GG31HOM were prepared by the new procedure and each of them has a near homogeneous post-erosion particle size distribution throughout the sample. The properties of the samples and experiment conditions that the samples were conducted are noted in Table 4-4.

Table 4-4 Summary of triaxial compression test conditions and results of GG18, GG39HOM, GG38HOM and GG31HOM.

Sample	Seepage passing through (10^{-3} m^3)	Percentage of fine particle mass loss (%)	Peak strength (kPa)	Friction angle at peak (°)	Friction angle at large strain (°)
GG18	0	0	583.1	48.3	44.1
GG39HOM	1×8	3.7	555.2	47.1	43.4
GG38HOM	3×8	6.05	537.2	46.7	42.9
GG31HOM	6×8	8.9	494.5	45.2	42.5

Figure 4-15 (a) and (b) show the stress-strain behaviors of the sample which had undergone different amounts of internal erosion.

From Figure 4-15 and Table 4-4, it is again noted that the peak strength, and friction angle at the peak, is lower for a sample which had experienced internal erosion. The peak strength tends to decrease with the increase of the volume of seepage water and erosion. This is consistent with the trend of the change in soil strengths observed for an effective confining stress of 50 kPa, as presented in Section 4.3.3.

The sample which experienced the most erosion (GG31HOM, from 48×10^{-3} m^3 of seepage) had a lower strength than those which experienced lesser internal erosion (from 8 and 24×10^{-3} m^3 of seepage).

Again, as can be seen in Figure 4-15(b), the volumetric deformations of a sample became less contractive at small shear strains with the increase of internal erosion. The samples subjected to internal erosion showed a decreased tendency for dilation compared to the sample which had not been subjected to internal erosion.

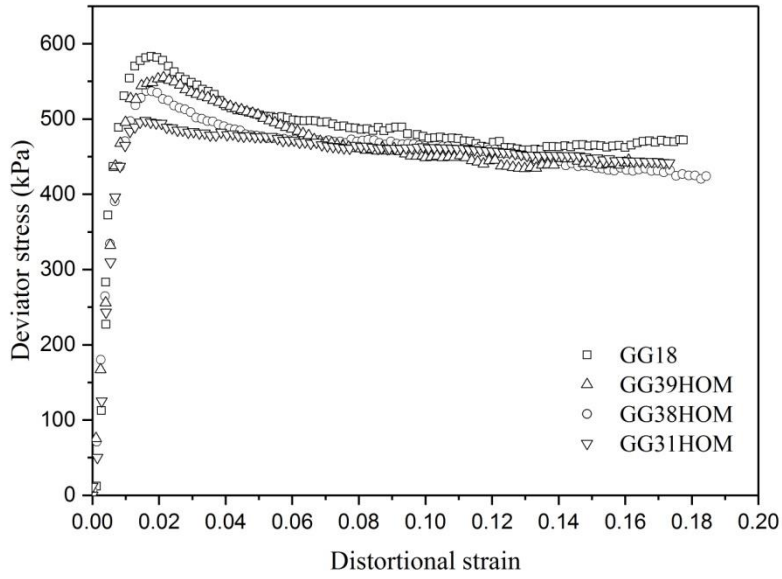

(a)

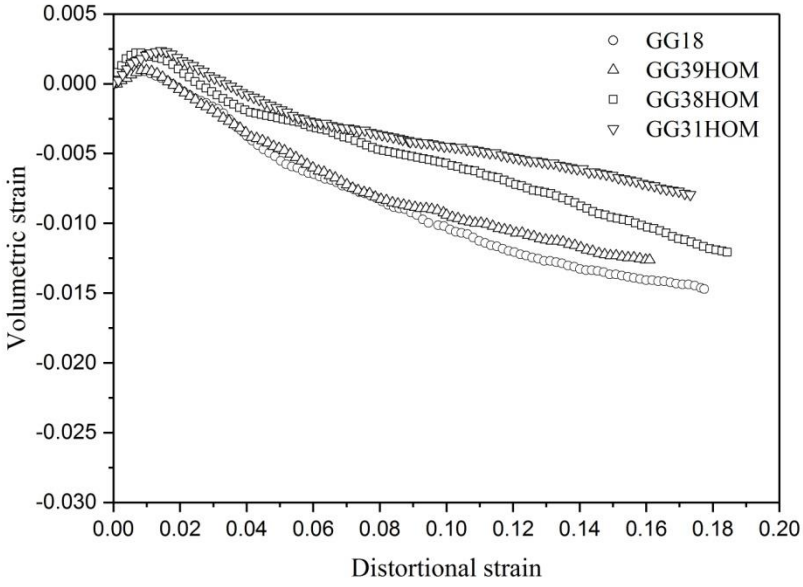

(b)

Figure 4-15 Drained compression tests on samples (GG18, GG39HOM, GG38HOM and GG31HOM) subjected to different amounts of internal erosion. (a) Stress-strain relationships. (b) Volumetric strain and shear strain relationships.

4.3.5 Stress-strain behavior of soils having undergone different amounts of internal erosion under the effective confining stress of 200 kPa

This section presents the results of drained monotonic triaxial compression of soil samples having undergone 24 and 48×10^{-3} m^3 of seepage under a hydraulic gradient of 3.1. The applied effective confining stress was 200 kPa. Sample GG18 was compacted by the conventional compaction method and was not subjected to erosion prior to shearing. The samples GG36HOM and GG37HOM were prepared by the new procedure and each of them had a near homogeneous post-erosion particle size distribution throughout the sample. The properties of the samples and experimental conditions that the samples were conducted are noted in Table 4-5. Since the samples exhibit a strain hardening behavior, only the friction angle and strength at large strains are given.

Table 4-5 Summary of triaxial compression test conditions and results of GG16, GG36HOM and GG37HOM.

Sample	Seepage passing through (10^{-3} m^3)	Percentage of fine particle mass loss (%)	Maximum strength (kPa)	Friction angle at large strain (°)
GG16	0	0	852.5	42.7
GG36HOM	3×8	5.85	827.6	42.2
GG37HOM	6×8	9.3	816.9	42.5

Figure 4-16(a) and (b) show the stress-strain behaviors of the samples which had undergone different amounts of internal erosion.

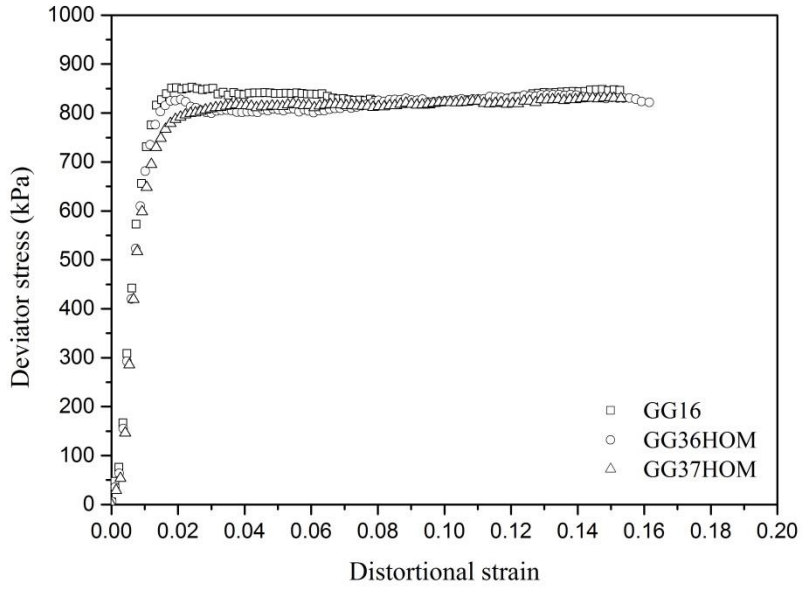

(a)

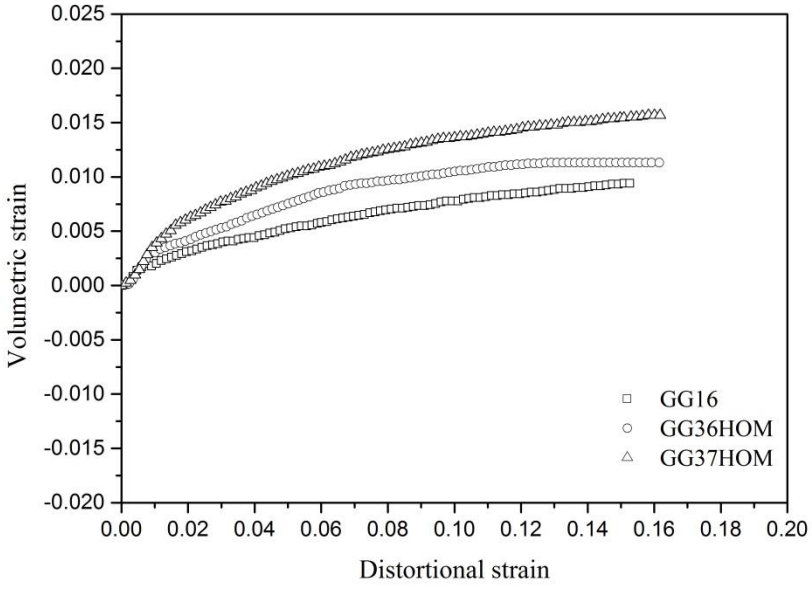

(b)

Figure 4-16 Drained compression tests on samples (GG16, GG36 and GG37) subjected to different amounts of internal erosion. (a) Stress-strain relationships. (b) Volumetric strain and shear strain relationships

Samples exhibited strain softening and dilation at the effective confining stresses of 50 and 100 kPa. Here, with a larger confining stress of 200 kPa, strain hardening and contractive behaviors occurred. At large strains there were no noticeable differences in strength whatever the amount of erosion. However, it is clearly noticeable that the volumetric strain increases as the erosion increases.

4.4 EVOLUTION OF SOIL STATE DUE TO INTERNAL EROSION

For soils with the same initial relative density and fines content attained different gradings and void ratios once they subjected to different amounts of internal erosion. Such changes in grading and void ratio influence the basic constitutive properties of the soil material, particularly for the critical states which are dependent on the packing of soil particles. DEM by Muir Wood and Maeda (2007) and Hicher (2013) have showed the dependence of critical state lines on the grading of soils. Thus, different critical state lines are expected to prevail for the soils which had undergone different amounts of internal erosion. Over the stress ranges, straight lines on compression plane are able to well represent the critical state lines for each set of tests. According to Muir Wood et al. (2010), the dominant effect of a changing grading due to internal erosion is that the critical state line moves upwards. The slopes of the critical state lines for soils having undergone different amounts of internal erosion are assumed to remain unchanged. With this assumption, the critical state lines of the test soils after different amounts of erosion can be obtained, as shown in Figure 4-17.

In Figure 4-17, the solid line represents the critical state line of soils having not subjected to internal erosion, and the dashes line represent the estimated critical state line for soils having undergone different amounts of internal erosion. With the assumption that the slope of critical state line keeping the same, it can be seen that the critical state line tends to move upwards with the increase of internal erosion, in accordance in Muir Wood and Maeda (2007). This is partly due to the soil being sheared from progressively looser initial states, and partly due to the

changing grading making the soil become differently. The state parameters (the volumetric distance between the current specific volume v and the specific volume v_{cs} at the critical state or void ratio e at the same mean effective stress, which will be discussed in detail in Section 6.2.1) before and after erosion can then be determined. The state parameters of samples before erosion at 50, 100 and 200 kPa were -0.118, -0.081 and -0.041, respectively. The state parameters of samples subjected to 48×10^{-3} m^3 of seepage were -0.105, -0.077 and -0.031. It can be seen that after erosion the critical state line (dash lines) moves upwards and the specific volume is increased, but the increase in specific volume is greater than the vertical distance that the critical state line moves.

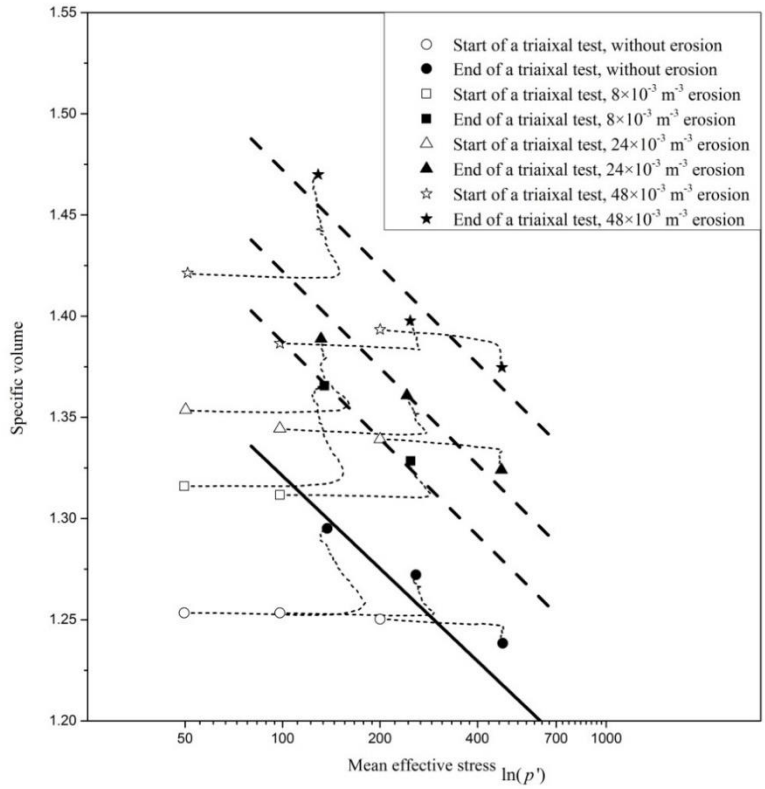

Figure 4-17 Critical state of selected testing samples subjected to varying amounts of internal erosion in space.

The link between the critical state lines of soils having undergone different amounts of internal erosion and the grading characteristics due to erosion may be established for modelling the effects of internal erosion.

4.5 DISCUSSION AND CONCLUSION

A range of experimental results has been presented which shown how erosion process experimental results of erosion characteristics under different conditions. The stress-strain behavior of soils having undergone different amounts of internal erosion have also been presented in this Chapter.

The hydraulic gradient, confining stress and initial density have significant influences on the erosion characteristics, especially flow rate and cumulative eroded soil mass. The flow rate decreases with the increase of density or effective confining stress. It increases with the hydraulic gradient being applied. The cumulative eroded soil mass increases with the increase of hydraulic gradient and decreases with the increase of initial density and effective confining stress.

The stress-strain behavior of soils having undergone different amounts of internal erosion at varying effective stress states have been investigated. The peak deviator stress tends to decrease as the volume of seepage water and amount of erosion increase. The volumetric strain at large shear strains decreases as the volume of seepage water and amount of erosion increase. Internal erosion also causes the critical state line to move upwards. The upward movement of the critical state line is lesser than the increase of void ratio due to internal erosion.

CHAPTER 5 THE FRACTAL CHARACTERIZATION OF SOILS SUBJECTED TO INTERNAL EROSION

5.1 INTRODUCTION

This chapter outlines the fractal characterization of soils subjected to internal erosion, including when changes to particle size distributions and void ratios occur. The main objectives of this chapter are:

- to develop direct mathematics links between fractal dimension and void ratio, applicable to soils with single or double fractal particle size distribution(s);
- to study the influences of internal erosion on the fractal dimension of soils;
- to apply the mathematical links between fractal dimension and void ratio to gap-graded soils subjected to internal erosion.

The internal erosion considered is of the suffusion type, ie, is characterized by seepage-induced fine particle loss without a change in the total volume of soil.

The theoretical links between fractal dimension and void ratio are implemented into a study of influences of internal erosion on soils in Chapter 6.

5.2 FREQUENTLY USED SYMBOLS

Some mathematical symbols that are frequently used in this Chapter and are applicable to a gap-graded soil in which two fractal sets define the finer and coarser components are listed in Table 5-1. A fractal material can be considered to have a total volume V and contains particles of

different sizes that are ordered in size. It will be detailed in Section 5.3.1. Erosion removes particles from the finer component only.

Table 5-1 Physical properties of the gap-graded test soil

Symbols	Finer component, before erosion	Coarser component, before erosion	Finer component, after erosion	Coarser component, after erosion
Maximum particle size	$d_{sf\max 0}$	$d_{sc\max}$ (assumed constant)	$d_{sf\max 1}$	$d_{sc\max}$ (assumed constant)
Minimum particle size	$d_{sf\min 0}$	$d_{sc\min}$ (assumed constant)	$d_{sf\min 1}$	$d_{sc\min}$ (assumed constant)
Fractal dimension	D_{sf0}	D_{sc} (assumed constant)	D_{sf1}	D_{sc} (assumed constant)
μ	μ_{f0}	μ_c	μ_{f1}	μ_c
n	n_f	n_c (assumed constant)	n_f	n_c (assumed constant)
p	p_{f0}	p_c (assumed constant)	p_{f1}	p_c (assumed constant)
Λ	Λ_f	Λ_c (assumed constant)	Λ_f	Λ_c (assumed constant)
Total soil volume	V_f	V_c	-	-

μ is the ratio between the volume of particles of order *k* and the total volume, and is always smaller than 1; n represents the ratio between individual particle volumes of successive orders and is a material constant; p is a material constant representing the ratio between total particle volumes of successive orders; Λ is a geometric shape factor.

5.3 A THEORETICAL LINK BETWEEN VOID RATIO AND FRACTAL DIMENSION OF PARTICLE SIZE DISTRIBUTION

Russell (2010, 2011) and Russell and Buzzi (2012) described the pore size distribution and other geometrical characteristics of pores using fractal theory. These descriptions may be used when describing the evolution of the void ratio of soils with fractal particle size distributions due to internal erosion.

There are a few important assumptions that need to be made in order to use fractals to describe the evolution of void ratio.

First of all, particle removal due to internal erosion only occurs in the fines component and this happens to be consistent with what was observed in the experiments.

Secondly, the type of internal erosion is suffusion, as stated in Section 5.1. During suffusion, the total volume of soil V does not change. Also the total volume of the solids in the coarse fraction V_c is a constant. Coarse particles act as the soil skeleton and are not be transported out from the soil sample by seepage.

Thirdly, the pre- and post-erosion particle size distributions of the fine component can be characterized using fractals. The test soil, which was deliberately reconstituted to be a gap-graded soil, can be divided into a coarser fraction and a finer fraction. Both fractions have fractal particle size distributions and are presented in rescaled plots in Figure 5-1. Figure 5-1 presents plots of the logarithm of percentage finer by mass against the logarithm of particle size. The

fractal dimensions of finer and coarser components, D_{sf0} and D_{sc}, can be obtained from the rescaled plots using $slopes = 3 - D_{sf0}$ and $3 - D_{sf}$, respectively.

Lastly, it is assumed that the maximum and minimum particle sizes of the finer component do not change during erosion. Preferential flow channels form as suffusion progresses, although there exit local zones where fines are not transported away by seepage. There always remains some amounts of fines, of all sizes, in the void space of the soil. Alternatively, Muir Wood et al. (2010) assumed the smallest particles were removed first and then coarser particles were progressively removed, stage by stage, resulting in an increase in the minimum particle size as internal erosion continued. This deliberate and selective removal of the smallest particles is algorithmically and theoretically simple but is less physically realistic. From the assumption that is made here, the results of post-erosion particle size distribution curves of Chang and Zhang (2011) and Ke and Takahashi (2012), and experimental observations in this work, indicate the minimum particle size remains the same during internal erosion.

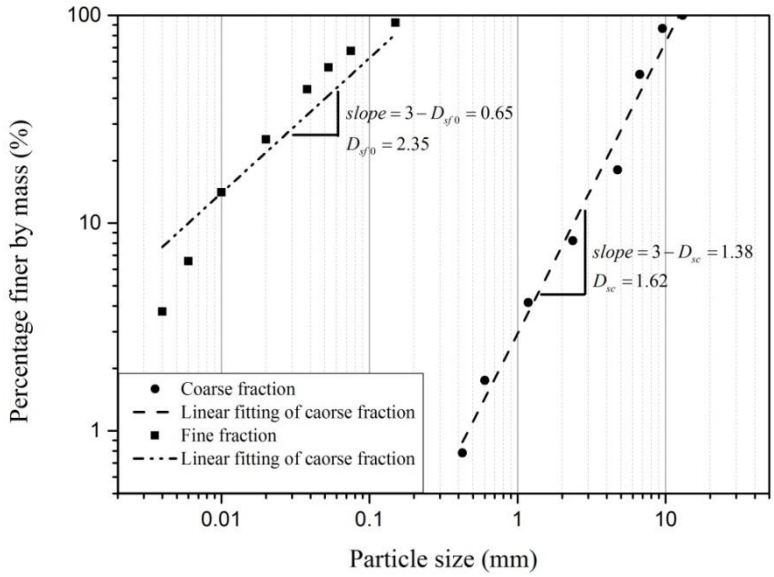

Figure 5-1 Particle size distributions of testing soil divided into finer and coarser fractions.

Figure 5-2 shows general particle size distribution curves of a gap-graded soil before and after internal erosion. The particle size distribution curve moves downwards from its initial position, due to the loss of fines from within the finer component due to internal erosion. The maximum and minimum particle sizes of the finer component do not change during erosion. Figures 5-3 and 5-4 show the rescaled particle size distributions of the finer component before and after internal erosion.

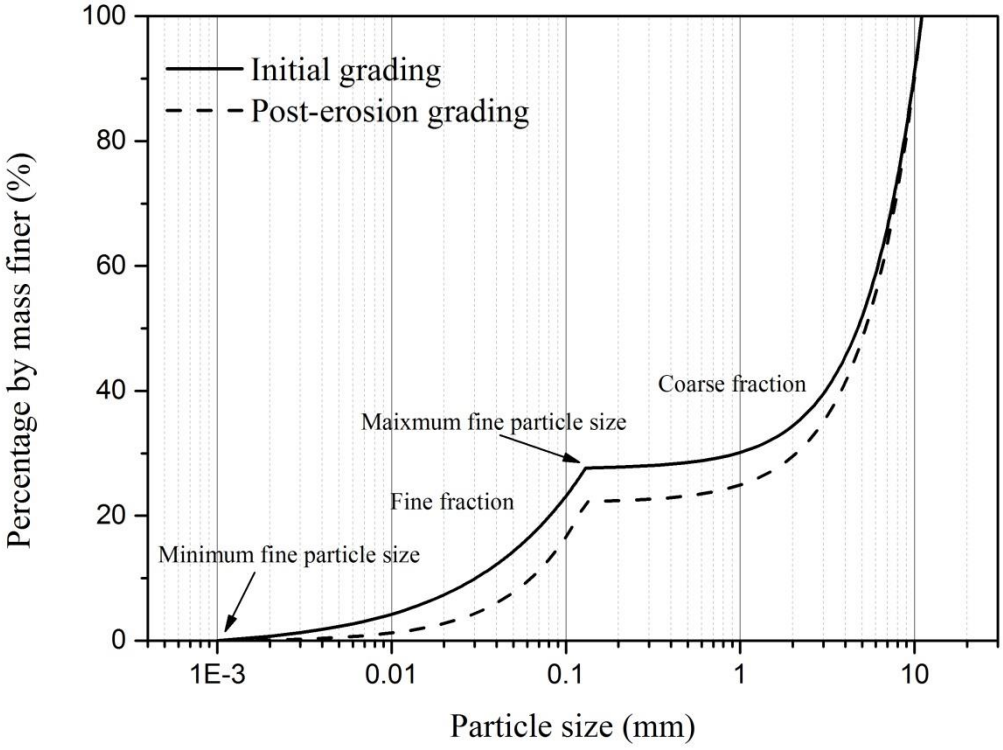

Figure 5-2 Schematic of particle size distribution curves of the soil before and after internal erosion.

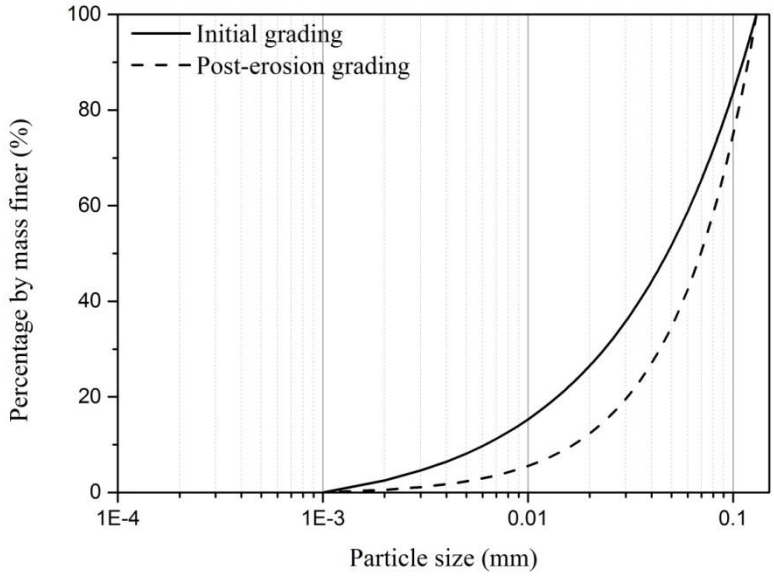

Figure 5-3 Rescaled particle size distribution curves of the finer component before and after erosion.

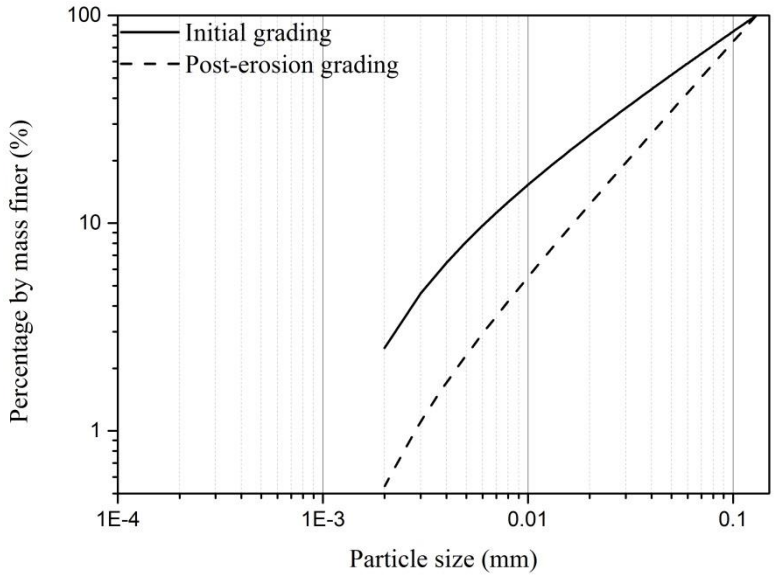

Figure 5-4 Rescaled particle size distribution curves of the finer component before and after erosion on a double logarithmic plane.

5.3.1 The link between fractal dimension and void ratio for well-graded soil

This section presents a mathematical method to calculate the void ratio for soil with a fractal particle size distribution (i.e., when well-graded) based on Russell (2010, 2011) and Russell and Buzzi (2012)'s formulations.

Consider a soil sample of total volume V, in which particles have a fractal particle size distribution. Each particle is denoted by order k, numbered upward from an order 0 for the smallest particle size. The first order particle has a size d_{sk}, which also represents the largest particle size. The subscript s indicates a solid particle. The total volume of all particles of order k is defined to be μV, where μ is the ratio between the volume of solid particles of order k. The value of μ must be smaller than 1. The total number of particles of order k is equal to $\mu V / (\Lambda d_{sk}^{3})$, where Λ is a geometric shape factor and is assumed to be constant for all particles. Then suppose the second-order $k-1$ of smaller particles have a size $d_{sk} / n^{1/3}$, where n is the ratio between individual particle volumes of successive orders and is a material constant. The total number of particles of order $k-1$ is defined to be $\mu p V$, where p is a material constant representing the ratio between total particle volumes of successive orders. The total number of particles of order $k-1$ is equal to $\mu n p V / (\Lambda d_{sk}^{3})$. The same procedure can be followed for all orders to create a fractal distribution of particle sizes, with results for the first three and ith orders presented in Table 5-2.

The total volume of solid particles from order k to 0 is:

$$V_s = \mu V (1 + p + p^2 + ...) \qquad (5\text{-}1)$$

which, since p must be less than 1 for convergence, gives the solution:

$$V_s = \frac{\mu V}{1-p} \qquad (5\text{-}2)$$

Table 5-2 Successive orders of particles and their geometrical properties

Order	k	$k-1$	$k-2$	…	i
Particle size	d_{sk}	$d_{sk}/n^{1/3}$	$d_{sk}/n^{2/3}$	…	$d_{sk}/n^{(k-i)/3}$
Volume of particle	μV	μpV	$\mu p^2 V$	…	$\mu p^{(k-i)} V$
Number of particles	$\mu V/(\Lambda d_{sk}^3)$	$\mu Vnp/(\Lambda d_{sk}^3)$	$\mu V(np)^2/(\Lambda d_{sk}^3)$	…	$\mu V(np)^{(k-i)}/(\Lambda d_{sk}^3)$

The void ratio e is then equal to:

$$e = \frac{V_v}{V_s} = \frac{V - V_s}{V_s} = \frac{1-p}{\mu} - 1 \qquad (5\text{-}3)$$

The total number of particles of size L larger than d_{si} (the particle size of order i) is then:

$$\begin{aligned} N_s(L > d_{si}) &= \frac{\mu V}{\Lambda d_{sk}{}^3}(1 + np + (np)^2 + ...) \\ &= \frac{\mu V (np)^{(k-i)}}{\Lambda d_{sk}{}^3}(1 + \frac{1}{np} + \frac{1}{(np)^2} + ...) \\ &= \frac{\mu V (np)^{(k-i)}}{\Lambda d_{sk}{}^3}(\frac{np}{np-1}) \end{aligned} \qquad (5\text{-}4)$$

For soil with a fractal dimension D_s for the particle sizes, $N(L > d_{si}) \propto d_{si}{}^{-D_s}$, so that:

$$\frac{N_s(L > d_{s(i-1)})}{N_s(L > d_{si})} = (\frac{d_{s(i-1)}}{d_{si}})^{-D_s} = (n^{-1/3})^{-D_s} = np \qquad (5\text{-}5)$$

this leads to the relationships between n, p and D_s:

$$D_s = 3(1 + \frac{\ln p}{\ln n}) \qquad (5\text{-}6)$$

which can be expressed in an alternative way:

$$p = n^{(D_s - 3)/3} \qquad (5\text{-}7)$$

By substituting $p = n^{(D_s-3)/3}$ into Equation (5-2):

$$V_s = \frac{\mu V}{1 - n^{(D_s-3)/3}} \qquad (5\text{-}8)$$

It follows that (from Equation (5-3)):

$$e = \frac{V_v}{V_s} = \frac{1 - n^{(D_s-3)/3}}{\mu} - 1 \qquad (5\text{-}9)$$

The incremental form for e becomes

$$\delta e = \frac{\partial e}{\partial D_s}\delta D_s + \frac{\partial e}{\partial \mu}\delta \mu \qquad (5\text{-}10)$$

Note that n is an assumed constant and μ and D_s may vary as erosion occurs. This is a simple mathematic link between the void ratio of soil with fractal particle size distribution and the fractal dimension of soil for when erosion occurs.

5.3.2 The link between fractal dimension and void ratio for gap-graded soil

The test soil considered here, which is a mixture of silt, sand, and gravel in different proportions, can be divided into a coarser component and finer component. Each component has a fractal particle size distribution. This section will link the fractal dimensions to the void ratio for the gap-graded soil.

Two sets of parameters D_s, μ, n, p and Λ are used; one for the finer fraction and one for the coarser fraction (Table 5-1).

By adopting similar derivations to those in Section 5.3.1, the volume of fine particles of the soil before erosion can be expressed as:

$$V_{sf0} = \frac{\mu_{f0} V_f}{1 - n_f^{(D_{sf0}-3)/3}} \qquad (5\text{-}11)$$

The finer particles are calculated within the void space around the coarser particles. Similarly, the volume of the coarser particles before erosion can be expressed as:

$$V_{sc} = \frac{\mu_c V}{1 - n_c^{(D_{sc}-3)/3}} \qquad (5\text{-}12)$$

It is assumed that the coarser particles are contained within the total volume of the soil, ie $V_c = V$.

The volume of fine particles after erosion is:

$$V_{sf1} = \frac{\mu_{f1} V_f}{1 - n_f^{(D_{sf1}-3)/3}} \qquad (5\text{-}13)$$

The volume of coarse particles does not change due to erosion.

The ratio between the volume of the fine particles and the total volume of all particles before erosion is:

$$R_{f0}=\frac{V_{sf0}}{V_{sc}+V_{sf0}}=\frac{\dfrac{\mu_{f0}V_f}{1-n_f^{(D_{sf0}-3)/3}}}{\dfrac{\mu_c V}{1-n_c^{(D_c-3)/3}}+\dfrac{\mu_{f0}V_f}{1-n_f^{(D_{sf0}-3)/3}}}=\frac{\dfrac{\mu_{f0}}{1-n_f^{(D_{sf0}-3)/3}}\cdot\dfrac{V_f}{V}}{\dfrac{\mu_c}{1-n_c^{(D_c-3)/3}}+\dfrac{\mu_{f0}}{1-n_f^{(D_{sf0}-3)/3}}\cdot\dfrac{V_f}{V}} \quad (5\text{-}14)$$

Similarly, the ratio of the volume of the fines and total particles after erosion is

$$R_{f1}=\frac{V_{sf1}}{V_{sc}+V_{sf1}}=\frac{\dfrac{\mu_{f1}V_f}{1-n_f^{(D_{sf1}-3)/3}}}{\dfrac{\mu_c V}{1-n_c^{(D_c-3)/3}}+\dfrac{\mu_{f1}V_f}{1-n_f^{(D_{sf1}-3)/3}}}=\frac{\dfrac{\mu_{f1}}{1-n_f^{(D_{sf1}-3)/3}}\cdot\dfrac{V_f}{V}}{\dfrac{\mu_c}{1-n_c^{(D_c-3)/3}}+\dfrac{\mu_{f1}}{1-n_f^{(D_{sf1}-3)/3}}\cdot\dfrac{V_f}{V}} \quad (5\text{-}15)$$

The overall volume of the soil is a sum of the volume of fine particles V_{sf}, volume of coarse particles V_{sc} and volume of voids V_v:

$$V=V_{sc}+V_{sf}+V_v \quad (5\text{-}16)$$

It is taken that V_f can be determined using:

$$V_f = V - V_{sc} = V_{sf} + V_v \qquad (5\text{-}17)$$

A so-called void ratio of the coarser fraction may be determined, assuming the volume of fine particles can be treated as part of voids around the coarser particles:

$$e_c = \frac{V - V_{sc}}{V_{sc}} = \frac{V_{sf} + V_v}{V_{sc}} \qquad (5\text{-}18)$$

and this is a constant during erosion since V_{sc} and V do not change. This may be rewritten as:

$$e_c = \frac{1 - n_c^{(D_{sc}-3)/3}}{\mu_c} - 1 \qquad (5\text{-}19)$$

The void ratio of the finer fraction before erosion is equal to:

$$e_{f0} = \frac{1 - n_f^{(D_{sf0}-3)/3}}{\mu_{f0}} - 1 \qquad (5\text{-}20)$$

and after erosion is equal to:

$$e_{f1} = \frac{1 - n_f^{(D_{sf1}-3)/3}}{\mu_{f1}} - 1 \qquad (5\text{-}21)$$

The global void ratio of the soil before erosion is:

$$e_0 = \frac{V_v}{V_{sf0} + V_{sc}} \qquad (5\text{-}22)$$

Substituting Equations (5-11) and (5-12) into the above expression leads to:

$$e_0 = \frac{V_v}{V_{sf0}+V_{sc}} = \frac{V-(V_{sf0}+V_{sc})}{V_{sf0}+V_{sc}} = \frac{V-\dfrac{\mu_{f0}V_f}{1-n_f^{(D_{sf0}-3)/3}}-\dfrac{\mu_c V}{1-n_c^{(D_{sc}-3)/3}}}{\dfrac{\mu_{f0}V_f}{1-n_f^{(D_{sf0}-3)/3}}+\dfrac{\mu_c V}{1-n_c^{(D_{sc}-3)/3}}}$$
$$= \frac{1-\dfrac{\mu_{f0}}{1-n_f^{(D_{sf0}-3)/3}}\cdot\dfrac{V_f}{V}-\dfrac{\mu_c}{1-n_c^{(D_{sc}-3)/3}}}{\dfrac{\mu_{f0}}{1-n_f^{(D_{sf0}-3)/3}}\cdot\dfrac{V_f}{V}+\dfrac{\mu_c}{1-n_c^{(D_{sc}-3)/3}}} \quad (5\text{-}23)$$

in which V_f/V is a constant when erosion occurs and is given by;

$$\frac{V_f}{V} = \frac{V-V_{sc}}{V} = 1-\frac{V_{sc}}{V} = 1-\frac{V_{sc}}{V_f+V_{sc}} = 1-\frac{1}{1+\dfrac{V_f}{V_{sc}}} = 1-\frac{1}{1+\dfrac{V_{sf}+V_v}{V_{sc}}}$$
$$= 1-\frac{1}{1+e_c} = \frac{e_c}{1+e_c} = \frac{\dfrac{1-n_c^{(D_{sc}-3)/3}}{\mu_c}-1}{\dfrac{1-n_c^{(D_{sc}-3)/3}}{\mu_c}} \quad (5\text{-}24)$$

Similarly, the global void ratio of the soil after erosion is:

$$e_{final} = \frac{1-\dfrac{\mu_{f1}}{1-n_f^{(D_{sf1}-3)/3}}\cdot\dfrac{V_f}{V}-\dfrac{\mu_c}{1-n_c^{(D_{sc}-3)/3}}}{\dfrac{\mu_{f1}}{1-n_f^{(D_{sf1}-3)/3}}\cdot\dfrac{V_f}{V}+\dfrac{\mu_c}{1-n_c^{(D_{sc}-3)/3}}} \quad (5\text{-}25)$$

More generally, for gap-graded soils, a direct link between fractal properties and the void ratio becomes:

$$e = \frac{1-\dfrac{\mu_f}{1-n_f^{(D_{sf}-3)/3}}\cdot\dfrac{V_f}{V}-\dfrac{\mu_c}{1-n_c^{(D_{sc}-3)/3}}}{\dfrac{\mu_f}{1-n_f^{(D_{sf}-3)/3}}\cdot\dfrac{V_f}{V}+\dfrac{\mu_c}{1-n_c^{(D_{sc}-3)/3}}} \quad (5\text{-}26)$$

where V_f / V is given in Equation (5-24). e depends on only two variables: D_{sf} and μ_f. In incremental form, e is expressed as:

$$\delta e = \frac{\partial e}{\partial D_s}\delta D_s + \frac{\partial e}{\partial \mu_f}\delta \mu_f \qquad (5\text{-}27)$$

which has the same form with Equation (5-10).

If μ_f is constant, or experiences negligible change, then the incremental form for e becomes much simpler:

$$\delta e = \frac{\partial e}{\partial D_s}\delta D_s \qquad (5\text{-}28)$$

Here it will be assumed that μ_f is constant for a soil at certain stress state. In other words, the total number of the largest particles which make up the finer fraction remains constant during erosion. It will be demonstrated later that this agrees well with the experimental observations.

5.4 THE CHANGE IN PARTICLE SIZE DISTRIBUTION DUE TO INTERNAL EROSION

The particle size distribution of a gap-graded soil subjected to internal erosion typically shift downwards from its original position due to the loss of particles from the finer component.

According to (Russell 2010), the particle size distribution of a well-graded soil with single fractal particle size distribution can be expressed as:

$$\%M(d_s < d) = 100\left(\frac{d_s^{3-D_s} - d_{s\min}^{3-D_s}}{d_{s\max}^{3-D_s} - d_{s\min}^{3-D_s}}\right) \qquad (5\text{-}29)$$

As we assumed in Section 5.3, internal erosion does not change the maximum and minimum particle sizes. The only variable is the fractal dimension D_s. Thus, the particle size distribution of soils subjected to internal erosion can be described by Equation (5-29) once the fractal dimension of soil subjected to internal erosion is obtained from sieving or hydrometer analysis.

According to Equation (2-8), the particle size distribution of gap-graded soil can be expressed as:

$$\begin{cases} 1-R_c\dfrac{d_{sc\max}^{3-D_{sc}}-d_{sc}^{3-D_{sc}}}{d_{sc\max}^{3-D_{sc}}-d_{sc\min}^{3-D_{sc}}} & \textit{Coarse fraction} \\ 1-R_c-(1-R_c)\dfrac{d_{sf\max}^{3-D_{sf}}-d_{sf}^{3-D_{sf}}}{d_{sf\max}^{3-D_{sf}}-d_{sf\min}^{3-D_{sf}}} & \textit{Fine Fraction} \end{cases} \qquad (5\text{-}30)$$

Here $R_c = 1-R_f$ (Equations (5-14) and (5-15)). The maximum and minimum particle sizes for both finer and coarser fractions, and the fractal dimension of the coarser fraction do not change according to assumptions made in Section 5.3. There are two variables in this circumstance: the fractal dimension of the finer fraction D_{sf} and the mass ratio of the coarser fraction to the total mass of soil R_c. The fractal dimension and mass ratio of the finer fraction can be obtained from sieving or hydrometer analysis or according to Equation (5-15).

An example of using the fractal characteristics to describe the particle size distribution of soils before and after internal erosion is shown in Figures 5-2, 5-3 and 5-4.

5.5 Validation with laboratory data

The theoretical derivations outlined in Sections 5.3 and 5.4 for the evolution of the void ratio and particle size distribution during suffusion are validated by comparing experimental data. The parameters used to fit the experimental data are listed in Table 5-3.

Table 5-3 Properties of particles of successive orders

Symbols	Finer component, before erosion	Coarser component, before erosion	Finer component, after erosion	Coarser component, after erosion
Maximum particle size (mm)	$d_{sf\max 0}$ =0.13	$d_{sc\max}$ =11	$d_{sf\max 1}$ =0.13	$d_{sc\max}$ =11
Minimum particle size (mm)	$d_{sf\min 0}$ =0.001	$d_{sc\min}$ =0.13	$d_{sf\min 1}$ =0.001	$d_{sc\min}$ =0.13
Fractal dimension	D_{sf0} =2.35	D_{sc} =1.62	D_{sf1} =2.20 after 8 liters; D_{sf1} =2.10 after 24 liters D_{sf1} =1.78 after 48 liters	D_{sc} =1.62
μ	μ_{f0} =0.069	μ_c =0.128, 50 kPa; μ_c =0.130, 100 kPa μ_c =0.133, 200 kPa	μ_{f1} =0.069, 50 kPa; μ_{f1} =0.070, 50 kPa; μ_{f1} =0.071, 50 kPa;	μ_c =0.128, 50 kPa; μ_c =0.130, 100 kPa μ_c =0.133, 200 kPa
n	n_f =2.03	n_c =1.76	n_f =2.03	n_c =1.76

5.5.1 Post-erosion particle size distributions

Figures 5-5, 5-6 and 5-7 show post-erosion particle size distributions of soil samples having undergone different amounts of internal erosion, along with grading curves using Equation (5-30). The experimental data represent the averages of measurements from samples having undergone a certain amount of internal erosion under a hydraulic gradient of 3.1.

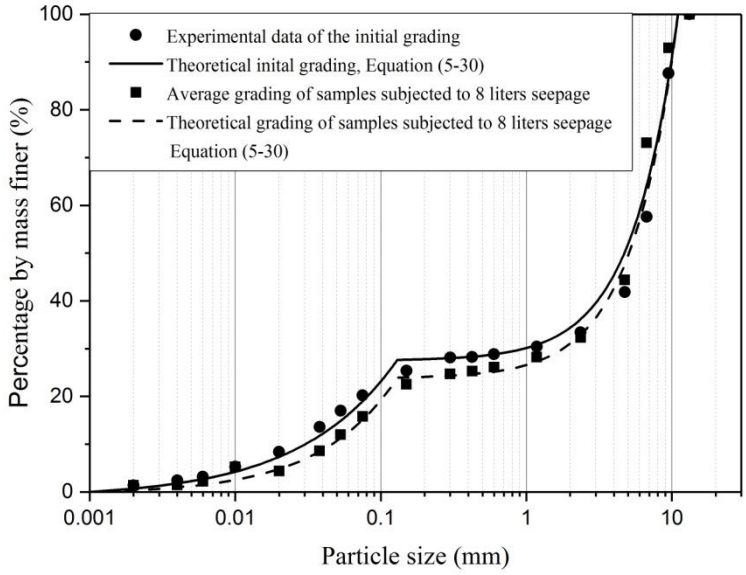

Figure 5-5 Theoretical and experimental particle size distribution for soils subjected to 8 liters seepage.

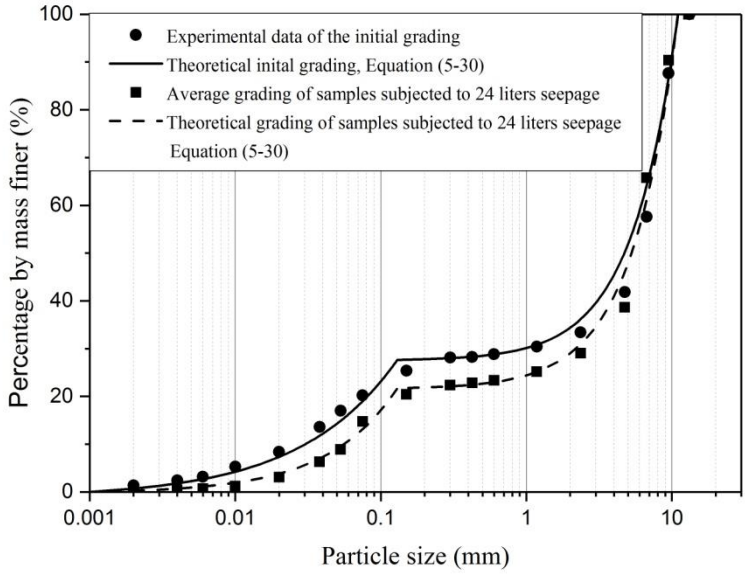

Figure 5-6 Theoretical and experimental particle size distribution for soils subjected to 24 liters seepage.

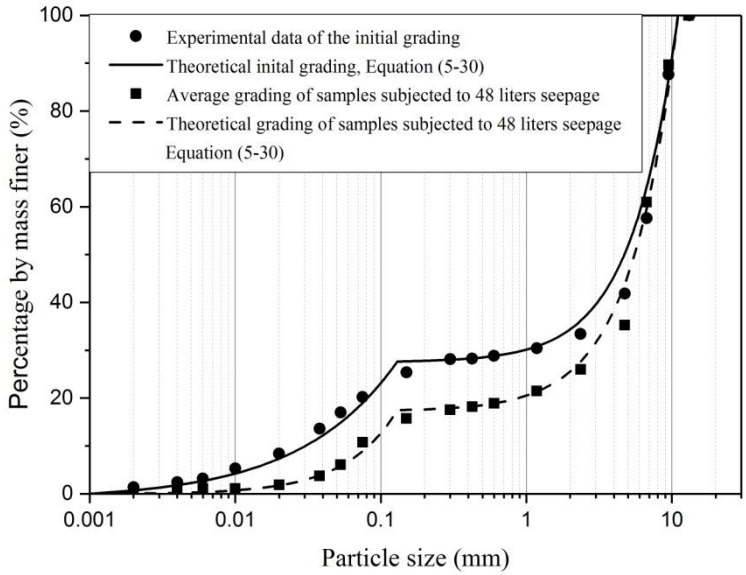

Figure 5-7 Theoretical and experimental particle size distribution for soils subjected to 48 liters seepage.

The fractal dimension of the finer component within soils having undergone 0, 8, 24 and 48 liters seepage erosion were 2.35, 2.2, 2.1, 1.78, respectively. It can be seen that the theoretical

grading curves fit well with the experimental data. The assumption that μ_f, $d_{sf\max}$ and $d_{sf\min}$ remain constants erosion occur are appropriate.

5.5.2 The evolution of void ratio due to internal erosion

Figures 5-8, 5-9 and 5-10 show the experimental and theoretical evolutions of the evolution of void ratio due to different amounts of internal erosion. The solid symbols represent the void ratio after consolidation and before erosion. The hollow symbols represent the void ratio after internal erosion, prior to the shearing. It can be seen that the void ratio increases as erosion occurs. A greater amount of internal erosion increases the void ratio more. The theoretical values fit well with the experiment data, providing further evidence that μ_f, $d_{sf\max}$ and $d_{sf\min}$ remain constants as erosion occurs.

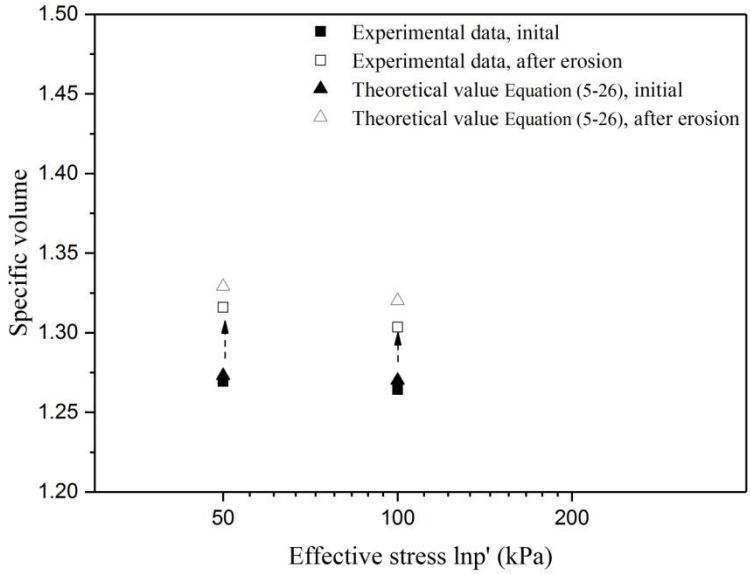

Figure 5-8 Evolution of void ratio for soils subjected to 8 liters seepage.

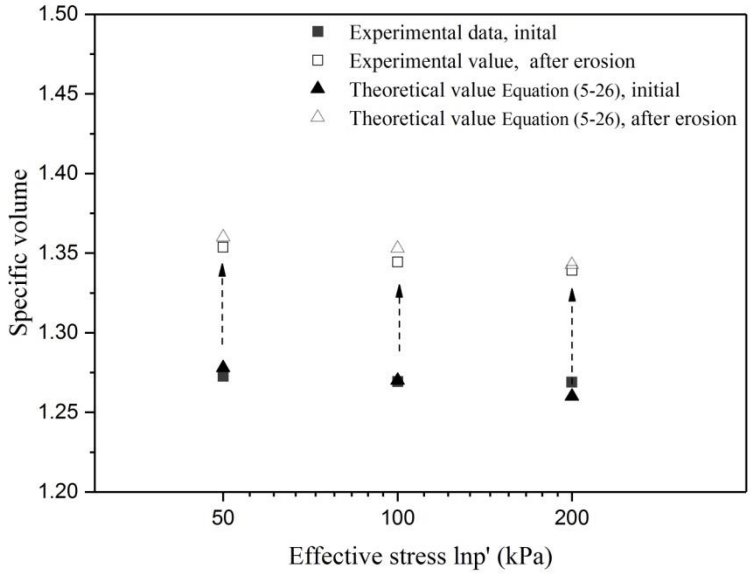

Figure 5-9 Evolution of void ratio for soils subjected to 24 liters seepage.

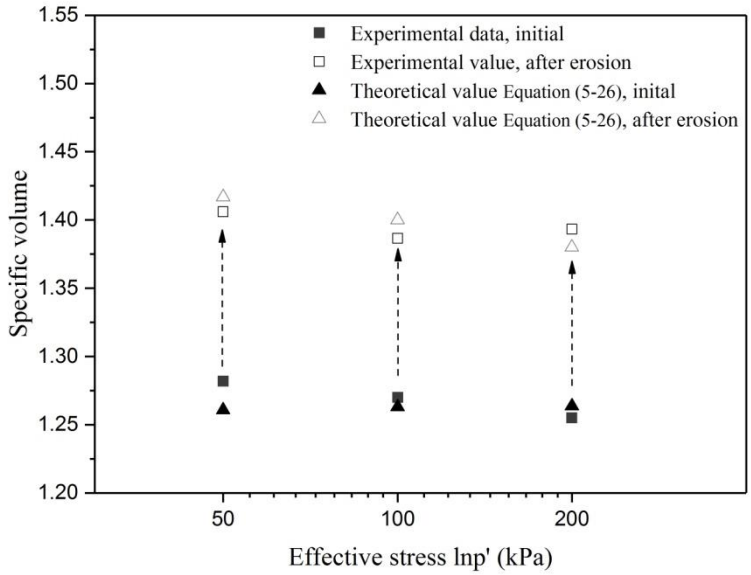

Figure 5-10 Evolution of void ratio for soils subjected to 48 liters seepage.

5.7 DISCUSSION AND CONCLUSION

This chapter focused on the evolution of void ratios of soils subjected to internal erosion using fractal theory.

A direct mathematical link between the fractal dimension and void ratio for soils with single or double fractal particle size distribution(s) was developed based on some practical and realistic assumptions.

In gap-graded soils different amounts of internal erosion cause the fractal dimension of the finer component of the particles to vary. The changing grading due to internal erosion may be expressed solely in terms of the change in fractal dimension. The change in void ratio can also be expressed in terms of this changing fractal dimension. The theoretical expectations fit well with experimental data.

CHAPTER 6 A CONSTITUTIVE MODEL FOR THE STRESS-STRAIN BEHAVIOR OF GAP-GRADED SOILS SUBJECTED TO INTERNAL EROSION

6.1 INTRODUCTION

This chapter outlines a constitutive model for the stress-strain behavior of gap-graded soils having undergone different amounts of internal erosion. The model incorporates microstructural characteristics through the fractal characteristics of the particle size distribution to simulate the macro-scale mechanical behavior.

The removal of fine particles due to suffusion has three main effects including creating a larger void space in soils, shifting the post-erosion particle size distribution downwards from its original position and changing the critical state of the soils. These effects have been described mathematically in Section 5.3, 5.4 and 5.5. The constitutive model Severn-Trent sand model (Gajo and Muir Wood 1999; Muir Wood and Belkheir 1994) is used here as a base. The effects of suffusion are captured through the critical state line and state parameter, which in turn capture the effects of the altered void ratio and particle size distribution.

The model is used to simulate the stress-strain behavior of a gap-graded cohesionless soil, with relevant results of laboratory tests detailed in Chapter 4.

6.2 THE CONSTITUTIVE MODEL FOR INTERNAL EROSION

6.2.1 Severn-Trent sand

Severn-Trent sand (Gajo and Muir Wood 1999) is an extended Mohr-Coulomb model which describes the mechanical behavior of soil with an unchanged grading. In it the critical state line

plays a central role to control the strength and dilatancy through the state parameter ψ (Been and Jefferies 1985). It provides a sound and simple base upon which a constitutive model that captures the effects of a changing grading, either through internal erosion (Muir Wood et al. 2010) or particle crushing (Kikumoto et al. 2010), can be developed.

The model contains four main elements. First, it is taken that there exists an asymptotic critical state for a soil in which indefinite shearing proceeds at a constant density and constant effective stress. The state parameter ψ is defined as the volumetric distance between the current specific volume v and the specific volume v_{cs} at the critical state or void ratio e at the same mean effective stress (Figure 6-1)：

$$\psi = v - v_{cs} \qquad (6\text{-}1)$$

Second, the available peak strength η_p of a soil is dependent on the state parameter (Figure 6-2):

$$\eta_p = M - k\psi \qquad (6\text{-}2)$$

where k is a soil constant and M is the critical state stress ratio. For triaxial compression on and $c' = 0$, M is related to the angle of shearing resistance $\phi_{cv}^{'}$:

$$M = \frac{6\sin\phi_{cv}^{'}}{3-\sin\phi_{cv}^{'}} \qquad (6\text{-}3)$$

the subscript cv indicates an association with the critical state.

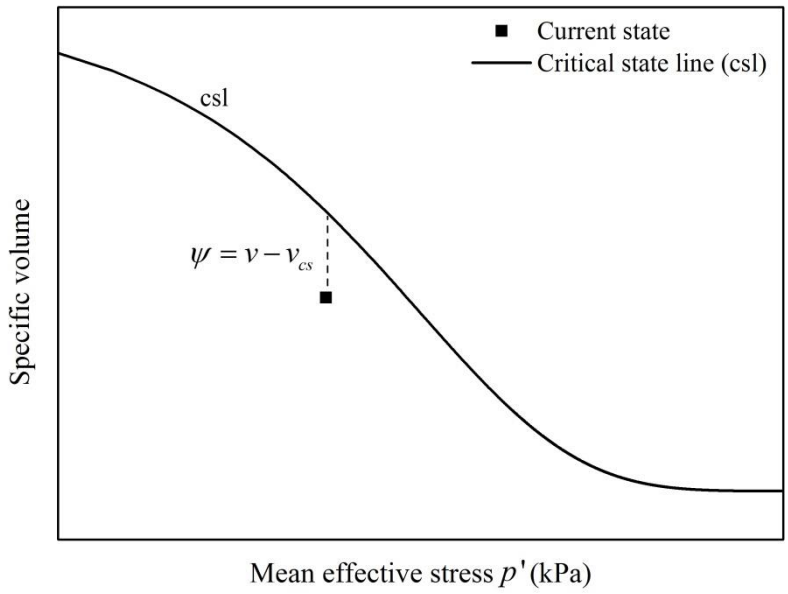

Figure 6-1 Definition of state parameter ψ .

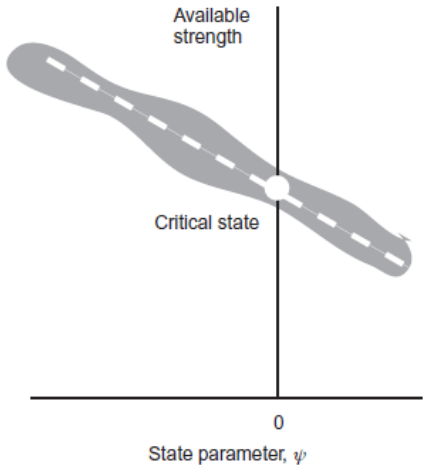

Figure 6-2 How the available strengths depend on the state parameter (Muir Wood et al. 2010).

Third, the soil is assumed to be a distortion hardening material so that the current mobilized stress ratio $\eta_y = q/p$ (which is akin to a mobilized strength) is linked only with the plastic

distortional strain ε_q^p . In order to describe the nonlinear degradation in stiffness, a simple hyperbolic relationship between η_y and ε_q^p is introduced (Figure 6-3):

$$\frac{\eta_y}{\eta_p} = \frac{\varepsilon_q^p}{a + \varepsilon_q^p} \tag{6-4}$$

Incrementally we have:

$$\delta\eta_y = \frac{(\eta_y - \eta_p)^2}{a\eta_p}\delta\varepsilon_q^p \tag{6-5}$$

or

$$\begin{pmatrix} \partial\eta_y / \partial\varepsilon_p^p \\ \partial\eta_y / \partial\varepsilon_q^p \end{pmatrix} = \begin{pmatrix} 0 \\ (\eta_p - \eta_y)^2 / a\eta_p \end{pmatrix} \tag{6-6}$$

where *a* is a soil constant which essentially scales the contribution of the plastic distortional strain (Muir Wood 2004)

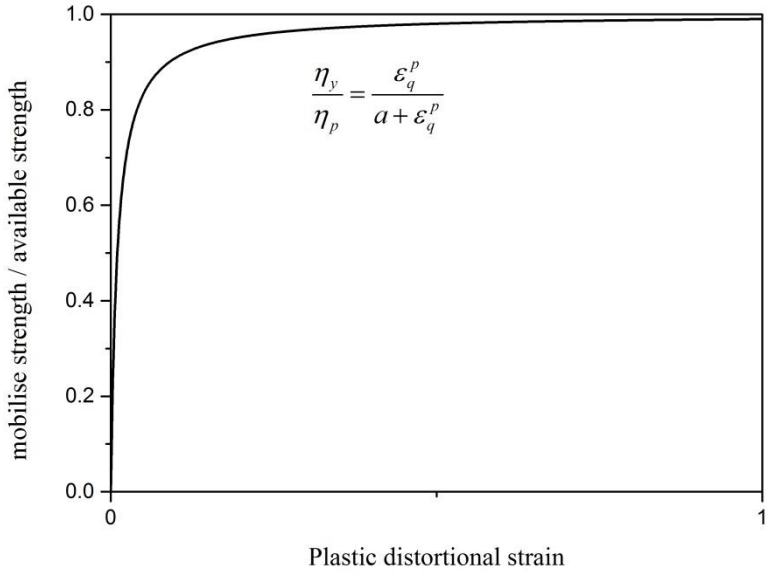

Figure 6-3 Distortion hardening law, after Kikumoto et al. (2010).

Fourth, the flow rule states that plastic distortion $\delta\varepsilon_q^p$ is accompanied by plastic volumetric strain $\delta\varepsilon_p^p$ according to a stress-dilatancy relationship which forces the volume towards the critical state whenever distortional straining occurs (as shown in Figure 6-4):

$$\frac{\delta\varepsilon_p^p}{\delta\varepsilon_q^p} = A[M(1+k_D\psi) - \eta_y] \quad (6\text{-}7)$$

where A and k_D are constitutive parameters. If $A=1$ and $k_D=0$, then the original Taylor (1948) and Cam-clay (Roscoe 1963) flow rule is obtained:

$$\frac{\delta\varepsilon_p^p}{\delta\varepsilon_q^p} = M - \eta_y \quad (6\text{-}8)$$

The above four ingredients of the Severn-Trent sand model ensure that the state of soil always, asymptotically, approaches critical state conditions during shearing. The critical state line plays a central role through the state parameter ψ. The current available peak strength, η_p, as described by Equation (6-2), can only be approached at infinite strain, where the state parameter ψ has approached zero and the available peak strength becomes equal to the critical state strength. Other features including kinematic hardening, a bounding surface and a changing grading can be readily incorporated to make the model able to predict plastic deformations during cycles of isotropic or anisotropic compression and unloading (Gajo and Muir Wood 1999) and the effects of crushing or erosion on soil's deformation behavior (Kikumoto et al. 2010; Muir Wood et al. 2010).

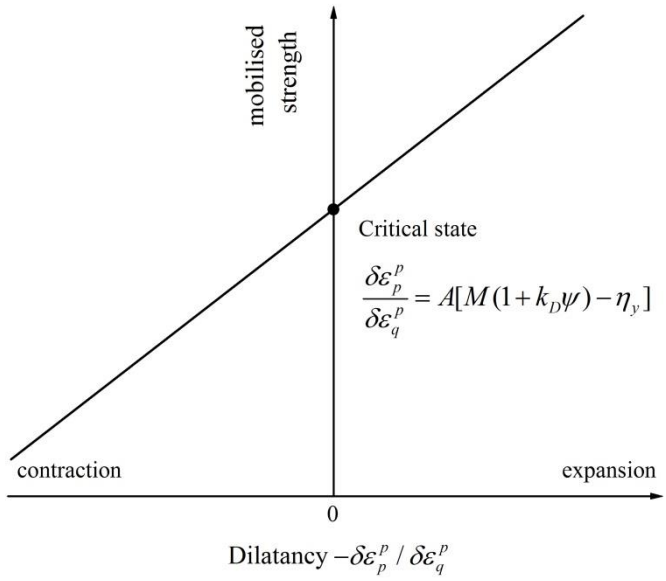

Figure 6-4 Stress dilatancy relationship, after Kikumoto et al. (2010).

6.2.2 Definition of a grading state index

A grading state index I_G was introduced by Muir Wood (2007) which evolves as internal erosion or particle crushing occur. It is a scalar parameter that may be used to link a changing particle size distribution to a soil's stress-strain behavior.

The grading state index of Muir Wood (2007) is defined as the ratio of the area under the current particle size distribution (ABC in Figure 6-5) and the area a limiting particle size distribution (ABD in Figure 6-5). It varies from 1 to 0 as the particle size distribution changes from a limiting grading to one for when particles are of a single size. The grading state index can be expressed as:

$$I_G \approx \frac{\ln(d_{\max} / d_{\min})}{2B} \qquad (6\text{-}9)$$

Here, B denotes the area ABD and a linear approximation is used for the area under the current particle size distribution. Also note that the area calculations are made by using $\ln(d)$, rather than d in a linear scale, as the horizontal length.

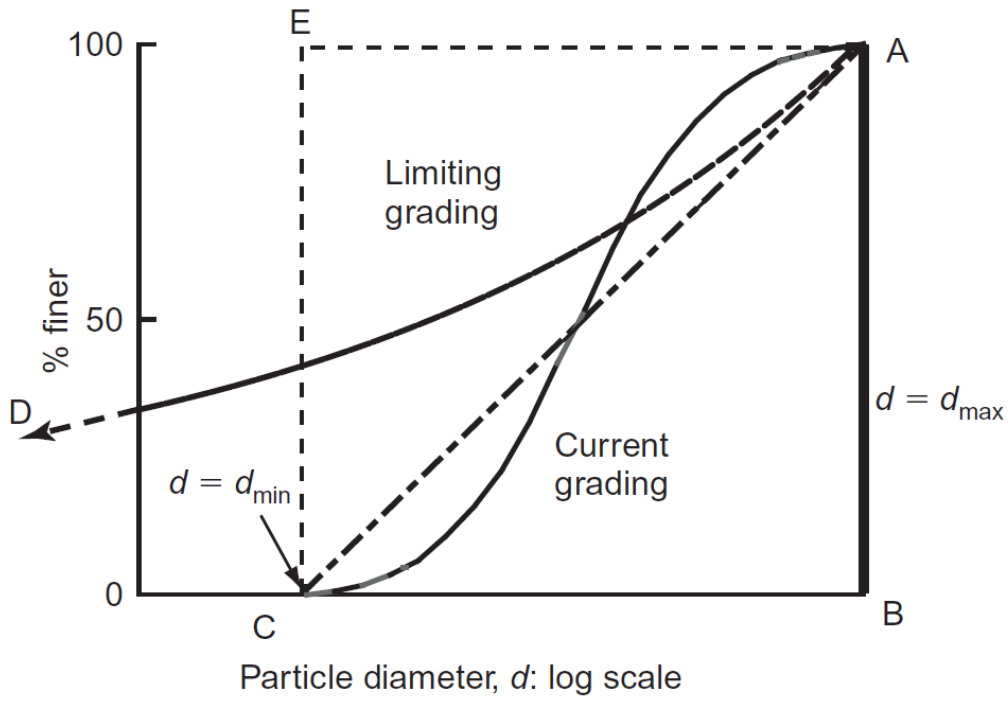

Figure 6-5 Definition of grading state index as the ratio of areas of ABC and ABD under the current and the limiting particle size distribution curves (Muir Wood et al. 2010).

.

This grading state index, including the linear approximation of the particle size distribution, is not able to capture the important dependency of internal erosion on the shape of the particle size distribution. For some particle size distributions the linear approximations provide very poor fits,, as shown in Figure 6-6. According to Equation (6-9), only the maximum and minimum particle sizes have important roles in estimating the value of the grading state index. This is concerning since the maximum and minimum particle sizes may not change during erosion, even though the shape of the particle size distribution does change, for example as shown in Figure 5-3.

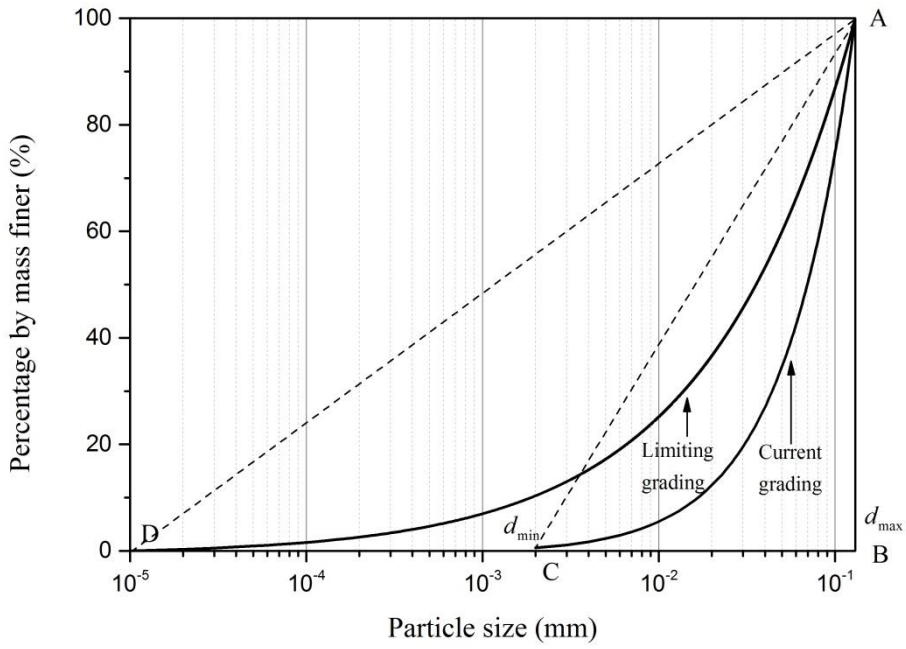

Figure 6-6 Definition of grading state index as the ratio of areas of ABC and ABD, poorly approximating areas under the current and the limiting particle size distributions according to Muir Wood (2007).

An alternative grading state index is defined here and will be used. It incorporates the closed areas under the limiting or current particle size distributions, which can be obtained by integration of Equation (5-35) for soils with single fractal particle size distribution or Equation (5-36) for soils with double fractal particle size distribution. The integrations are performed in terms of d, meaning the areas represent those under particle size distribution curves when d is plotted using a linear scale. Instead of using a linear approximation to estimate the area under the particle size distribution, integration of Equations (5-29) or (5-30) can be easily done. The maximum and minimum particle sizes are the integration limits and can be either fixed or allow to change.

Also, it is noted that the fine particles cannot be completely washed out by seepage and there must be a lower bound to the post-erosion particle size distribution. The area under that lower

bound distribution will be incorporated into the grading state index. It is reasonable to assume that the fractal dimension of finer fraction for this lower bound condition is equal to zero.

The new grading state index is defined as:

$$I_G = \frac{Area\ under\ current\ \ p.s.d - Area\ under\ lower\ bound\ \ p.s.d}{Area\ under\ inital\ \ p.s.d - Area\ under\ lower\ bound\ \ p.s.d} \qquad (6\text{-}10)$$

I_G reduces from 1 as erosion takes place. The lowest possible value of I_G is 0. For soils with a single fractal particle size distribution the grading state index can be expressed as:

$$I_G = \frac{\int_{d_{s\,\min}}^{d_{s\,\max}} 100\left(\frac{d_s^{3-D_{s1}} - d_{s\,\min}^{3-D_{s1}}}{d_{s\,\max}^{3-D_{s1}} - d_{s\,\min}^{3-D_{sf\,1}}}\right) d(d_s) - A_{lower}}{\int_{d_{s\,\min}}^{d_{s\,\max}} 100\left(\frac{d_s^{3-D_{s0}} - d_{s\,\min}^{3-D_{s0}}}{d_{s\,\max}^{3-D_{s0}} - d_{s\,\min}^{3-D_{s0}}}\right) d(d_s) - A_{lower}} \qquad (6\text{-}11)$$

in which,

$$A_{lower} = \int_{d_{s\,\min}}^{d_{s\,\max}} 100\frac{d_s^3 - d_{s\,\min}^3}{d_{s\,\max}^3 - d_{s\,\min}^3} d(d_s) \qquad (6\text{-}12)$$

where D_{s0} is the fractal dimension of soil with its initial particle size distribution, D_{s1} is the fractal dimension of soil having undergone a certain amount of internal erosion and $d_{s\,\min}$ and $d_{s\,\max}$ are the minimum and maximum particle size, d_s is the particle size.

For soils with a double fractal particle size distribution, the grading state index can be expressed as:

$$I_G \approx \frac{\int_{d_{sc\,\min}}^{d_{sc\,\max}} 100(1-R_{c0}\frac{d_{sc\,\max}^{3-D_{sc}}-d_{sc}^{3-D_{sc}}}{d_{sc\,\max}^{3-D_{sc}}-d_{sc\,\min}^{3-D_{sc}}})d(d_{sc})+\int_{d_{sf\,\min}}^{d_{sf\,\max}} 100(1-R_{c0}-(1-R_{c0})\frac{d_{sf\,\max}^{3-D_{sf\,0}}-d_{sf}^{3-D_{sf\,0}}}{d_{sf\,\max}^{3-D_{sf\,0}}-d_{sf\,\min}^{3-D_{sf\,0}}})d(d_{sf})-A_{lower}}{\int_{d_{sc\,\min}}^{d_{sc\,\max}} 100(1-R_{c1}\frac{d_{sc\,\max}^{3-D_{sc}}-d_{sc}^{3-D_{sc}}}{d_{sc\,\max}^{3-D_{sc}}-d_{sc\,\min}^{3-D_{sc}}})d(d_{sc})+\int_{d_{sf\,\min}}^{d_{sf\,\max}} 100(1-R_{c1}-(1-R_{c1})\frac{d_{sf\,\max}^{3-D_{sf\,1}}-d_{sf}^{3-D_{sf\,1}}}{d_{sf\,\max}^{3-D_{sf\,1}}-d_{sf\,\min}^{3-D_{sf\,1}}})d(d_{sf})-A_{lower}} \quad (6\text{-}13)$$

in which

$$A_{lower}=\int_{d_{sc\,\min}}^{d_{sc\,\max}} 100(1-R_{c\,\lim}\frac{d_{sc\,\max}^{3-D_{sc}}-d_{sc}^{3-D_{sc}}}{d_{sc\,\max}^{3-D_{sc}}-d_{sc\,\min}^{3-D_{sc}}})d(d_s)+\int_{d_{sf\,\min}}^{d_{sf\,\max}} 100(1-R_{c\,\lim}-(1-R_{c\,\lim})\frac{d_{sf\,\max}^{3}-d_{sf}^{3}}{d_{sf\,\max}^{3}-d_{sf\,\min}^{3}})d(d_s) \quad (6\text{-}14)$$

where $R_{c0}=1-R_{f0}$, $R_{c1}=1-R_{f1}$, R_{f0} and R_{f1} can be obtained from Equation (5-14) and (5-15), respectively; d_{sc} and d_{sf} are particle sizes within coarser and finer fractions, respectively; $R_{c\,\lim}$ the ratio between the volume of the coarse particles and the volume of all particles when the fractal dimension for the finer fraction is 0. Other notations are in accordance with Section 5.2.

Given that the maximum and minimum particle sizes of the finer fraction and coarser fraction, and the fractal dimension of the coarser fraction, are identical before and after suffusion, and R_c is dependent on the fractal dimension of finer fraction for a soil subjected to suffusion, the only variable is the fractal dimension of the finer fraction.

A graphical presentation of the upper bound and lower bound for the test soil, particle size distribution, and another particle size distribution which is evolving between these, are shown in Figures 6-7 and 6-8.

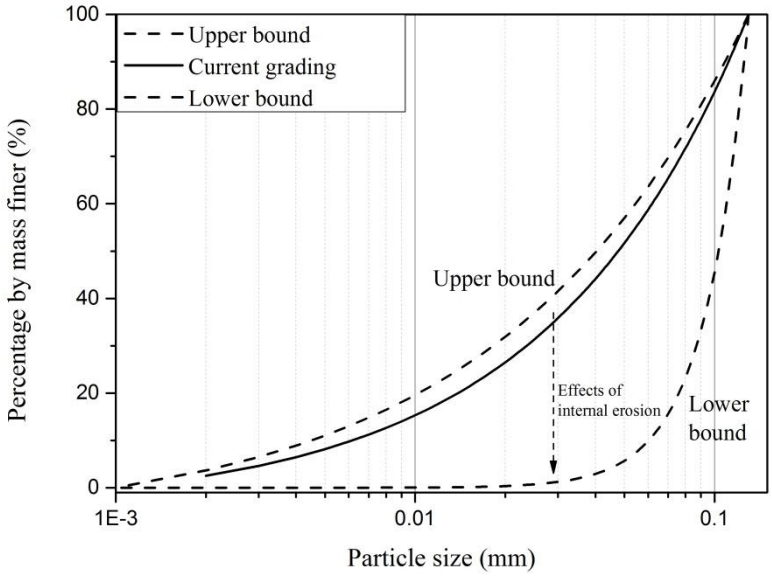

Figure 6-7 Upper and lower bound of the grading for the fine fraction of the testing soil..

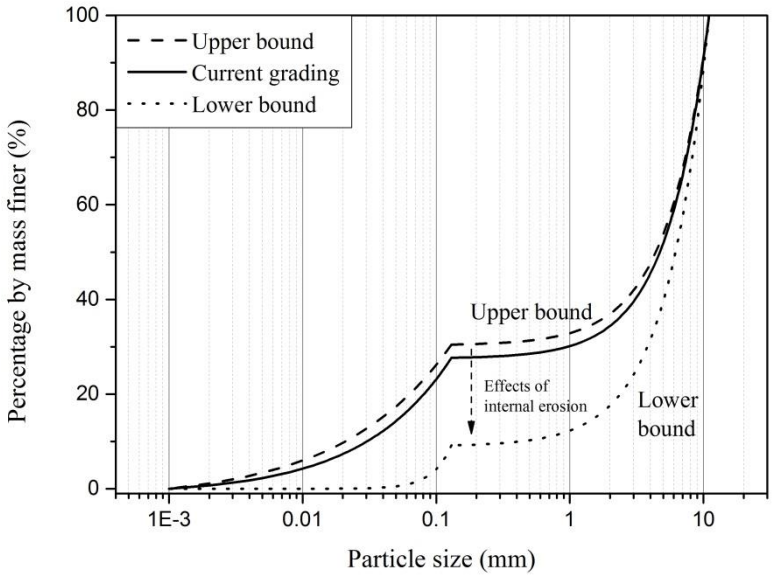

Figure 6-8 Upper and lower bound of particle size distributions.

6.2.3 The effects of internal erosion on the critical state line

Traditionally, the critical state line in the compression plane is defined as (Muir Wood 1990):

$$v_{cs} = \Gamma - \lambda \ln(p') \quad (6\text{-}15)$$

where Γ is the value of v_{cs} on the critical state line when $p' = 1$ kPa, and λ is its slope. The isotropic normal compression line is defined as:

$$v = N - \lambda \ln(p') \quad (6\text{-}16)$$

where N is the value of v when $p' = 1$ kPa. The elastic unloading and reloading line is then defined as:

$$v = v_k - \kappa \ln(p') \quad (6\text{-}17)$$

in which v_k is not a constant but depends on the current state.

Internal erosion creates voids and changes the grading of the soil. Creating voids results in an increase in the void ratio of soil, as discussed in Section 5.6.1. According to Muir Wood and Maeda (2007), the location of the critical state line moves upwards (as a result of removal of fine particles, such as internal erosion) or downwards (as a result of increasing in fine particles, such as particle crushing) in the compression plane as the grading changes. It is reasonable to assume that the slope of the critical state lines for soils subjected different amounts of internal erosion remains unaltered (Muir Wood and Maeda 2007). The effect of a changing grading on the critical state line has been mathematically described by Muir Wood et al. (2010) and Kikumoto et al. (2010) through a linear relationship between the maximum possible specific volume at the critical state and grading state index I_G through:

$$v_{cs}^{erosion} = \Gamma - \lambda \ln(p') - v_G I_G \quad (6\text{-}18)$$

where $v_{cs}^{erosion}$ is the specific volume at the critical state of a soil having undergone a certain amount of internal erosion, v_G controls the amount of vertical movement of the critical state line as the grading state index I_G changes (Muir Wood et al. 2010), I_G is the modified grading state index as it is discussed in section 6.2.2. When p' is constant:

$$\delta v_{cs}^{erosion} = -v_G \delta I_G \qquad (6\text{-}19)$$

δI_G is negative as the particle size distribution shift downwards from its original position due to internal erosion. Therefore, the critical state line moves upwards as a result of internal erosion.

Similarly, the isotropic normal compression line has the equation:

$$v = N - \lambda \ln(p') - v_G I_G \qquad (6\text{-}20)$$

The state parameter after erosion $\psi^{erosion}$ is then expressed as:

$$\begin{aligned} \psi^{erosion} &= v^{erosion} - v_{cs}^{erosion} = \psi + \delta e + v_G \delta I_G \\ &= v_0 - \Gamma + \lambda \ln(p') + \delta e + v_G \delta I_G \end{aligned} \qquad (6\text{-}21)$$

where $v^{erosion}$ is the specific void ratio after internal erosion and is equal to $v_0 + \delta e$. From Equations (5-26) and (5-24), we have:

$$\delta e = e_{final} - e_0 \qquad (6\text{-}22)$$

The change in state parameter for a constant p' is then expressed as:

$$\delta \psi^{erosion} = \delta e + v_G \delta I_G \qquad (6\text{-}23)$$

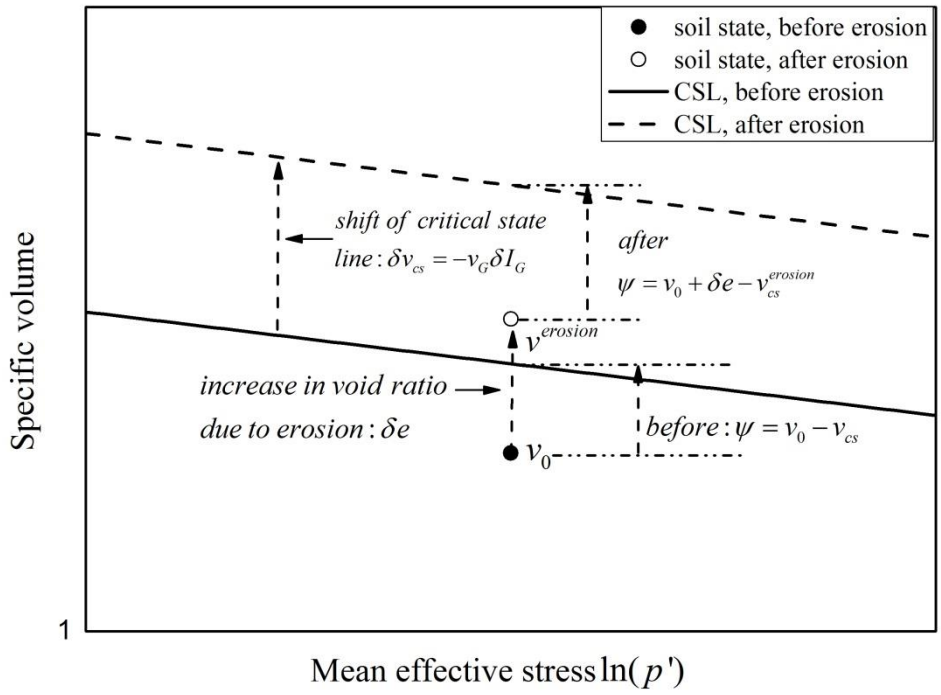

Figure 6-9 Schematic diagram of the shift of critical state and change in specific volume due to internal erosion.

Figure 6-9 shows a schematic diagram of the shift of the critical state and change in specific volume due to internal erosion. The solid black symbol represents the soil at a state with a specific volume lower than the corresponding specific volume at the critical state, indicating the density of the soil at this stress state is higher than the density of the soil at the critical state. The state parameter ψ is equal to $v_0 - v_{cs}$. After internal erosion, the specific volume increases by an amount δe while the critical state shifts upwards by an amount $-v_G \delta I_G$. The state parameter after internal erosion $\psi^{erosion}$ is then equal to $v^{erosion} - v_{cs}^{erosion} = v_0 + \delta e - v_{cs}^{erosion}$. The change in state parameter is $\delta e + v_G \delta I_G$.

According to Equation (6-2) we have:

$$\eta_p = M - k\psi = M - k(v^{erosion} - v_{cs}^{erosion}) \quad (6\text{-}24)$$

Substituting Equations (6-18), (6-19), (6-21) and $v = (v_0 + \delta e)(1 - \varepsilon_p)$ into Equation (6-24), we have:

$$\eta_p = M - k[((v_0 + \delta e) - \Gamma + \lambda \ln p_0^{'}) + (\lambda \ln \frac{p'}{p_0^{'}} - (v_0 + \delta e)\varepsilon_p^e) - v_0 \varepsilon_p^p] \quad (6\text{-}25)$$

The second term in square brackets can be neglected as the elastic volumetric strain roughly equals the volumetric change due to the mean effective stress change (Muir Wood 2004). Thus we have:

$$\eta_p = M - k[((v_0 + \delta e) - \Gamma + \lambda \ln p_0^{'}) - v_0 \varepsilon_p^p] \quad (6\text{-}26)$$

or the incremental form:

$$\delta\eta_p = -k\delta\psi \quad (6\text{-}27)$$

If $\delta e + v_G \delta I_G > 0$, i.e. the increase in the void ratio is greater than the vertical upward shift of the critical state line, then the state parameter ψ increases. Therefore, the available strength will fall and the stress ratio $\eta_y = \eta_p \varepsilon_q^p / (a + \varepsilon_q^p)$ will decrease as well.

Theoretically, it is possible that $\delta e + v_G \delta I_G \leq 0$. However, this may practically difficult to achieve as v_G controls the vertical movement of the critical state line as the grading state index shift from 1 to 0. Thus the calibration of v_G is crucial as an overestimation of it may lead to contrasting results and an underestimation of it may result in predicting an insufficient reduction in soil strength.

It is worth noting that δI_G is a variable and depends on the amount of erosion in different tests. However, it is a constant during shearing if no erosion is taking place.

6.2.4 Derivation of the constitutive model ingredients

The monotonic shearing of samples having undergone different amounts of internal erosion can be modelled using the Severn-Trent sand model. The effects of internal erosion, and the increasing void ratio and the vertical shifting of the critical state line may be considered. In this section, the constitutive relations and stiffness relations are presented.

Elastic properties

Conventional nonlinear isotropic elastic properties are assumed. Two stiffness properties increasing the bulk modulus K and shear modulus G are used here. It follows that:

$$\begin{pmatrix} \delta p' \\ \delta q \end{pmatrix} = \begin{pmatrix} K & 0 \\ 0 & 3G \end{pmatrix} \begin{pmatrix} \delta \varepsilon_p^e \\ \delta \varepsilon_q^e \end{pmatrix} = \mathbf{D} \delta \boldsymbol{\varepsilon}^e \qquad (6\text{-}28)$$

where $\mathbf{D}$ is the isotropic elastic stiffness matrix.

Comparing Equations (6-17) and (6-28), the stress level dependency of the elastic stiffness leads to a definition for the bulk modulus K:

$$K = \frac{vp'}{\kappa} \qquad (6\text{-}29)$$

The elastic shear modulus G is then derived by assuming a constant value for Poisson's ratio ν:

$$G = \frac{3(1-2\nu)K}{2(1+\nu)} \qquad (6\text{-}30)$$

Yield criterion

The yield criterion is now written as (Muir Wood 2014):

$$f(\boldsymbol{\sigma},\chi) = f(p',q,\eta_y) = q - \eta_y p' \qquad (6\text{-}31)$$

where $\chi = n_y$ and is the current size of the yield locus, as shown in Figure 6-10; $\boldsymbol{\sigma} = \begin{bmatrix} p' & q \end{bmatrix}^T$, the superscript T indicates the transpose of the matrix. The yield locus differs from the failure locus. η_y is approaches η_p as hardening proceeds. The elastic, elastic-plastic and inaccessible regions in the stress plane are indicated in Figure 6-10.

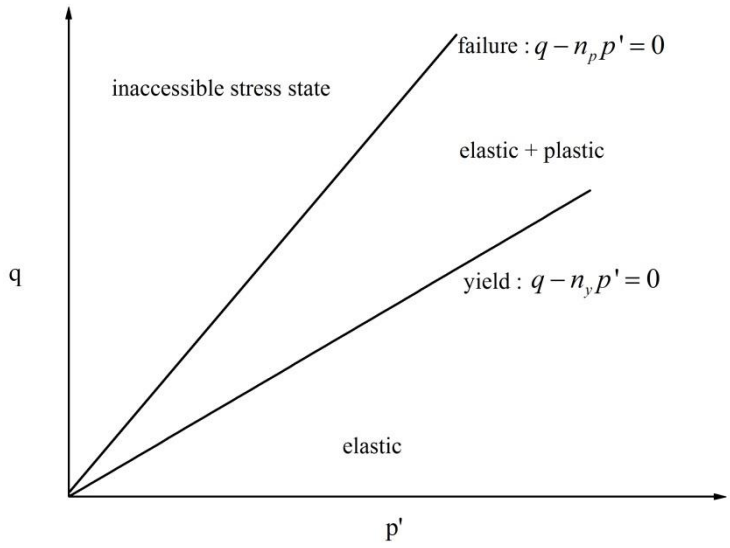

Figure 6-10 Yield locus and failure locus.

From the consistency condition, which states that the plastic strain increment $\delta\varepsilon^p$ occurs only when the stress state remains on the yield surface, it follows that:

$$f(\boldsymbol{\sigma},\eta_y)=0;\ \delta f=\frac{\partial f}{\partial \boldsymbol{\sigma}}\delta\boldsymbol{\sigma}+\frac{\partial f}{\partial \eta_y}\delta\eta_y=0 \qquad (6\text{-}32)$$

Combining Equations (6-31) and (6-32), we have:

$$\frac{\partial f}{\partial \boldsymbol{\sigma}}=\begin{bmatrix}\dfrac{\partial f}{\partial p'}\\ \dfrac{\partial f}{\partial q}\end{bmatrix}=\begin{bmatrix}-\eta_y\\ 1\end{bmatrix} \qquad (6\text{-}33)$$

Flow rule

The flow rule is introduced as per Equation (6-7). Conventionally, soils have a plastic potential function of the general form:

$$g(\boldsymbol{\sigma})=g(p',q)=0 \qquad (6\text{-}34)$$

The plastic strain increments are obtained using a vector normal to the plastic potential function at the current stress state. According to Equation (6-7), we have:

$$\delta\boldsymbol{\varepsilon}^p=\begin{pmatrix}\delta\varepsilon_p^p\\ \delta\varepsilon_p^p\end{pmatrix}=\mu\begin{pmatrix}\dfrac{\partial g}{\partial p'}\\ \dfrac{\partial g}{\partial q}\end{pmatrix}=\mu\begin{pmatrix}A[M(1+k_D\psi)-\eta_y]\\ 1\end{pmatrix} \qquad (6\text{-}35)$$

in which μ is a plastic multiplier.

Hardening rule

From Equations (6-4) and (6-26), the hardening rule becomes；

$$\frac{\partial \eta_y}{\partial \boldsymbol{\varepsilon}^p} = \begin{pmatrix} \frac{\partial \eta_y}{\partial \varepsilon_p^p} \\ \frac{\partial \eta_y}{\partial \varepsilon_q^p} \end{pmatrix} = \begin{pmatrix} \frac{\partial \eta_y}{\partial \eta_p}\frac{\partial \eta_p}{\varepsilon_p^p} \\ \frac{\partial \eta_y}{\varepsilon_q^p} \end{pmatrix} = \begin{pmatrix} \frac{\eta_y}{\eta_p} k(v_0 + \delta e) \\ \frac{(\eta_p - \eta_y)^2}{a\eta_p} \end{pmatrix} \quad (6\text{-}36)$$

Stress-strain relationship

According to Muir Wood (2014), the general form of the relationship between stress increments and strain increments is:

$$\delta\boldsymbol{\sigma} = \left[\mathbf{D} - \frac{\mathbf{D}\frac{\partial g}{\partial \boldsymbol{\sigma}}\frac{\partial f}{\partial \boldsymbol{\sigma}}^T \mathbf{D}}{\frac{\partial f}{\partial \boldsymbol{\sigma}}^T \mathbf{D}\frac{\partial g}{\partial \boldsymbol{\sigma}} + H} \right] \delta\boldsymbol{\varepsilon} = \mathbf{D}^{ep}\delta\boldsymbol{\varepsilon} \quad (6\text{-}37)$$

and H is given by:

$$H = -\frac{\partial f}{\partial \eta_y}\frac{\partial \eta_y}{\partial \boldsymbol{\varepsilon}^p}\frac{\partial g}{\partial \boldsymbol{\sigma}} \quad (6\text{-}38)$$

Substituting Equations (6-6), (6-33), (6-35) and (6-36) into Equations (6-37) and (6-38) gives the elastic-plastic stress-strain matrix:

$$\delta\boldsymbol{\sigma} = \left[\mathbf{D} - \frac{\begin{bmatrix} -AK^2\eta_y(M(1+k_D\psi) - \eta_y) & 3GKA(M(1+k_D\psi) - \eta_y) \\ -3GK\eta_y & 9G^2 \end{bmatrix}}{3G - AK\eta_y(M(1+k_D\psi) - \eta_y) + p'\left(\frac{Ak(v_0 + \delta e)\eta_y(M(1+k_D\psi) - \eta_y)}{\eta_p} + \frac{(\eta_p - \eta_y)^2}{a\eta_p} \right)} \right] \delta\boldsymbol{\varepsilon} \quad (6\text{-}39)$$

Note that the state parameter ψ is calculated according to Equation (6-21). The above equation can be written as $\delta\boldsymbol{\sigma} = \mathbf{D}^{ep}\delta\boldsymbol{\varepsilon}$.

6.3 CALIBRATION AND SIMULATION

This section presents the calibration and simulation of the Severn-Trent sand model extended to account for internal erosion, using experimental results which were detailed in Chapter 4. The predictive capabilities of the model for internal erosion are illustrated by its ability to closely simulate the stress-strain behavior of a soil having undergone varying amounts of internal erosion at different effective stresses.

The choice of model constants through calibration is detailed in Section 6.3.1. The comparisons between model simulations and test results are then given in Section 6.3.2.

6.3.1 Calibration

The triaxial compression tests on samples with homogeneous post-erosion particle size distribution results are used to obtain the critical state lines. Most tests were carried out to about $\varepsilon_q = 0.2$ to reach conditions close to the critical state. The stress trajectories are shown as short dash lines in the compression plane in Figure 6-11, where an open circle represents the initial conditions for samples without internal erosion, a solid circle represents the end of the drained compression tests on samples without internal erosion, an open square represents the initial conditions for samples having undergone 8 liters of seepage erosion, a solid square represents the end of tests on samples having undergone 8 liters of seepage erosion, a hollow triangle represents the initial conditions for samples having undergone 24 liters of seepage erosion, a solid triangle represents the end of tests on samples having undergone 24 liters of seepage erosion, a hollow five-point star represents the initial conditions for samples having undergone 48 liters of seepage erosion, a solid five-point star represents the end of tests on samples having undergone 48 liters of seepage erosion. The solid symbols indicating the ends of tests were regarded to be close to critical states as the stress ratios and volumetric strains had approached constant values at the large distortion strains.

It is convenient to employ linear relationships to fit the critical state lines for the range of applied effective stresses. For soils without internal erosion, $\Gamma = 1.62$ and $\lambda = 0.069$. The slope of the critical state lines, whatever the fractal dimension of the finer fractions, is assumed to be a constant. According to Figure 6-11, the vertical separation of critical state lines, when D_{sf} changes from 2.35 to 1.78 (and the I_G changes from 1 to 0.455) is about 0.15. A factor of 2 is applied to estimate the v_G, thus $v_G = 0.3$.

Combinations of the mean effective stress p', the fractal dimension of the finer components D_s and specific volume at critical state v can be plotted in the three-dimensional space, as shown in Figure 6-12.

Other microstructural parameters of the soil particles remain the same as erosion occurs, as listed in Table 5-3. Other constitutive parameters are listed in Table 6-1.

The effects of internal erosion and the changing grading on friction are not significant (Muir Wood and Maeda 2007). Thus the friction angle at the critical state is assumed to be a constant throughout. The effects of internal erosion and changing grading on elastic properties is unclear. A constant κ is assumed in this study, whatever the amounts of erosion.

The parameters listed in Table 6-1 were deduced through a trial and error and global optimization procedure.

Table 6-1 Constitutive parameters

parameter	value	description
D_{sf}	2.35 for 0 liters of erosion, 2.2 for 8 liters of erosion, 2.1 for 24 liters of erosion, 1.78 for 48 liters of erosion	fractal dimension of fine fractions
ϕ_{cv}	42°	angle of shearing resistance ϕ_{cv}
a	0.005	soil constant which essentially scales the plastic strain
A	1.8	constitutive parameter in flow rule
k_D	-0.8	constitutive parameter in flow rule
ν	0.3	Poisson' ratio
k	8	soil constant, the slope of state parameter versus available strength
κ	0.003	slope of unloading-reloading line

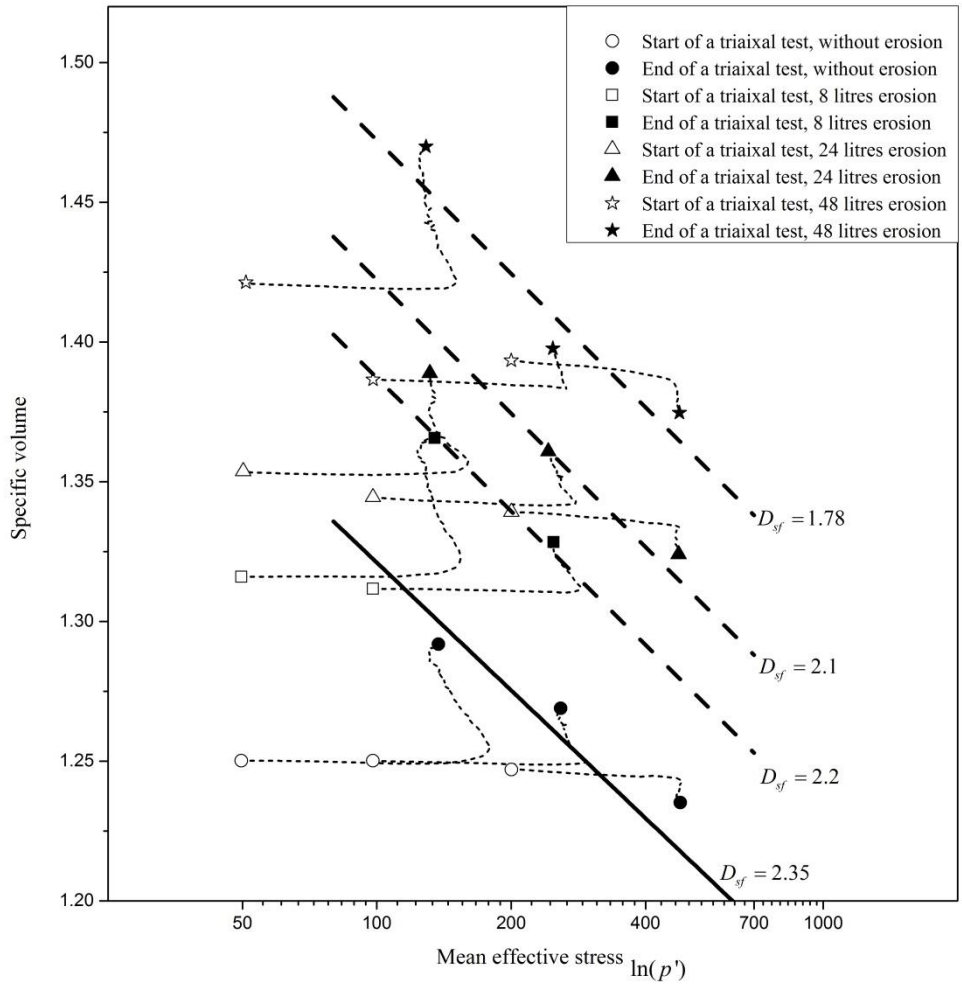

Figure 6-11 Triaxial test results and critical state lines.

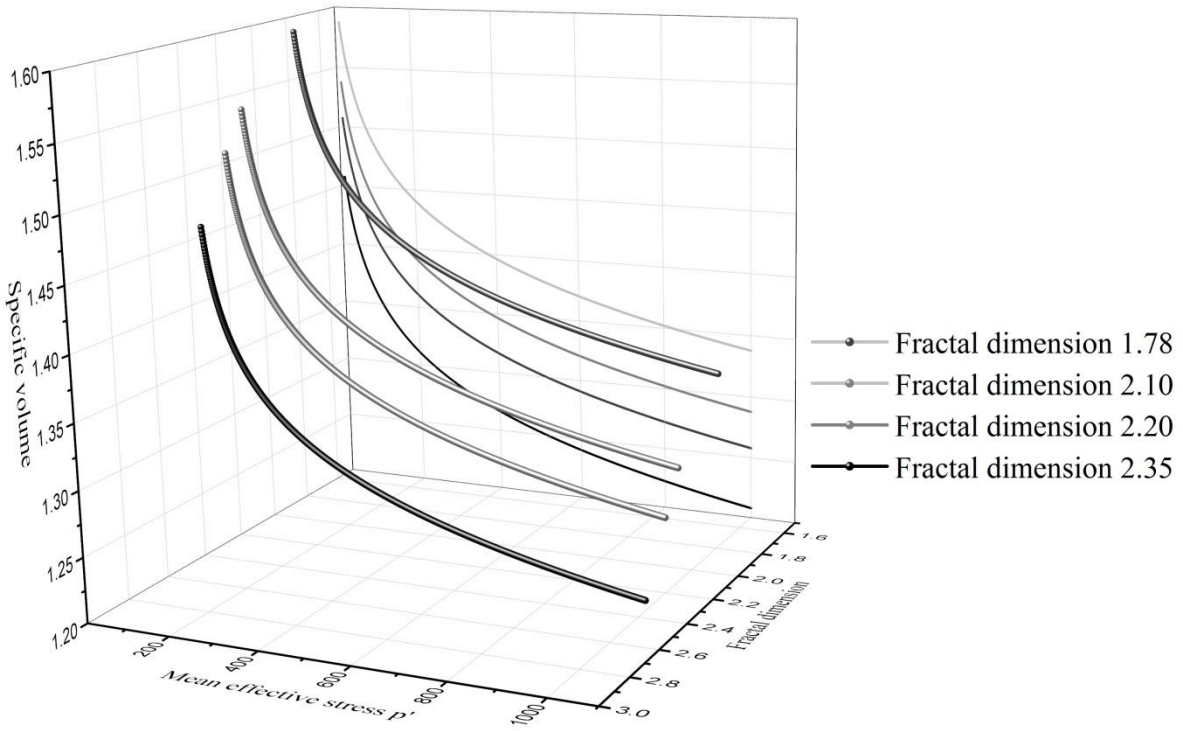

Figure 6-12 Critical state lines for different fractal dimensions of finer components.

6.3.2 Simulations of triaxial test results for soils without erosion

Figures 6-13 to 6-15 present the conventional drained triaxial test results and model simulations in $\eta_y \sim \varepsilon_q$ and $\varepsilon_p \sim \varepsilon_q$ planes. In the $\eta_y \sim \varepsilon_q$ plane, the solid line indicates variation in stress ratio, the dashed line indicates variation in current peak strength, the circles indicate experimental results. In the $\varepsilon_p \sim \varepsilon_q$, the dashed line indicates model simulation and the circles indicate experimental results. The tests were conducted at effective confining stresses of 50, 100 and 200 kPa, respectively. The specific volume before shearing were 1.256 (50 kPa), 1.253 (100kPa), 1.247 (200 kPa), respectively. Strain-softening and dilative responses were observed for 50 and 100 kPa, while a strain-hardening and contractive response was observed for 200 kPa. Specifically, for GG14 and GG18, with the effective confining stresses of 50 and 100 kPa,

respectively, hardening occurs rapidly up to a peak in the stress ratio, accompanied by initial volumetric contraction at small strains followed by volumetric expansion. The stress ratios after the peak gradually reduced towards an asymptotic line as the soils approached the critical state at large strains. For sample GG16, the stress ratio increased rapidly at small strains, then increased more slowly once the ε_q exceeded 0.015, as the soil approached the critical state.

Despite a few local variations, the model simulations fit well with the experimental data well.

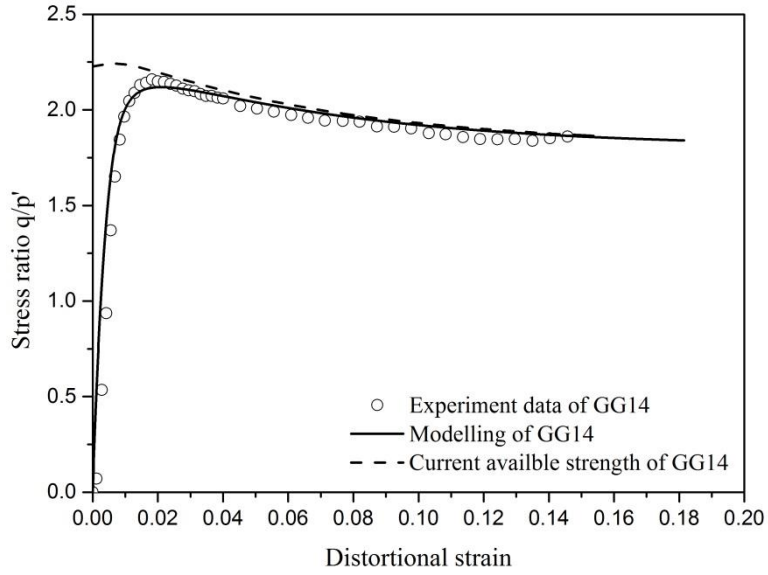

(a)

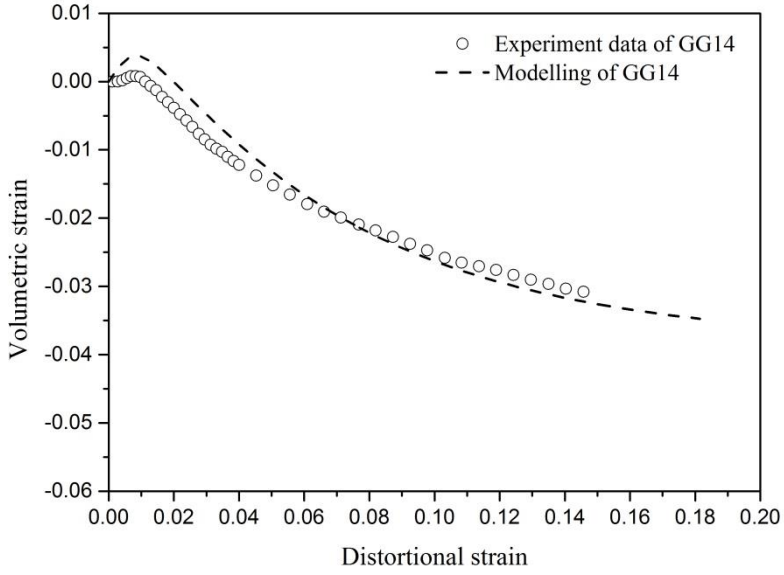

(b)

Figure 6-13 Triaxial compression test on a sample without erosion at an effective confining pressure of 50 kPa. (a) stress-strain response (b) volumetric strain response.

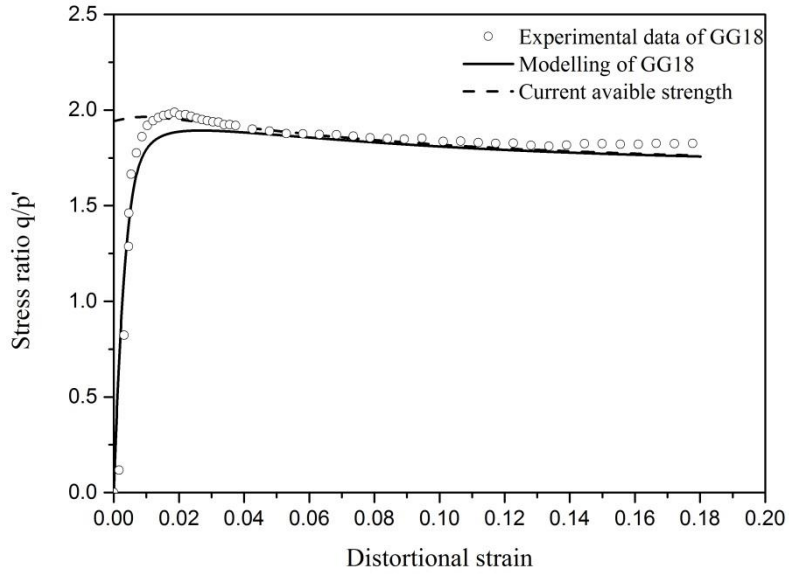

(a)

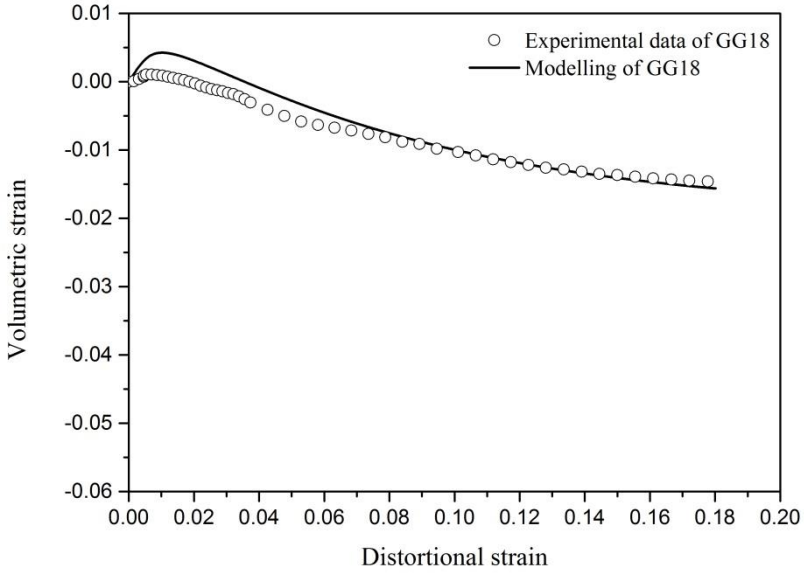

(b)

Figure 6-14 Triaxial compression test on a sample without erosion at an effective confining pressure of 100 kPa. (a) stress-strain response (b) volumetric strain response.

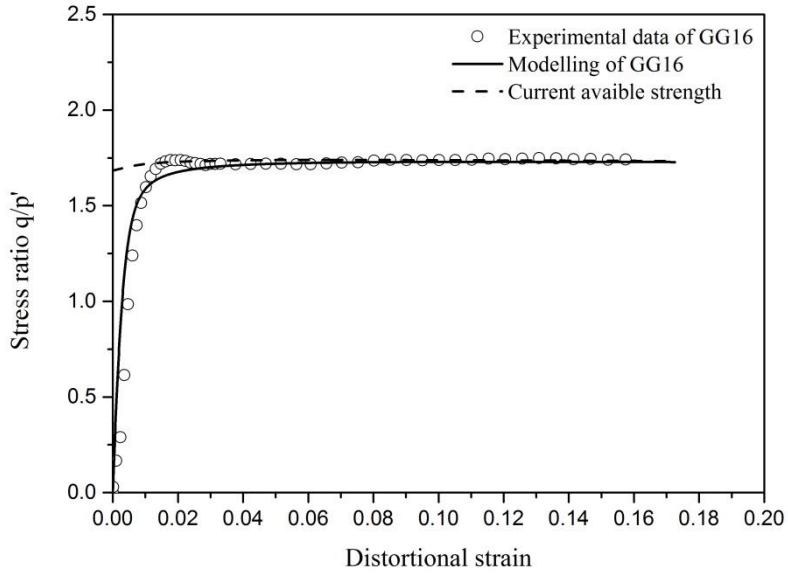

(a)

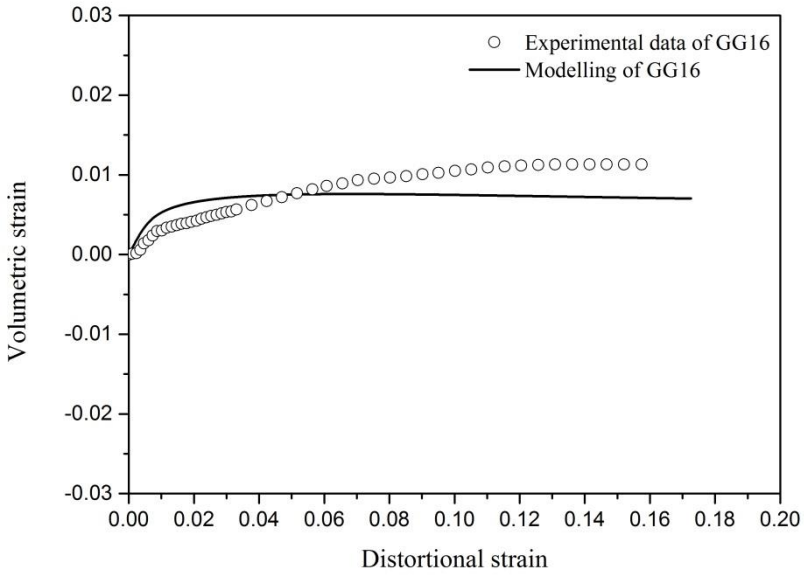

(b)

Figure 6-15 Triaxial compression a test on sample without erosion at an effective confining pressure of 200 kPa. (a) stress-strain response (b) volumetric strain response.

6.3.3 Simulations of triaxial tests for soils subjected to 8 liters of seepage to cause erosion

Figure 6-16 and Figure 6-17 present the results of drained triaxial tests on samples having undergone 8 liters of seepage and model simulations in $\eta_y \sim \varepsilon_q$ and $\varepsilon_p \sim \varepsilon_q$ planes. In the $\eta_y \sim \varepsilon_q$ plane, the solid line indicates variation in stress ratio, the dashed line indicates variation in current peak strength, the circles indicate experimental results. In the $\varepsilon_p \sim \varepsilon_q$ plane, the dashed line indicates model simulation and the circles indicate experimental results. The tests were conducted at effective stresses of 50 and 100 kPa, respectively. The specific volume before shearing were 1.316 (50 kPa) and 1.311 (100kPa), respectively. It is assumed that all samples have same fractal dimension of the finer fraction, $D_{sf} = 2.20$. The model simulations fit the experimental data well.

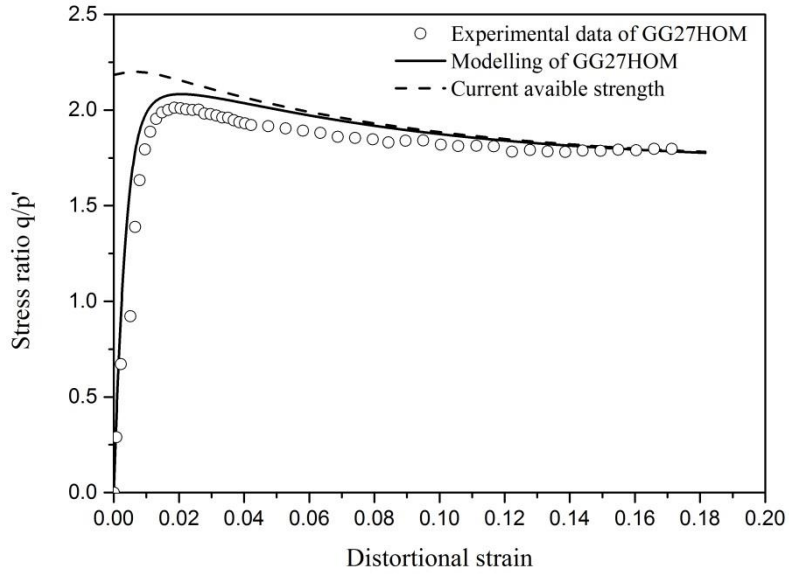

(a)

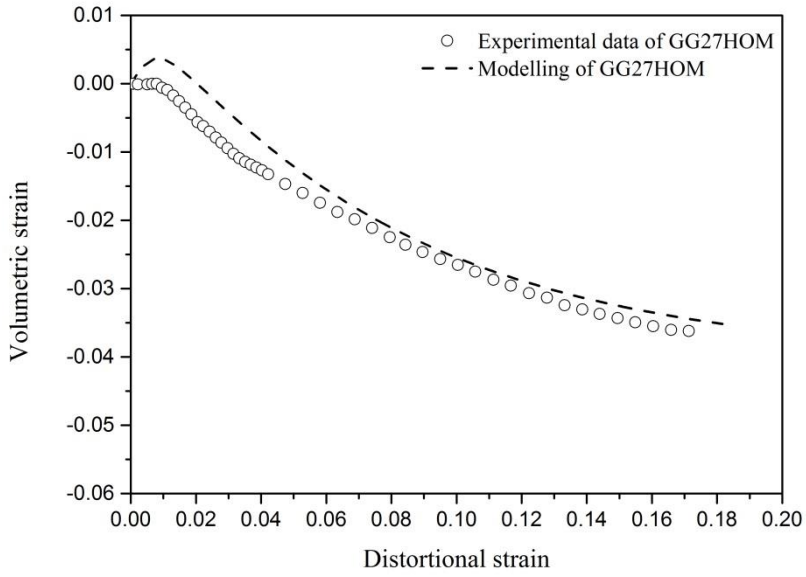

(b)

Figure 6-16 Triaxial compression test on a sample subjected to 8 litres of seepage to cause erosion at an effective confining pressure of 50 kPa. (a) stress-strain response (b) volumetric strain response.

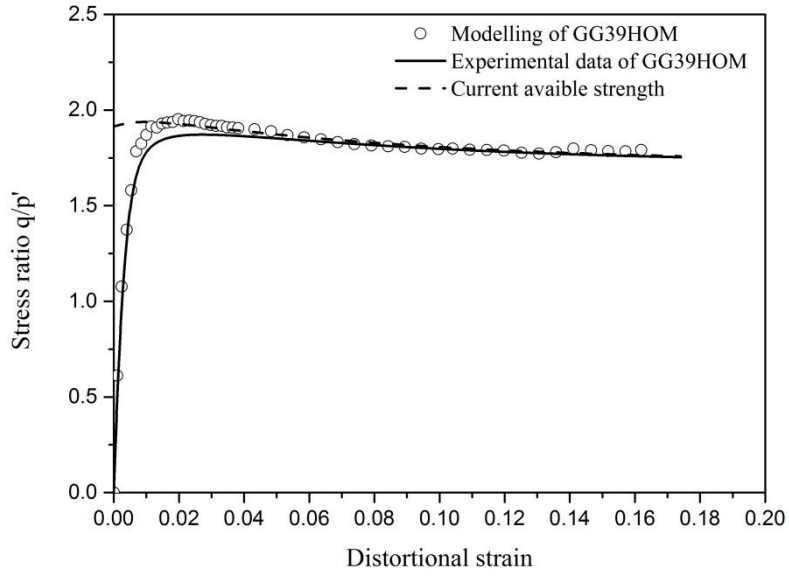

(a)

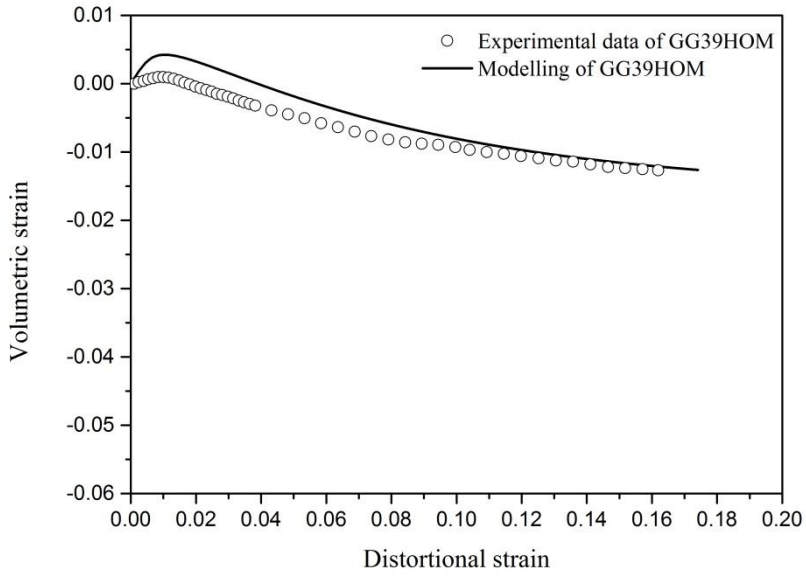

(b)

Figure 6-17 Triaxial compression test on a sample subjected to 8 litres of seepage to cause erosion at an effective confining pressure of 100 kPa. (a) stress-strain response (b) volumetric strain response.

6.3.4 Simulations of triaxial tests for soils subjected to 24 liters of seepage to cause erosion

Figures 6-18 to 6-20 present the result of drained triaxial tests on samples having undergone 24 liters of seepage and model simulations in $\eta_y \sim \varepsilon_q$ and $\varepsilon_p \sim \varepsilon_q$ planes. Tn the $\eta_y \sim \varepsilon_q$ plane, the solid line indicates variation in stress ratio, the dashed line indicates variation in current peak strength, the circles indicate experimental results. In the $\varepsilon_p \sim \varepsilon_q$ plane, the dashed line indicates model simulation and the circles indicate experimental results. The tests were conducted at effective stresses of 50, 100 and 200 kPa, respectively. The specific volume before shearing were 1.354 (50 kPa), 1.344 (100kPa), 1.339 (200 kPa), respectively. It is assumed that all samples have same fractal dimension the of the finer fraction $D_{sf} = 2.10$. The model simulations fit the experimental data well.

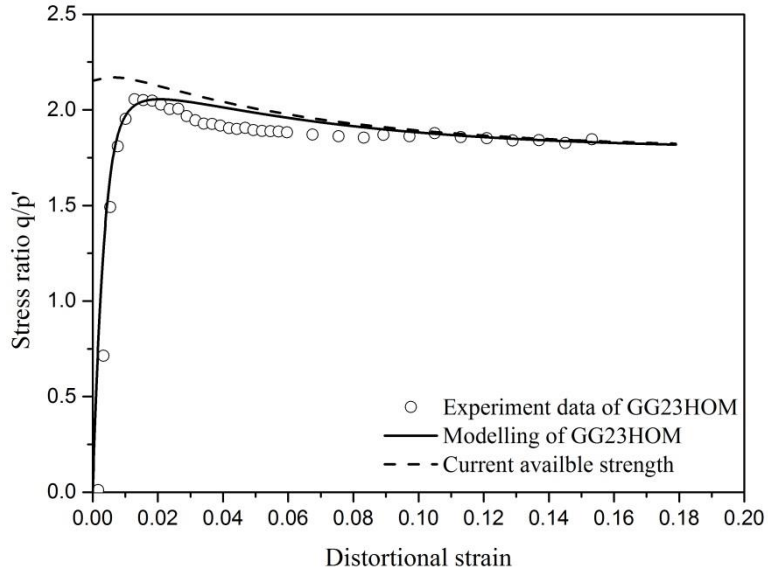

(a)

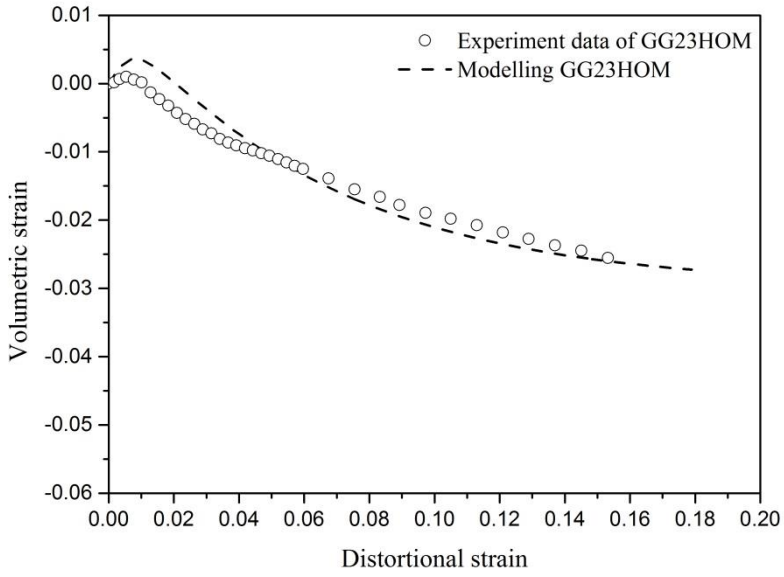

(b)

Figure 6-18 Triaxial compression test on a sample subjected to 24 liters of seepage to cause erosion at an effective confining pressure of 50 kPa. (a) stress-strain response (b) volumetric strain response.

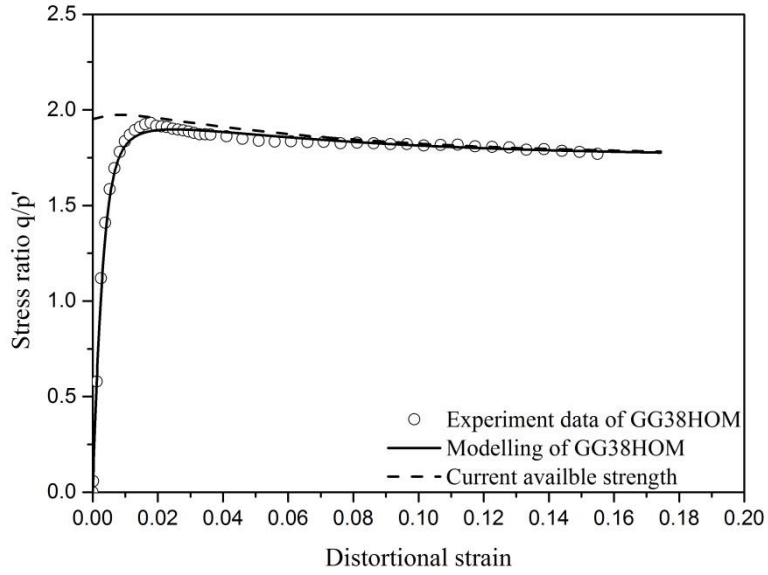

(a)

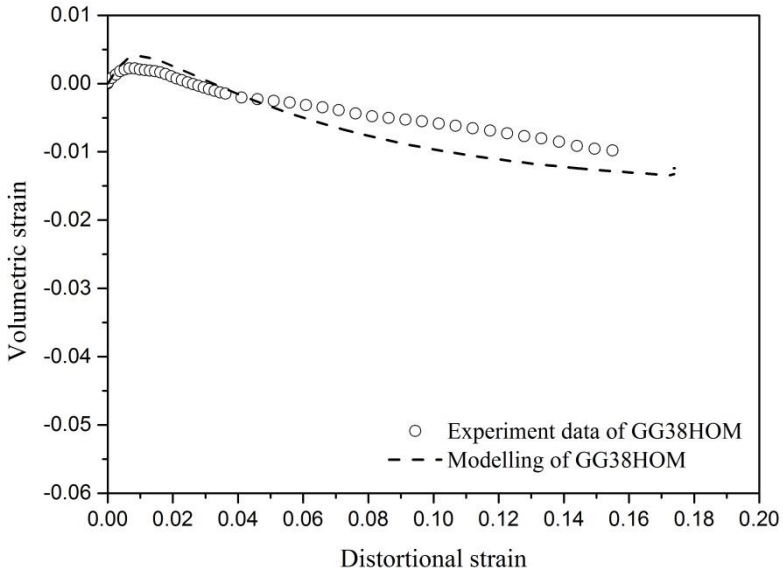

(b)

Figure 6-19 Triaxial compression test on a sample subjected to 24 liters of seepage to cause erosion at an effective confining pressure of 100 kPa. (a) stress-strain response (b) volumetric strain response.

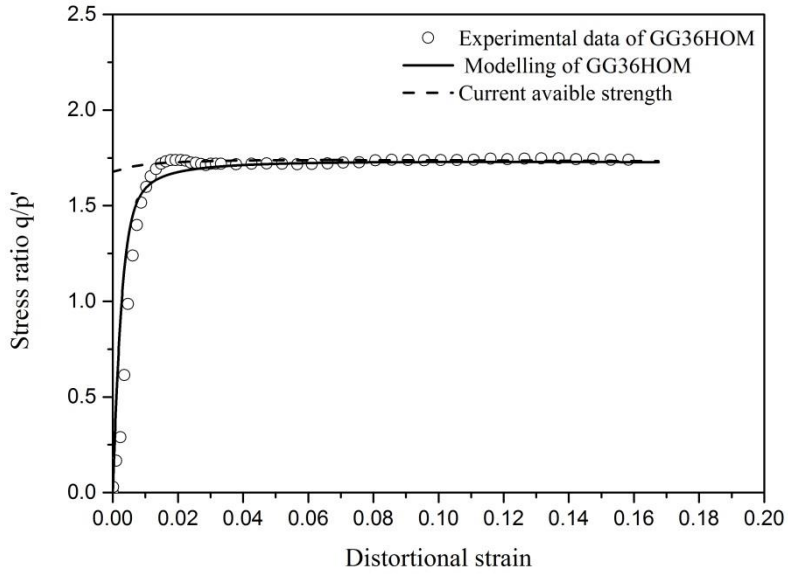

(a)

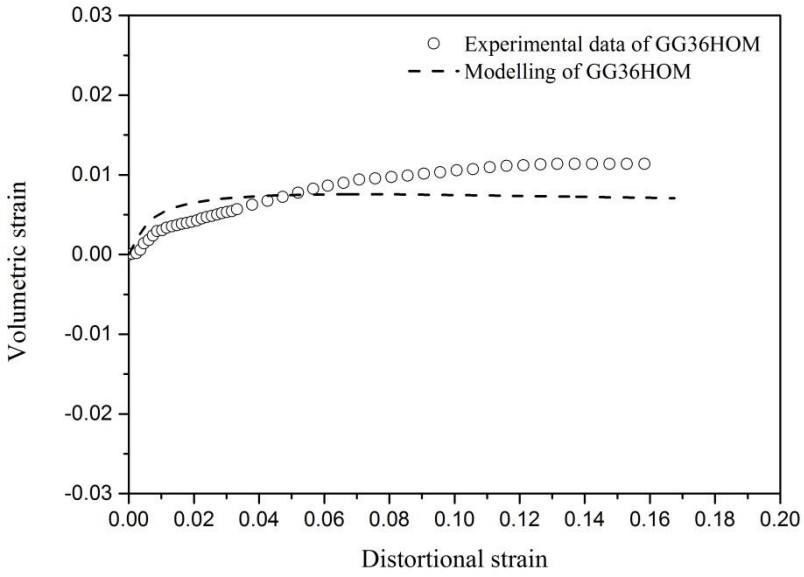

(b)

Figure 6-20 Triaxial compression test on a sample subjected to 24 liters of seepage to cause erosion at an effective confining pressure of 200 kPa. (a) stress-strain response (b) volumetric strain response.

6.3.5 Simulations of triaxial tests for soils subjected to 48 liters of seepage to cause erosion

Figures 6-18 to 6-20 present the results of drained triaxial tests on samples having undergone 48 litres of seepage and model simulations in $\eta_y \sim \varepsilon_q$ and $\varepsilon_p \sim \varepsilon_q$ planes. In the $\eta_y \sim \varepsilon_q$ plane, the solid line indicates variation in stress ratio, the dashed line indicates variation in current peak strength, the circles indicate experimental results. In the $\varepsilon_p \sim \varepsilon_q$ plane, the dashed line indicates model simulation and the circles indicate experimental results. The tests were conducted at effective stresses of 50 and 100 kPa, respectively. The specific volume before shearing were 1.421 (50 kPa), 1.389 (100kPa), 1.393 (200 kPa), respectively. It is assumed that all samples have same fractal dimension of the finer fraction $D_{sf} = 1.78$. The model simulations fit the experimental data well.

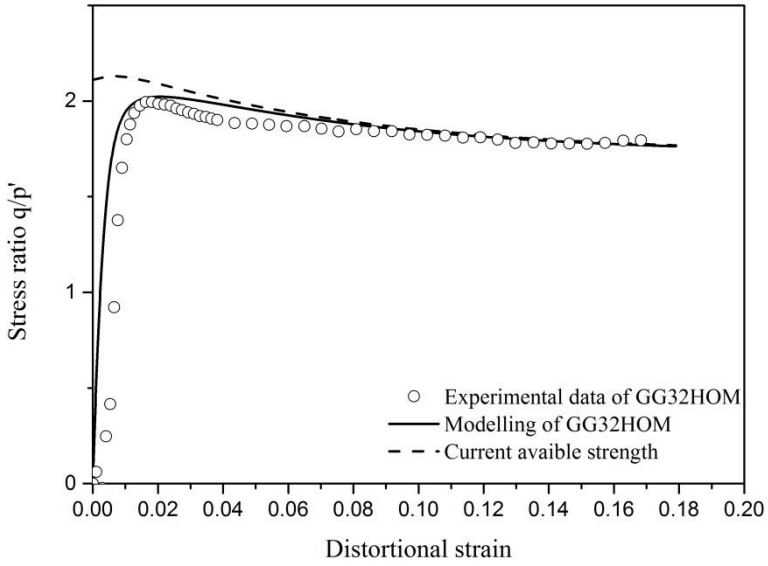

(a)

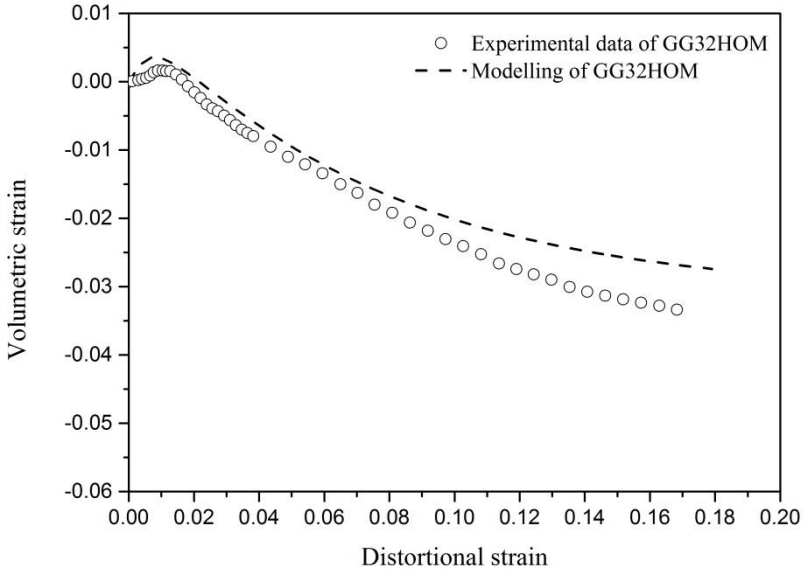

(b)

Figure 6-21 Triaxial compression test on a sample subjected to 48 liters of seepage to cause erosion at an effective confining pressure of 50 kPa. (a) stress-strain response (b) volumetric strain response.

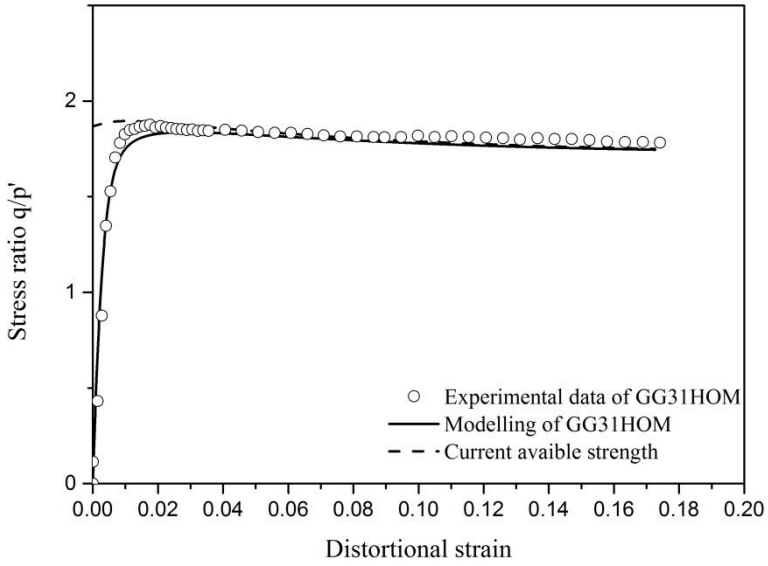

(a)

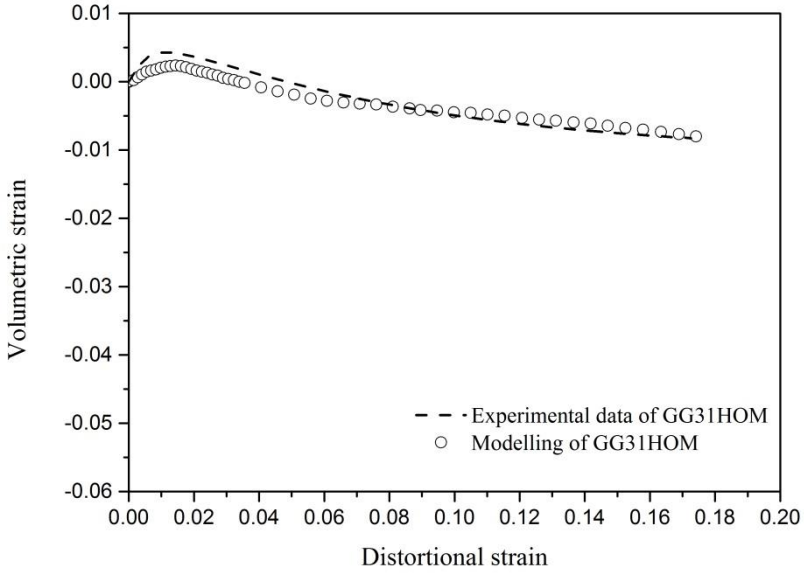

(b)

Figure 6-22 Triaxial compression test on a sample subjected to 48 liters of seepage to cause erosion at an effective confining pressure of 100 kPa. (a) stress-strain response (b) volumetric strain response.

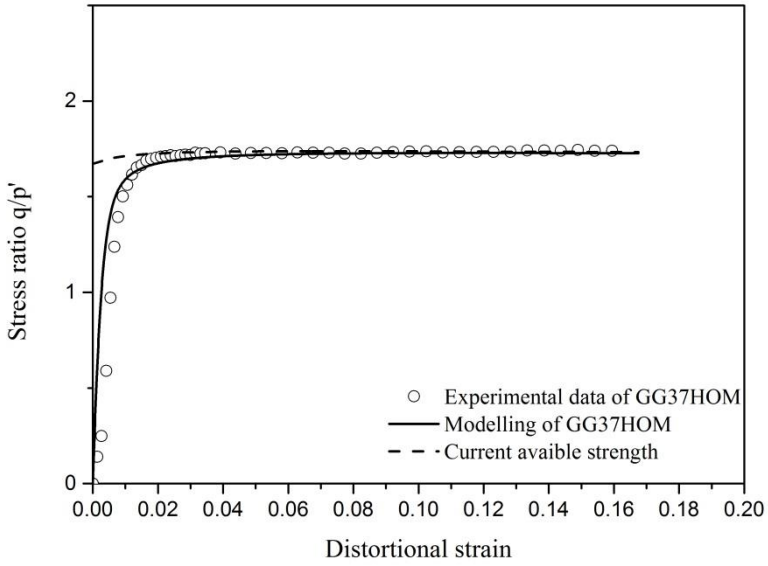

(a)

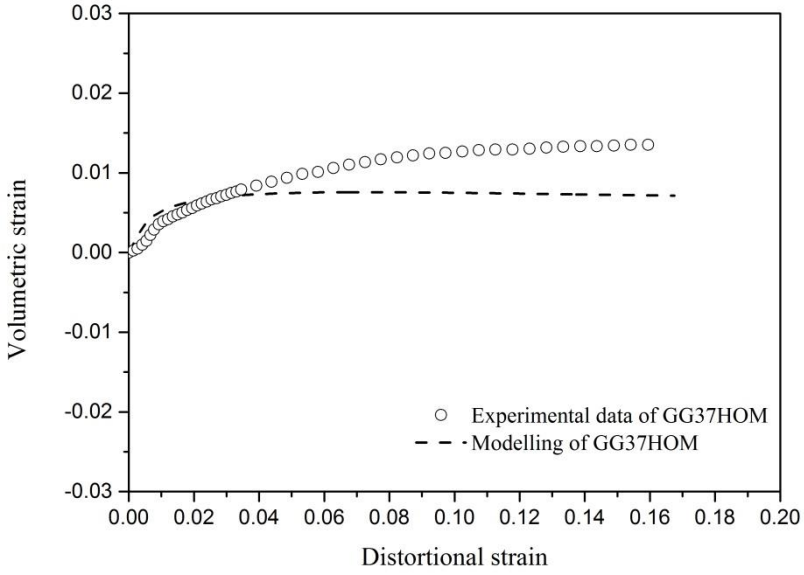

(b)

Figure 6-23 Triaxial compression test on a sample subjected to 48 liters of seepage to cause erosion at an effective confining pressure of 200 kPa. (a) stress-strain response (b) volumetric strain response.

6.4 DISCUSSION AND CONCLUSION

This chapter presents the modelling of stress-strain behaviors of soils having undergone different amount of internal erosion. An extension of the Severn-Trent sand model is presented.

The effects of internal erosion on the grading state index are described. A new method to estimate the grading state index, before and after internal erosion, is proposed using fractal theory. Thus the effects of internal erosion on the critical state can also be described using fractals.

The extended Severn-Trent sand model considering the effects of internal erosion, is calibrated and used to simulate a series of triaxial tests. In spite of the variations in volumetric strains at high confining pressures, which may because of the limitation of triaxial device and it is challenging to observe the real critical state, it turned out that the extended model reproduces the stress-strain behaviors well.

CHAPTER 7 SUMMARY AND CONCLUSIONS

7.1 GENERAL

The main objective of this research was to understand the mechanical consequences of internal erosion and develop a constitutive model able to simulate the stress-strain behavior of an eroded soil.

In doing so a new procedure to form homogeneous soil samples, post-erosion and prior to determinations of strength and stress-strain behaviors, was developed. Conducting triaxial tests on homogenous soil samples maximizes the relevance and usefulness of the results, and enables more reliable links to be made between microstructural characteristics and large scale mechanical behaviors.

Other accomplishments are listed below.

- The observations of differences in stress-strain behaviors of soil samples formed by the new procedure and a commonly used procedure that results in heterogeneous post-erosion particle size distributions.
- The production of a series of drained triaxial compression tests results from samples having undergone different amounts of internal erosion under varying effective confining stresses. A range of soil densities and hydraulic gradients were considered.
- Derivation of a direct mathematical link between the fractal dimension of the finer fraction and the void ratio of eroded soils, with single or double fractal particle size distribution(s), incorporating some practical and realistic assumptions.
- Definition of a new grading state index to incorporate all characteristics of the particle size distribution, including characteristics central to the potential erodibility of the soil.

- Extension of the Severn-Trent sand constitutive model to simulate the soil behavior, incorporating erosion-induced changes to void ratios, gradings and critical states. The model simulations provided a good fit to the experimental data.

7.2 A NEW SAMPLE FORMATION PROCEDURE THAT RESULTS IN HOMOGENEOUS POST-EROSION PARTICLE SIZE DISTRIBUTIONS

The new sample formation procedure involves the reallocation of fine particles in each compacted layer of a heterogeneous sample so that the subsequent erosion produces a homogeneous particle size distribution throughout the sample. It is a practical and reasonable technique for producing a sample for triaxial testing, enabling the observed stress-strain behavior to be linked to measures of initial state including the particle size distribution, void ratio and state parameter.

Drained triaxial compression tests on samples with homogeneous and heterogeneous post-erosion particle size distributions were compared. For two samples that had the same amount of fines lost due to internal erosion, the one with a homogeneous particle size distribution showed a greater peak strength. For samples with homogeneous post-erosion particle size distributions, but different amounts of fines lost by internal erosion, the peak strength decreased as the amount of fines lost increased.

7.3 ADDITIONAL TRIAXIAL TESTS

Additional laboratory triaxial erosion tests on a gap-graded soil having undergone different amounts of internal erosion at varying confining stresses were conducted. The erosion characteristics and stress-strain behaviors were observed.

The hydraulic gradient, confining stress and initial density have significant influences on the erosion characteristics, especially on the flow rate and cumulative eroded soil mass. The flow rate decreases with the increase of density or confining stress. It increases with the applied hydraulic gradient. The cumulative eroded soil mass increases with the increase of hydraulic gradient and decreases with the increase of initial density and confining stress.

The stress-strain behaviors of soils having undergone different amounts of internal erosion at varying effective stress states were also investigated. The peak deviator stress tends to decrease as the volume of seepage water and the amount of erosion increase. The volumetric strain at large shear strains decreases as the volume of seepage water and the amount of erosion increase. Internal erosion also causes the critical state line to move upwards. The upward movement of the critical state line is lesser than the increase of the void ratio due to internal erosion.

7.4 The fractal characteristics

A direct mathematical link between the fractal dimension and void ratio for soils, with single or double fractal particle size distributions, was developed incorporating some practical and realistic assumptions.

In gap-graded soils, different amounts of internal erosion results in the fractal dimension of the finer component of the particle size distribution to vary. The changing grading due to internal erosion may be expressed solely in terms of the changing fractal dimension. The change in void ratio can also be expressed in terms of this changing fractal dimension. The theoretical derivations fit the experimental data well.

7.5 MODELLING THE STRESS-STRAIN BEHAVIOR OF SOILS HAVING UNDERGONE DIFFERENT AMOUNTS OF INTERNAL EROSION

A new grading state index was defined, incorporating fractal theories, enabling the full shape of the particle size distribution to be considered. It is more accurate when compared to another grading state index that includes a rough linear approximation and is unable to account for a soil's gap-graded nature.

The movement of the critical state line was linked to the change in the grading state index.

The erosion-induced increase in void ratio, changing grading and shift of the critical state line were incorporated into an extended Severn-Trent sand model. The extended model was calibrated using the experimental data generated in this study. The simulations showed a good fit with the experimental data for a significant range of confining stresses and amounts of internal erosion.

7.6 Recommendations for further research

The following topics are worthy of further investigation.

- A microstructural analysis on the link between particle size and pore size distributions would be worthwhile. Undisturbed subsamples, taken from larger eroded samples, may be scanned using X-ray CT, or subjected to mercury intrusion testing, to permit detailed characterization of an eroded soil's pore microstructure and how it is affected by internal erosion.
- Triaxial erosion test on soils under complicated stress states. Study the mechanical consequence of internal erosion initiates under varying stress ratios.

- The effects of internal erosion on elastic properties may also be worthy of a more targeted study. A few investigations (Lin Ke 2014) have reported that the small-strain (elastic) stiffness of an eroded soil is higher than that of the same soil when it has not eroded. Other studies, including this study, have observed contrasting results.
- More attention may be devoted to the identification of the critical hydraulic gradient needed for internal erosion to commence. There may be an additional critical hydraulic gradient, beyond which the fines participating in the force structure start to be removed. In researching these issues consideration may be given to: (i) how fine particles in gap-graded soils occupy the void spaces between coarse particles, or (ii) form parts of the contacts between coarse particles, and (iii) actively participate in the force structure of the soil skeleton (Rahman and Lo 2007). The mechanisms underlying the mechanical consequences of internal erosion may alter depending on where the applied hydraulic gradient lies with respect to these two critical values.
- A study which addresses a more general soil behavior, including when a change to the grading occurs during shear, would also be welcome. In the study presented here, and most others in the literature, triaxial tests were conducted on samples after they had experienced a certain amount of erosion. However, shearing and erosion may occur at the same time in practice. The modelling ideas presented here, in which the state of a soil at any time can be expressed in terms of the current value of mean effective stress, deviator stress, void ratio and grading state index, need to be tested when erosion and shearing occur in different ways and concurrently.

REFERENCES

Arya, L.M., and Paris, J.F. 1981. A physicoempirical model to predict the soil moisture characteristic from particle-size distribution and bulk density data 1. Soil Science Society of America Journal **45**(6): 1023-1030.

Been, K., and Jefferies, M.G. 1985. A state parameter for sands. Géotechnique **35**(2): 99-112.

Bendahmane, F., Marot, D., and Alexis, A. 2008. Experimental parametric study of suffusion and backward erosion. Journal of Geotechnical and Geoenvironmental Engineering **134**(1): 57-67.

Bradshaw, A., and Baxter, C. 2007. Sample preparation of silts for liquefaction testing. Geotechnical Testing Journal **30**(4): 324-332.

Burenkova, V. 1993. Assessment of suffusion in non-cohesive and graded soils. Filters in geotechnical and hydraulic engineering. Balkema, Rotterdam: 357-360.

Chang, D., and Zhang, L. 2011. A stress-controlled erosion apparatus for studying internal erosion in soils. Geotechnical Testing Journal **34**(6): 579-589.

Chang, D., and Zhang, L. 2012. Critical hydraulic gradients of internal erosion under complex stress states. Journal of Geotechnical and Geoenvironmental Engineering **139**(9): 1454-1467.

Chang, D., Zhang, L., and Cheuk, J. 2014. Mechanical consequences of internal soil erosion. HKIE Transactions **21**(4): 198-208.

Daouadji, A., Hicher, P.-Y., and Rahma, A. 2001. An elastoplastic model for granular materials taking into account grain breakage. European Journal of Mechanics-A/Solids **20**(1): 113-137.

Dodds, P.S., and Weitz, J.S. 2002. Packing-limited growth. Physical Review E **65**(5): 056108.

Fannin, R., and Slangen, P. 2014. On the distinct phenomena of suffusion and suffosion. Géotechnique Letters **4**(4): 289-294.

Fell, R., Wan, C.F., Cyganiewicz, J., and Foster, M. 2003. Time for development of internal erosion and piping in embankment dams. Journal of geotechnical and geoenvironmental engineering **129**(4): 307-314.

Foster, M., Fell, R., and Spannagle, M. 2000. The statistics of embankment dam failures and accidents. Canadian Geotechnical Journal **37**(5): 1000-1024.

Foster, M.A., and Fell, R. 1999. Assessing embankment dam filters which do not satisfy design criteria. University of New South Wales, School of Civil Engineering.

Gajo, A., and Muir Wood, M. 1999. Severn–Trent sand: a kinematic-hardening constitutive model: the q–p formulation. Géotechnique **49**(5): 595-614.

Gee, G.W., and Bauder, J.W. 1986. Particle-size analysis 1. Methods of soil analysis: Part 1—Physical and mineralogical methods(methodsofsoilan1): 383-411.

Hicher, P. Y. 2013. Modelling the impact of particle removal on granular material behaviour. Géotechnique **63**(2): 118-128

Holtz, W.G., and Gibbs, H. 1956. Triaxial shear tests on pervious gravelly soils. Journal of the Soil Mechanics and Foundations Division **82**(1): 1-22.

Hunt, A.G., and Gee, G.W. 2002. Application of critical path analysis to fractal porous media: Comparison with examples from the Hanford site. Advances in Water Resources **25**(2): 129-146.

Indraratna, B., Muttuvel, T., Khabbaz, H., and Armstrong, R. 2008. Predicting the erosion rate of chemically treated soil using a process simulation apparatus for internal crack erosion. Journal of Geotechnical and Geoenvironmental Engineering **134**(6): 837-844.

Istomina, V. 1957. Filtration stability of soils. Gostroizdat, Moscow, Leningrad **15**.

Ke, L., and Takahashi, A. 2012. Strength reduction of cohesionless soil due to internal erosion induced by one-dimensional upward seepage flow. Soils and Foundations **52**(4): 698-711.

Ke, L., and Takahashi, A. 2014a. Experimental investigations on suffusion characteristics and its mechanical consequences on saturated cohesionless soil. Soils and Foundations **54**(4): 713-730.

Ke, L., and Takahashi, A. 2014b. Triaxial erosion test for evaluation of mechanical consequences of internal erosion. Geotechnical Testing Journal **37**(2): 347-364.

Ke, L., and Takahashi, A. 2015. Drained monotonic responses of suffusional cohesionless soils. Journal of Geotechnical and Geoenvironmental Engineering **141**(8): 04015033.

Kenney, T., and Lau, D. 1985. Internal stability of granular filters. Canadian geotechnical journal **22**(2): 215-225.

Kenney, T., and Lau, D. 1986. Internal stability of granular filters: Reply. Canadian Geotechnical Journal **23**(3): 420-423.

Kézdi, A. 1979. SOIL PHYSICS-SELECTED TOPICS-DEVELOPMENTS IN GEOTECHNICAL ENGINEERING-25.

Kikumoto, M., Wood, D.M., and Russell, A. 2010. Particle crushing and deformation behaviour. Soils and foundations **50**(4): 547-563.

Kovács, G. 2011. Seepage hydraulics. Elsevier.

Ladd, R. 1978. Preparing test specimens using undercompaction.

Lafleur, J., Mlynarek, J., and Rollin, A.L. 1989. Filtration of broadly graded cohesionless soils. Journal of Geotechnical Engineering **115**(12): 1747-1768.

Lin Ke, A.T. 2014. Traxial erosion test for evaluation of mechanical consequences of internal erosion. Geotechnical testing journal.

Lubochkov, E. 1965. Graphical and analytical methods for the determination of internal stability of filters consisting of non cohesive soil. Izvestia, vniig **78**: 255-280.

Luzzani, L., and Coop MR . 2002. On the relationship between particle breakage and the critical state of sands. Soils and foundations **42**(2): 71-82.

Mandelbrot, B.B. 1983. The fractal geometry of nature. WH freeman New York.

McDougall, J., Kelly, D., and Barreto, D. 2013. Particle loss and volume change on dissolution: experimental results and analysis of particle size and amount effects. Acta Geotechnica **8**(6): 619-627.

Moffat, R. 2005. Experiments on the internal stability of widely graded cohesionless soils. University of British Columbia.

Moffat, R., Fannin, R.J., and Garner, S.J. 2011. Spatial and temporal progression of internal erosion in cohesionless soil. Canadian Geotechnical Journal **48**(3): 399-412.

Muir Wood, D. 1990. Soil behaviour and critical state soil mechanics. Cambridge university press.

Muir, D. 2004. Geotechnical modelling. CRC press.

Muir Wood, D., and Belkheir, K. 1994. Strain softening and state parameter for sand modelling. Geotechnique **44**(2): 335-339.

Muir Wood, D., and Maeda, K. 2008. Changing grading of soil: effect on critical states. Acta Geotechnica **3**(1): 3.

Muir Wood, D. 2007. The magic of sands. Canadian Geotechnical Journal **44**(11): 1329-1350. doi: 10.1139/t07-060.

Muir Wood, D., and Maeda, K. 2007. Changing grading of soil: effect on critical states. Acta Geotechnica **3**(1): 3-14. doi: 10.1007/s11440-007-0041-0.

Muir Wood, D., Maeda, K., and Nukudani, E. 2010. Modelling mechanical consequences of erosion. Géotechnique **60**(6): 447-457.

Ouyang, M., and Takahashi, A. 2015. Influence of initial fines content on fabric of soils subjected to internal erosion. Canadian Geotechnical Journal **53**(2): 299-313.

Perfect, E. 1997. Fractal models for the fragmentation of rocks and soils: a review. Engineering geology **48**(3-4): 185-198.

Perfect, E., and Kay, B. 1995. Applications of fractals in soil and tillage research: a review. Soil and Tillage Research **36**(1-2): 1-20.
Rahman, M.M., and Lo, S. 2007. Equivalent granular void ratio and state parameters for loose clean sand with small amount of fines.

Richards, K.S., and Reddy, K.R. 2009. True triaxial piping test apparatus for evaluation of piping potential in earth structures. Geotechnical Testing Journal **33**(1): 83-95.

Roscoe, K. 1963. Mechanical behaviour of an idealized'wet'clay. *In* Proc. 3rd Eur. Conf. Soil Mech. Wiesbaden, 1963. pp. 47-54.

Russell, A. 2014. How water retention in fractal soils depends on particle and pore sizes, shapes, volumes and surface areas. Géotechnique **64**(5): 379.

Russell, A.R. 2010. Water retention characteristics of soils with double porosity. European journal of soil science **61**(3): 412-424.

Russell, A.R. 2011. A compression line for soils with evolving particle and pore size distributions due to particle crushing. Géotechnique Letters **1**(1): 5-9.

Russell, A.R., and Buzzi, O. 2012. A fractal basis for soil-water characteristics curves with hydraulic hysteresis. Geotechnique **62**(3): 269.

Sato, M., and Kuwano, R. 2015. Suffusion and clogging by one-dimensional seepage tests on cohesive soil. Soils and Foundations **55**(6): 1427-1440.

Sato, M., and Kuwano, R. 2018. Laboratory testing for evaluation of the influence of a small degree of internal erosion on deformation and stiffness. Soils and foundations **58**(3): 547-562.

Scholtès, L., Hicher, P.-Y., and Sibille, L. 2010. Multiscale approaches to describe mechanical responses induced by particle removal in granular materials. Comptes Rendus Mécanique **338**(10-11): 627-638.

Sherman, W. 1953. Filter Experiments and Design Criteria. ARMY ENGINEER WATERWAYS EXPERIMENT STATION VICKSBURG MISS.

Shire, T., O'Sullivan, C., Hanley, K., and Fannin, R.J. 2014. Fabric and effective stress distribution in internally unstable soils. Journal of Geotechnical and Geoenvironmental Engineering **140**(12): 04014072.

Sibille, L., Marot, D., and Sail, Y. 2015. A description of internal erosion by suffusion and induced settlements on cohesionless granular matter. Acta Geotechnica **10**(6): 735-748.

Skempton, A., and Brogan, J. 1994. Experiments on piping in sandy gravels. Geotechnique **44**(3): 449-460.

Taylor, D.W. 1948. Fundamentals of soil mechanics. LWW.

Terzaghi, K., Peck, R.B., and Mesri, G. 1948. Soil mechanics in engineering practice. John Wiley & Sons.

Tyler, S.W., and Wheatcraft, S.W. 1989. Application of fractal mathematics to soil water retention estimation. Soil Science Society of America Journal **53**(4): 987-996.

Tyler, S.W., and Wheatcraft, S.W. 1992. Fractal scaling of soil particle-size distributions: analysis and limitations. Soil Science Society of America Journal **56**(2): 362-369.

Vo, T., and Russell, A.R. 2013. Unsaturated soil interacting with a rotating model wall. International Journal of Physical Modelling in Geotechnics **13**(2): 63-78.

Vo, T., Yang, H., and Russell, A.R. 2016. Cohesion and suction induced hang-up in ore passes. International Journal of Rock Mechanics and Mining Sciences **87**: 113-128.

Wan, C.F. 2006. Experimental investigation of piping erosion and suffusion of soils in embankment dams and their foundations. University of New South Wales.

Wan, C.F. 2009. Experimental investigations of piping erosion and suffusion of soils in embankment dams and their foundations. University of New South Wales.

Wan, C.F., and Fell, R. 2004. Investigation of rate of erosion of soils in embankment dams. Journal of geotechnical and geoenvironmental engineering **130**(4): 373-380.

Wan, C.F., and Fell, R. 2008. Assessing the potential of internal instability and suffusion in embankment dams and their foundations. Journal of geotechnical and geoenvironmental engineering **134**(3): 401-407.

Wang, K., Zhang, R., and Wang, F. 2005. Testing the pore-solid fractal model for the soil water retention function. Soil Science Society of America Journal **69**(3): 776-782.

Wang, G., Horikoshi, K., and Takahashi, A. 2019. Effects of Internal Erosion on Parameters of Subloading Cam-Clay Model. Geotechnical and Geological Engineering: 1-13.

Xiao, M., and Shwiyhat, N. 2012. Experimental investigation of the effects of suffusion on physical and geomechanic characteristics of sandy soils. Geotechnical Testing Journal **35**(6): 890-900.

Yang, J., Yin, Z.Y., Laouafa, F., and Hicher, P.Y. 2019. Internal erosion in dike - on - foundation modeled by a coupled hydromechanical approach. International Journal for Numerical and Analytical Methods in Geomechanics **43**(3): 663-683.

Yu, B., Cai, J., and Zou, M. 2009. On the physical properties of apparent two-phase fractal porous media. Vadose Zone Journal **8**(1): 177-186.